THE ELECTROENCEPHALOGRAM, METABOLIC RHYTHMS, AND THYROID HORMONE MECHANISMS IN THE ADULT BRAIN

by

STEVEN MOFFETT

A dissertation submitted to the

Graduate School-Camden

Rutgers, The State University of New Jersey

In partial fulfillment of the requirements

For the degree of

Doctor of Philosophy

Graduate Program in Computational and Integrative Biology

Written under the direction of

Dr. Joseph Martin, PhD

And approved by

_____

Dr. Joseph Martin, PhD

_____

Dr. Grace Brannigan, PhD

_____

Dr. Venkat Venkataraman, PhD

_____

Dr. Eric Klein, PhD

Camden, New Jersey

October 2018

ABSTRACT OF THE DISSERTATION

The Electroencephalogram, Metabolic Rhythms, and Thyroid Hormones in the Adult Brain

by STEVEN MOFFETT

Dissertation Director:

Dr. Joseph Martin, PhD

Within brain, rhythmic and spontaneous molecular cascades determine behavior. We used multiple methods of analysis to quantify several of these molecular cascades. The protein S100B acts as a bimodal calcium transduction switch in retinal cells involved with circadian rhythm entrainment. We show that S100B knockout mice exhibit a secondary circadian rhythm during intervals of photic entrainment. In another investigation, we searched for behavioral rhythms shorter than a day through analysis of the electroencephalogram (EEG). Using two separate methods, we show evidence for a short ultradian rhythm (SUR) in rats and mice correlative with sharp decreases in delta EEG activity and non-rapid-eye movement (non-REM) sleep. We also show the first semi-automated detection of a behavioral SUR using EEG data, which may provide insight into metabolic oscillations within brain tissue separate from the transcription/translation feedback loops governing circadian rhythms. In brain, extracellular adenosine accumulates during periods of wakefulness and diminishes after periods of non-REM sleep. We measured EEG and locomotor activity in mice lacking

CD73, an enzyme involved with conversion of adenosine triphosphate (ATP) into adenosine. We show that CD73 knockout mice exhibit different amounts of wakefulness and REM sleep compared to wild-type mice, results consistent with a role of adenosine in sleep. Thyroid hormones also affect sleep. A dysthyroid state can induce sleep disturbance, lethargy, anxiety, or other symptoms. We injected 3-iodothyronamine (T1AM), a decarboxylated thyroid hormone derivative, into the preoptic region of adult male rats and collected EEG to quantify post-injection sleep. T1AM causes sleep fragmentation and, contrary to our hypothesis, decreased sleep in a similar way to thyroid hormone, which may be due to shared mechanisms of sleep regulation. We also demonstrate the existence of two new high-frequency EEG bands which vary in relation to sleep behavior in rats. Finally, we demonstrate that nicotinic acetylcholine receptors (nAChRs), which contribute to electrical activity regulation in brain, are inhibited by triiodothyronine (T3), a thyroid hormone, and pregnenolone sulfate, a neurosteroid with similar molecular properties. These data give new insight into the structure-activity relationship of neurosteroids relative to nAChRs and to other related receptors in the brain.

Acknowledgments

I would foremost like to thank Dr. Joseph Martin, who has been my teacher, mentor, and friend for a decade. I cannot express enough gratitude for his patience, his teaching style, his advice, and his dedication to my continual learning. I also thank Dr. Grace Brannigan, whose practical and contextual emphasis while I was learning new topics made even intimidating and abstract biological concepts somehow personal. Many thanks also to Dr. Venkat Venkataraman, whose sound advice as well as his enthusiasm to collaborate and share knowledge over the years reminds me of the best things about the academic community. And thank you to Dr. Eric Klein, whose piercing insight and deep technical knowledge helped me become proficient at my most difficult lab protocols, and who extended a helping hand at a critical moment in my studies.

I would also like to acknowledge that the people above are masters within their disciplines as well as outside of their disciplines; a committee like this is a dream for a computational and integrative student.

I would also like to acknowledge my friends for their assistance and moral support throughout my education, chief among them Daniel Russo, Harish Swaminathan, and Nastassia Pouradier Duteil, whose support over the years has been indispensable, Kyle Jenkins, whom I have had the honor of being lab partners with as well as the honor of his truly dear friendship, Katarina and Joseph Kawash, whose generosity with their time, advice, and humor I have treasured, Sal, Lekha, Darya, Sean, Giulia, Zheming, Nathaniel, Maria Laura, Aylin, Tom, Nicolle, Thomas, Anaïs, Remi, Olivier, Joseph Andre, Rob,

Spyros, Kuhn, Jane, David, Matt, Kelly, Janet, Catherine, Nicole, Laura, and Lancelot, with whom I always enjoy spending time and who have helped me immensely over the years, Dr. Jongmin Nam, Dr. Nir Yakoby, Dr. Sean O'Malley, Dr. Benedetto Piccoli, Dr. Dawei Hong, Dr. Kwangwon Lee, and Dr. Wiliam Saidel, who gave guidance as teachers but who approached as friends.

I would also like to acknowledge the support of my family, without whom none of this would be possible. Thanks to my brother and sister-in-law, who lent a sympathetic ear (and provided a meal) no matter what the circumstances, from the truly grave to the truly frivolous. Thanks to my niece, my nephew, and my sisters, who love and support me through everything. Thanks to my father, who has commiserated with me about everything under the sun. Thanks to my mother, whose fortitude and grace under pressure I will never fully understand. When things were most difficult, I thought of my family to bring me courage.

Dedication

To my niece, my nephew, my younger sister, my brother, my sister-in-law, my older sister, my father, and my mother.

Table of Contents

List of Figures and Tables

Chapter 1

Chapter 2

Chapter 3

Chapter 4

Chapter 5

Chapter 6

Appendix Figures

Supplemental Figures

Introduction

Beneath behavior lies multitudes. This was our philosophy when conducting our investigations. Although our experiments all involve brain tissue activity and its consequent behaviors, our investigative methods were wide-ranging. To properly express this multi-pronged approach, each of the following 6 chapters are presented as a self-contained journal article. In some cases, these chapters exist as published articles (4 and 5). Other chapters are being prepared for manuscript submission. In general, the progression of the following research goes from macroscopic to microscopic, starting with behavioral studies and ending with neural receptor function. These studies represent several breakthroughs in understanding of brain activity and illustrate the extremely complex relationship between intracellular transduction switches, electrochemical activity, extracellular enzymes, metabolic derivatives, summed electroencephalographic activity, and individual receptor function.

Chapter 1: S100B Affects Circadian Rhythm in Adult Male Mouse

1.1 Abstract

S100B has been demonstrated to localize in mammalian retina, as well as in several neural pathways and nuclei involved with circadian rhythm and entrainment. Its absence shows effects on phototransduction. The S100B protein is a calcium-sensitive protein using two EF-hand motifs. It binds with rod outer segment guanylate cyclase (ROS-GC1) and serves as part of a bimodal calcium transduction switch, along with neurocalcin δ (NCALD). Unlike NCALD, S100B's adaptive function in this bimodal switch is not definitively known, as it becomes active only at pathologically high intracellular calcium concentrations, and further raises this concentration after activation. We subjected wild-type and S100B KO mice to long-term studies of circadian locomotor activity, in both photic entrainment conditions and free-running conditions. We show that S100B KO mice exhibit a secondary circadian rhythm during intervals of entrainment, a shorter free-running period, and an eventual disorganization of circadian activity, even in photic entrainment lighting conditions. S100B may be involved in the homeostatic process maintaining normal photic entrainment and free-running period.

1.2 Introduction

Circadian rhythms are a set of molecular and genetic oscillations whose cyclical, behavioral consequences have a period of approximately 24 hours, can be re-set by environmental cues, and can persist even in the absence of such cues. Plants [1], cyanobacteria [2], fungi [3], and animals [4] exhibit circadian rhythms, and the term

chronobiology describes the studies of these oscillations and behaviors [5]. Chronobiological studies usually involve perturbation of the underlying autoregulatory feedback loops of a given organism by changing environmental, anatomical, cellular, or genetic (genomic, transcription, or translation) conditions, followed by observation of the resulting periodic behaviors.

Daily, periodic behavior in the absence of external cues, known as the free-running state, can be manipulated by timed stimuli; these stimuli change the periodicity of, or re-entrain, the circadian rhythm [6]. Re-entrainment allows circadian rhythm-exhibiting organisms to stay synchronous with the external world. The minimum effective controlling stimuli often bears little resemblance to the selective conditions guiding the establishment of the circadian rhythm: relatively short light pulses early in an organism's subjective "night" can prolong the circadian rhythm [7, 8]. Conversely, some manipulations--to the neural tissue or to genetic material--can abolish the ability of organisms to be re-entrained [9, 10]. These effects can be partial or complete [10].

Other stimuli, such as timed feeding [11], social interaction [12], sounds [13], and physical activity [14, 15], can influence entrain circadian rhythms. Nevertheless, the predictability of the sun's diurnal appearance from most vantage points on earth make light one of the most widespread and dominant cues of circadian rhythm entrainment.

Photic entrainment in mammals is governed by photoreceptive elements localized in the retina, which project to nuclei in the cerebrum and neuroendocrine glands. This includes the most important and well-studied nucleus contributing to both re-entrainment and

to the free-running aspect of circadian rhythm, the suprachiasmatic nucleus (SCN) [16, 17].

Photoreceptive elements rod and cone cells form the visual field. Experiments in which mice with a visual retinal degeneration mutation, rendering their visual photoreceptive elements non-functioning and making them functionally blind, still exhibit photic entrainment by light pulses no different from the photic entrainment of wild-type mice [18]. Entrainment in mammals is only abolished after bilateral enucleation (eye removal), in which all projecting tracts from the retinas are severed [19]. Therefore, the nonvisual aspect of photoreceptive cells is necessary for photoentrainment.

Unlike visual component cells, non-visual photoreceptive elements, or melanopsin-containing intrinsically photosensitive retinal ganglion cells (ipRGCs), do not contribute to the visual field, and do not reach their projection sites with ordered topographic mapping. These cells comprise the photic entrainment pathway, which involves the retina, retinohypothalamic tract (RHT), SCN, intergeniculate leaflet (IGL), ventrolateral geniculate nucleus (vLGN), and pretectum (including the olivary pretectal nucleus) [20]. During photic entrainment, ipRGCs project luminance information to the SCN with its intrinsic photopigment, melanopsin. This photopigment is less sensitive to light than rod and cone photopigments (rhodopsin in rods and photopsins I, II, and III in cones). Light levels below the detection limit of melanopsin, however, can also achieve photic entrainment, because rod and cone cells can rely on ipRGCs to relay light information to the SCN [21]. Genetic ablation of all ipRGCs in mice cripples photoentrainment, even as

visual sense is spared [22]. This implies that ipRGCs are necessary for photic entrainment.

The retina is a multi-layered tissue. The outer segment, where rod and cone cells are organized, make connections to horizontal cells (connecting, generally, rods to cones), and bipolar cells, which relay signal to the retinal ganglion cells [23]. Visual component cells are unlike the other cell types in their transduction of meaningful data: the cells are continuously depolarized in the absence of light. The pigment in photosensitive visual component cells changes conformation and causes, through release of cyclic GMP phosphodiesterase, a cascade that stops release of its neurotransmitter, glutamate, to bipolar cells. Bipolar cells come in two functional varieties: on-center bipolar cells are hyperpolarized by glutamate, so when a light is on, the drop in synaptic glutamate causes them to depolarize, while off-center bipolar cells act in the opposite way.

In phototransduction, a critical signaling molecule is cyclic GMP, whose hydrolysis by light-stimulated phosphodiesterase leads to visual cell hyperpolarization. Cyclic GMP partially acts to restore the depolarized state, due to calcium-sensing proteins: guanylate cyclase activating proteins (GCAPs), unbound from the depleted calcium of the hyperpolarized state, stimulate retina outer-segment guanylate cyclase (ROS-GC) to synthesize cyclic GMP more rapidly; the rising cyclic GMP opens cyclic nucleotide-gated (CNG) channels and helps restore calcium to its darkness concentration (reviewed in [24]; [25]).

Calcium is a second messenger in several cell types within the entrainment pathway, and classes of neuronal calcium sensor (NCS) proteins mediate effects of calcium. Calcium binds to these proteins using an EF hand motif, at a loop joining the motif's double alpha helix. The cytosolic NCS neurocalcin δ (NCALD) has three EF hands capable of binding calcium [26]. When bound to calcium ions, a conformational change extrudes the N-terminus of NCS proteins, allowing NCALD myristoylation, which enables it to bind to membrane [26, 27]. This can bring NCALD into proximity of membrane-bound guanylate cyclases including ROS-G1, or can facilitate binding to the perinuclear compartment [28, 29]. NCALD stimulates ROS-GC1 as a function of intracellular calcium concentration and is present in amacrine and ganglion cells, as well as in the inner plexiform layer along with ROS-GC1 [28].

NCALD binds with the protein S100B, a dimer which also binds calcium via EF hand motifs [30]. Enhanced binding of the two proteins is calcium-dependent [30]. S100B proteins occur in outer plexiform, inner nuclear, and ganglion cell layers of the retina, and localize in photoreceptor-bipolar cell synapses and cone photoreceptors (but not in rod photoreceptors) [31]. Like NCALD, S100B proteins stimulate ROS-GC1, but do so on a different protein module [29]. S100B proteins also differ from NCALD in their activity in the presence of calcium: at low concentrations of calcium, S100B does not stimulate the ROS-GC1, but at high calcium levels, S100B stimulates ROS-GC1, leading to enhanced cyclic GMP synthesis, CNG stimulation, and further increases in calcium influx [31].

In vivo, the influence of S100B on phototransduction is subtle but statistically reliable. Compared to wild-type mice, the electroretinogram of S100B knockout mice shows a widened b-wave and a diminished ratio of the b-wave to a-wave amplitude, as well as a delay in peak arrival of both waves. These results imply multiple S100B influence sites outside of the outer cone segment of the retina [31]. S100B's expression in cells that conduct rod signaling to other rods and to cone cells also indicates a possible modulation of rod signaling, even if the protein is not specifically expressed in rod cells.

S100B is present in glial cells throughout the brain, with elevated expression in the SCN [32], and it interacts with at least one other neuronal calcium sensor involved in circadian rhythms, NCALD [30]. Further, S100B's presence in, and modification of, cells directly involved with the photic entrainment pathway and the free-running pathway make perturbation of its expression a candidate for alteration of both processes.

We compared the entrainment to light, free-running circadian rhythm, and photic re-entrainment of wild-type mice compared to S100B knockouts. We found indications of a free-running circadian rhythm superimposed on the 12:12 light:dark photoentrainment rhythm in S100B KO mice. We also show a significantly shorter free-running circadian rhythm in S100B mice compared to wild type mice during the dark:dark interval of data collection. We show a gradual disorganization of the circadian rhythm of S100B knockouts toward the end of the data collection interval, compared to no such disorganization in wild-type mice. These results suggest several possible overlapping effects of the S100B protein.

1.3 Materials and Methods

Experimental animals

Four male wild type, and four male S100B knockout BALB-C mice, weighing ~20 g, were generously donated by our collaborator, Dr. Venkat Venkataraman (Rowan School of Osteopathic Medicine).

Experimental chamber

Mice were housed individually in shoebox cages within an electrically shielded and sound dampened Faraday chamber. The temperature was maintained at 22.2–23.3 °C and relative humidity was controlled at 55%. During light:dark entrainment intervals of data collection, lights in the experimental chamber were on from 7:00 AM until 7:00 PM and off from 7:00 PM until 7:00 AM. During the dark:dark free-running interval of data collection, mice were housed in individual sound and light-shielded chambers, with noisemaking flow-through fans providing fresh air to each mouse. Intake and outflow of oxygen was shielded from any possible encounter with incident light with porous foam, and all lights in the Faraday chamber were kept off. Mice were fed *ad libitum*, and food stock replenishments were administered two sporadic times per week, in dim red lighting.

Transmitter implantation surgery

For each surgery, a mouse was place in an induction chamber primed with 5% gaseous isoflurane at a flow rate of 2 LPM for 5 min, then placed on a platform maintained at 37

°C to prevent hypothermia. The gaseous mixture was reduced to 2.5% isoflurane, with flow rate maintained at 2 LPM. An E-Mitter Transponder (Mini Mitter, Bend, OR) was implanted through a small midventral incision in the abdominal wall. The muscle layer and the skin were closed with vicryl sutures and bacitracin was applied topically. The mouse was injected intramuscularly with 0.10 mL 0.125% bupivacaine. All procedures were approved by the Institutional Animal Care and Use Committee (IACUC) at Rutgers University.

Data collection and analysis

All data was collected via the E-Mitter transponder. Activity counts (arbitrary units), generated via changes in signal strength between the transponder and the nearby receiver box, were summed over each minute. Minute-to-minute values were imported into the ImageJ (NIH, Bethesda, MD) plugin ActogramJ (University of Wuerzburg, Germany). Periodogram analyses were performed in ActogramJ using a Chi-square test ($p < 0.05$). Periodogram values for determination of the free-running state were imported into Graphpad Prism 5.0 (La Jolla, CA).

Experimental design

Experiment 1: Two wild-type and two S100B KO mice were entrained on a 12:12 light:dark cycle for 33 days, followed by 60 days of constant dark (12:12 dark:dark).

Experiment 2: Two wild-type and two S100B KO mice were entrained on a 12:12 light:dark cycle for 18 days, followed by 37 days of constant dark (12:12 dark:dark), followed by re-entrainment of a 12:12 light:dark cycle for 80 additional days.

1.4 Results

Experiment 1:

The circadian period of WT-1A observed during entrainment was 1440 minutes, while the free-running interval (illustrated by the red lines) was 1437 minutes. The circadian period of WT-1B observed during entrainment was 1440 minutes, while the free-running interval was 1430 minutes (Figure 1).

The circadian period of KO-2A observed during entrainment was 1437 minutes, although the activity of the mice extends into the (generally inactive) light phase. The free-running interval (illustrated by the red lines) was 1423 minutes. The circadian period of KO-2B observed during entrainment was 1441 minutes, with a second, smaller peak at 1422 minutes, while the free-running interval was 1420 minutes (Figure 2). During the last 12 days of the test, mouse KO-2A died of unknown causes. Around the same time, mouse KO-2B showed a total disorganization of its activity cycle, with no significant periodogram value able to be uncovered.

Experiment 2:

The circadian period of WT-3A observed during initial entrainment was 1439 minutes; the free-running interval (illustrated by the red lines) was also 1439 minutes, and the re-entrainment interval was 1439 minutes. The circadian period of WT-3B observed during

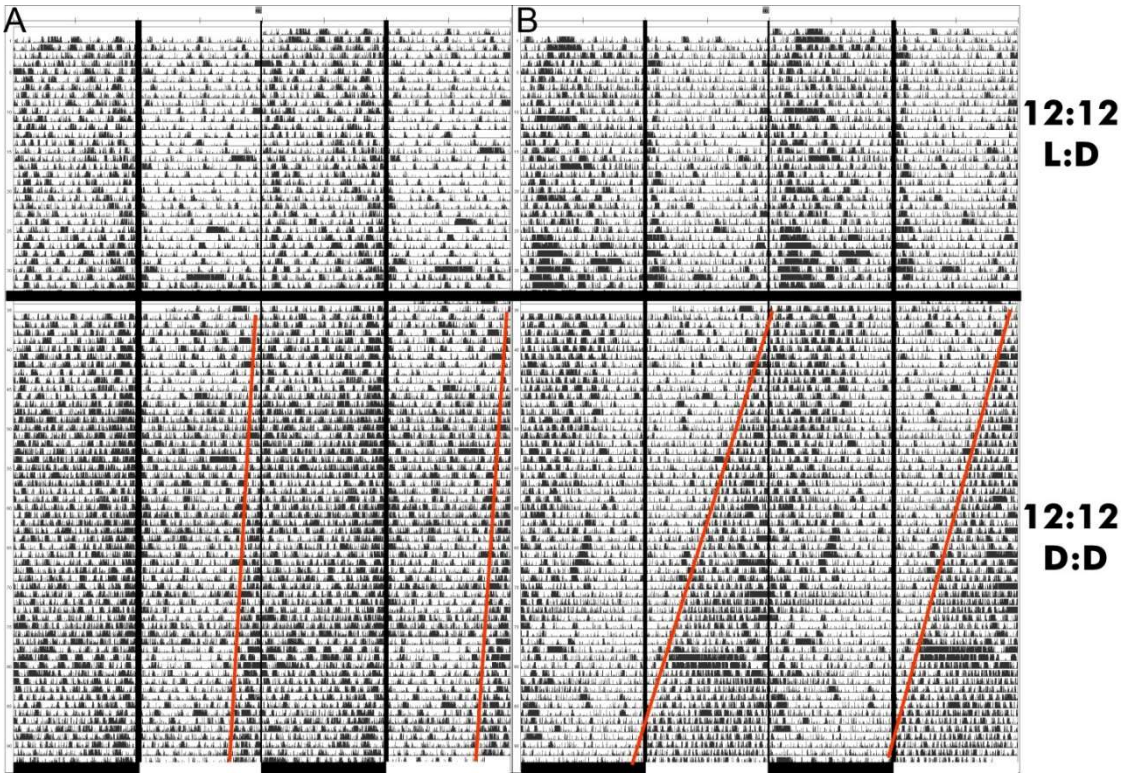

Figure 1. Wild-type mice, experiment 1. Entrained and free-running circadian rhythm of Wild-Type BALB-C mice. Two wild-type (A-B) mice were entrained on a 12:12 light:dark cycle for 33 days, followed by 60 days of constant dark (12:12 dark:dark). The horizontal bars represent the change from entrainment (light:dark) to free-running (dark:dark).

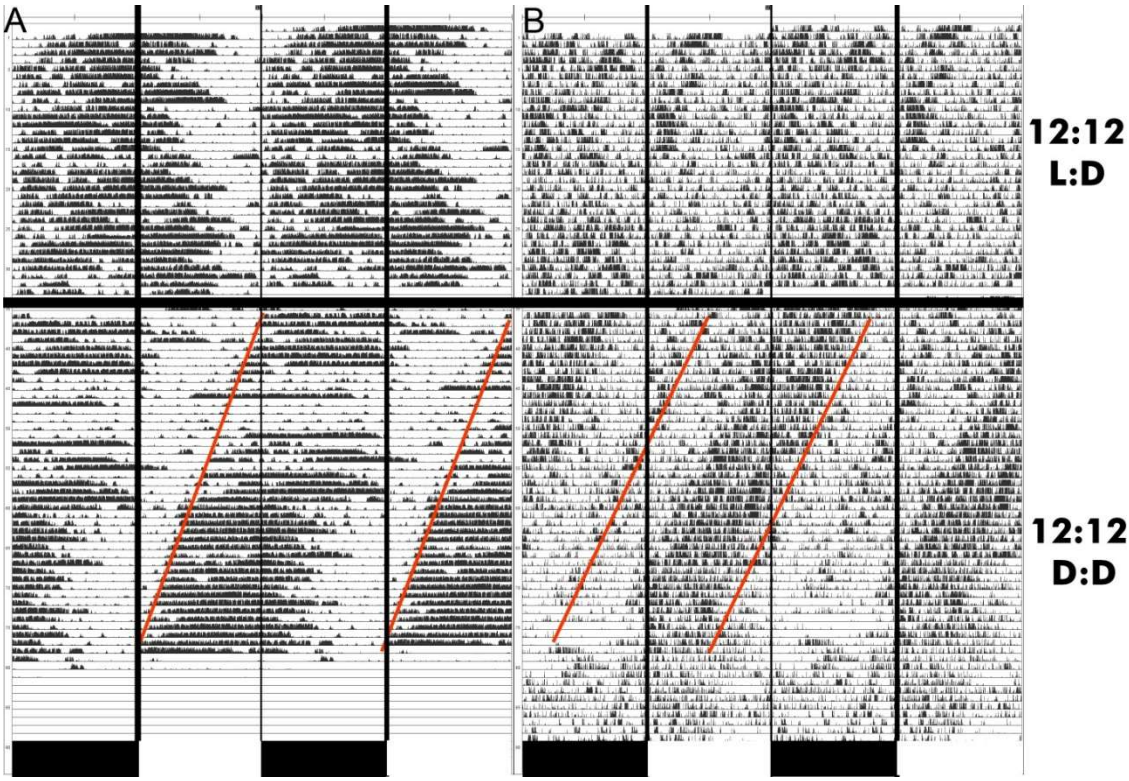

Figure 2. Knockout mice, experiment 1. Entrained and free-running circadian rhythm of S100B knockout BALB-C mice. Two S100B knockout (A-B) mice were entrained on a 12:12 (light:dark) cycle for 33 days, followed by 60 days of constant dark (12:12 dark:dark). The horizontal bars represent the change from entrainment (light:dark) to free-running (dark:dark).

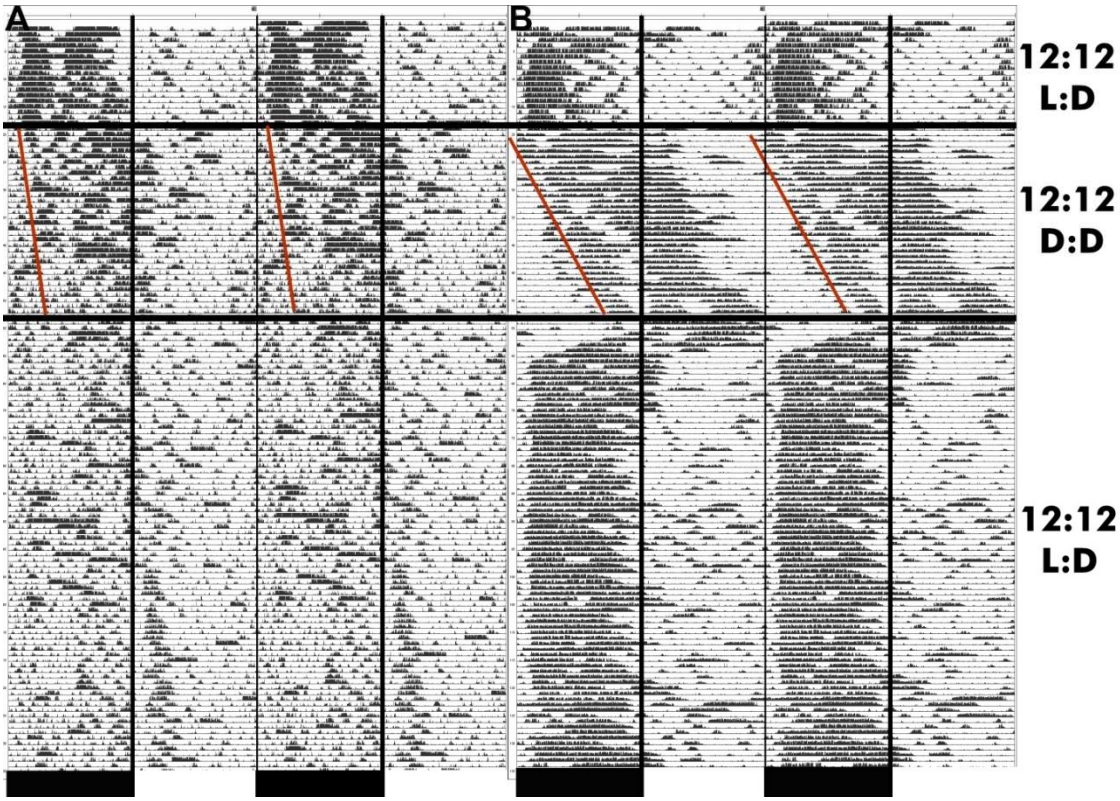

Figure 3. Wild-type mice, experiment 2. Entrained, free-running, and re-entrainment of circadian rhythm of Wild-Type BALB-C mice. Two wild-type (A-B) mice were entrained on a 12:12 (light:dark) cycle for 18 days, followed by 37 days of constant dark (12:12 dark:dark), followed by re-entrainment of a 12:12 (light:dark) cycle for 80 additional days. The horizontal bars represent the change from entrainment (light:dark) to free-running (dark:dark), and from free-running to re-entrainment.

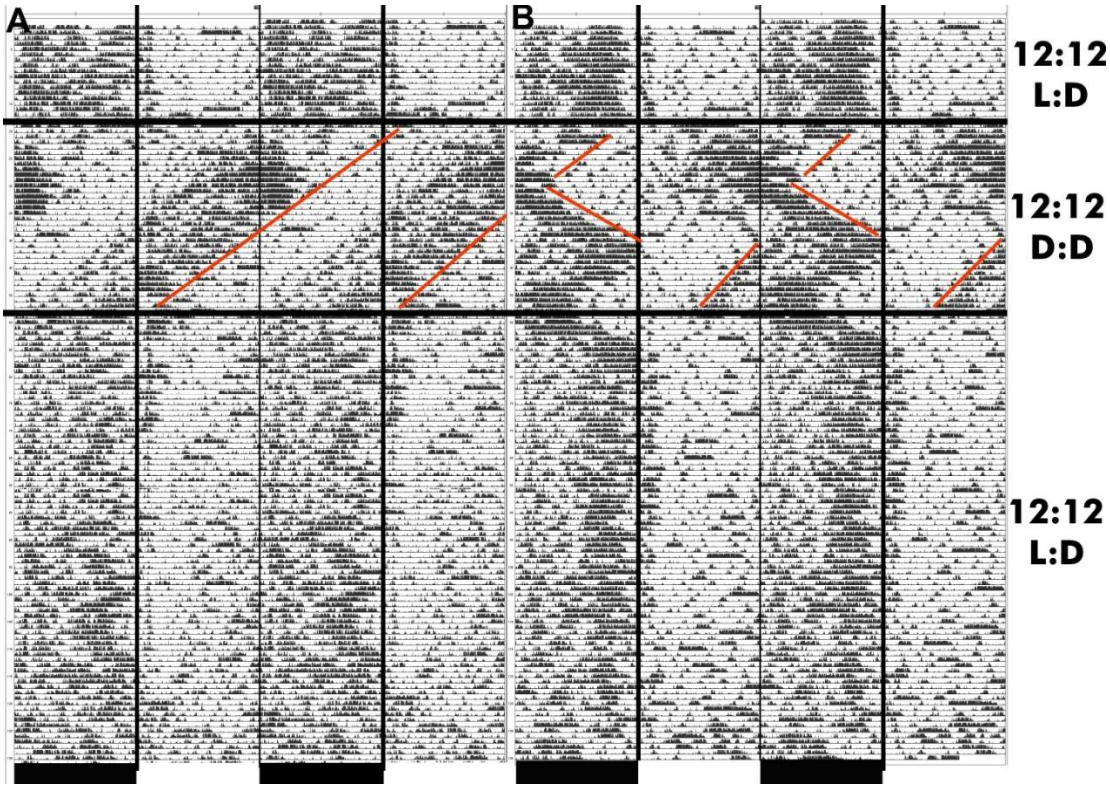

Figure 4. Knockout mice, experiment 2. Entrained, free-running, and re-entrainment of circadian rhythm of Wild-Type BALB-C mice. Two S100B knockout (A-B) mice were entrained on a 12:12 (light:dark) cycle for 18 days, followed by 37 days of constant dark (12:12 dark:dark), followed by re-entrainment of a 12:12 (light:dark) cycle for 80 additional days. The horizontal bars represent the change from entrainment (light:dark) to free-running (dark:dark), and from free-running to re-entrainment.

	Wild-type			S100B Knockout		
	Entrainment	Free-run	Re-entrainment	Entrainment	Free-run	Re-entrainment
1	1440	1437	n/a	1437	1423	n/a
2	1440	1430	n/a	1441	1422	n/a
3	1439	1439	1439	1440	1400	1440/(weak)1430
4	1437	1455	1440	1440	1451/1391	1440/(weak)1446

Table 1. S100B Periodogram times.

initial entrainment was 1437 minutes, while the free-running period was 1455 minutes; the re-entrainment period was 1440 minutes (Figure 3).

The circadian period of KO-4A observed during entrainment was 1440 minutes, while the free-running period (illustrated by the red lines) was 1400 minutes. The re-entrainment period was 1440 minutes, until the final 21 days of the study, during which the intervals of active behavior became disorganized, with a weak peak in the periodogram at 1430 minutes. The circadian period of KO-4B observed during initial entrainment was 1440 minutes. During free running, the observed period was 1451 minutes, with a second peak representing the change in free-running period of 1391 minutes. During re-entrainment, the period interval returned to 1440 minutes, until the final 24 days of the study, during which the activity behavior became disorganized, with a weak peak observed in the periodogram at 1446 minutes (Figure 4).

The results of both experiments are summarized in Table 1. The mean of free-running period in S100B KO mice was significantly shorter than in wild-type mice. In second experiment, in which the groups of mice were re-entrained after free-running, the S100B KO mice exhibited a weak, secondary circadian rhythm along with the light-entrained (1440-minute) rhythm.

1.5 Discussion

S100B is a biomarker of injury [33], age [34], inflammation [35], Alzheimer's disease [36], and cancer [37], and interest in this aspect has led to information useful to the current study—Emsley *et al*'s use of S100B as an astrocytic staining target demonstrated

S100B's presence in the SCN. S100B's intrinsic qualities as a novel calcium-sensitive binding protein came to prominence when it was found to bind with NCALD [30]. Further studies have rigorously described S100B as extant in circadian rhythm-related phototransduction and ganglionic tissue. It is also found to be curiously involved in the guanylate cyclase signal transduction system by modifying membrane-bound ROS-GC1, a separate modification from the one caused by NCALD, which is itself another of S100B's binding proteins. These studies also described its subtle influence on phototransduction [28, 29, 31].

A protein having widespread expression and specialized functions in differing cells may also have subtle and/or plural effects on circadian behavior. The current study has demonstrated three major differences in the circadian activity of S100B KO mice relative to wild-type counterparts: the presence of weaker, separate rhythm during periods of entrainment seen in 3 of the 4 S100B KO mice, with no such "ghost" rhythms in the wild-type mice; the behavior of the mice becoming more disorganized with statistically weaker periodogram values, at the end of the study, in 3 of the 4 S100B KO mice, with no such disorganization in the wild-type mice; and a significantly shorter free-running period in S100B KO mice compared to wild-type mice.

The presence of a less-organized, secondary rhythm observed during intervals of photoentrainment in S100B knockouts is complicated by the fact that the period of the secondary rhythms do not match the period seen during free-running in 2 of the 3 mice in which it was observed. The exception S100B KO mouse 2A's periodogram was a weak peak of 1422 minutes during photic entrainment, and a period of 1420 minutes during

the free-running interval. The other two mice, S100B KO mice 4A and 4B, showed a secondary rhythm thirty minutes longer than its 1400-minute period during free running and a secondary rhythm five minutes shorter than its free-running circadian period. If all KO mice showed an identical secondary rhythm to its free-running one, it might indicate that there was a weakening of photic entrainment. Entrainment to 1440 minutes was able to occur in all S100B KO mice, but the presence of the weaker rhythm may imply different changes in function: since the other EF-hand calcium-sensing protein, NCALD, is still present in S100B KO mice, it may have impressed an imperfect contribution to the activity cycle due to its periodic expression. NCALD has been shown to have periodic expression in *Drosophila*, and if mammalian NCALD has a similarly periodic expression, its period may have become desynchronized from that of the rest of the photic pathway. One unexplained phenomenon of this theory is how the S100B protein is necessary for NCALD to remain synchronous with the rest of the circadian rhythm nuclei.

The generalized disorganization noted in 3 of the 4 S100B KO mice included complete disorganization in one (mouse 2B), and only weak periods in mouse 4A and 4B. This degeneration of activity organization could be due to degeneration of tissues related to S100B's absence in circadian rhythm-related tissue such as the SCN, or could be related to more generalized effects. S100B, as stated above, is used as a biomarker of age. The presence of S100B has been posited as a possible regeneration-facilitative protein [38], and the lack of it in aged S100B KO mice could cause generalized pathologies, with scattered activity timing as one observed effect. Such an identification of relevant S100B

function could point toward further experiments of S100B knockouts observing other, more direct age-related functions.

The mechanism by which free-running circadian rhythms periods are shortened is poorly understood, but perturbation of the *VIP* and *Vipr2* genes leads to a shortened circadian period in a certain percentage of mice [39]. Deletion of the half of the PAS B and whole PAC subdomains *mPer2* gene caused both a shortening of free-running circadian rhythm, as well as an eventual disorganization of circadian activity. Further, PER2 rhythmicity requires calcium flux [40]. Perturbations of calcium flux by the absence of S100B may contribute to the effects seen in the present study.

Chapter 2: Short Ultradian Rhythms

2.1 Abstract

Ultradian rhythms are recognized in humans in the form of sleep cycling. Anxiety and depressive disorders disturb human sleep cycles, particularly in the measurement of rapid-eye movement (REM) bout length and non-REM sleep time. Behavioral aspects with a similar periodicity persist during waking. Rodents exhibit an analogous sleep cycle process involving a repeated switching between non-REM and REM states. In electroencephalographic (EEG) signal, delta and theta frequency band power parallels rodent non-REM/REM sleep cycling. We recorded EEG in rats over 24 hours and used spectral analysis of the delta (1-4 Hz) frequency band. We also used a semi-autonomous, discrete wavelet analysis of rat EEG focusing on the theta (5-10 Hz) frequency range. Most previous analyses of rodent ultradian rhythms investigate ultradian rhythms of an hour or longer. Here, we demonstrate a short ultradian rhythm (SUR), repeating approximately every 10 minutes, after analysis using both manual and semi-autonomous methods. We also show mouse locomotor activity exhibits a SUR that is approximately 8.6 minutes. These SURs may be influenced by redox conditions within sleep and wake-active brain nuclei.

2.2 Introduction

Biological rhythms occur at multiple scales. The generator of a circadian rhythm is a self-sustaining cellular oscillator which can be reset by external cues, can compensate for temperature differences within a physiological range, and which cycles over the

course of about one day [41-44]. Ultradian rhythms are biological rhythms which cycle in shorter intervals than 24 hours and exist in a wide range of organisms [45]. Whether there is a relationship between ultradian rhythms and circadian rhythms is not currently known.

The most well-characterized ultradian rhythm in humans is in sleep cycling. Studies of sleep behavior characterize the state of consciousness and/or alertness of the subject using electroencephalographic (EEG) data. EEG signal is sorted into putative frequency bands including delta (1-4 Hz), theta (5-10 Hz), alpha (8-12 Hz), beta (13-30 Hz), and gamma (31-100 Hz) [46]. Combinations of frequency range prominence denote the state of consciousness: wakefulness exhibits primarily alpha and delta bands, rapid eye movement (REM) sleep exhibits low-voltage delta band mixed with theta and gamma, and non-REM sleep exhibits high-amplitude prominence at the low-delta band and a minor alpha band aspect [47, 48]. The human sleep cycle, in which REM episodes terminate multi-stage non-REM intervals [49], repeats multiple times per night [47, 50], and exhibits a period of 90-120 minutes [51]. Depression is characterized by an alteration in EEG-defined sleep architecture [50], implying a central role of ultradian rhythms in affective disorders.

Humans also have ultradian rhythms in hormone secretion which are subject to change in response to variations in stress level and disturbance of sleep [52]. Pharmacological interventions can have differing effects based on the time of administration relative to ultradian rhythms (for review, see [53]). Humans exhibit several waking behavioral [54-59] and nocturnal hormone-secretory [60] oscillations which reflect the approximate

timing of non-REM/REM sleep cycling; both are posited to have the same underlying mechanism (for review, see [61]).

Non-REM/REM time intervals, matched by species-specific waking oscillatory behaviors, have been observed in rhesus monkeys [62], rats [63], cats [64], and mice [65]. The period of a non-REM/REM cycle in mice is reported to be ~10 minutes [66]. A 3.5-5-hour ultradian rhythm in mouse locomotor activity whose period does not respond to differing light cues has also been demonstrated [67].

Past studies have employed methods of inquiry based on a non-REM/REM sleep cycle analogous to the ones seen in humans. Inherent ambiguities involved with defining a sleep cycle in polyphasic rodents, whose sleep behavior is scattered over the 24-hour day, make systematic analysis of ultradian rhythms in rodents using EEG difficult [68].

We extracted spectral magnitude data from EEG signal in freely-moving adult rats corresponding to the delta and theta frequency ranges. Using a plot of the change in frequency band magnitude over entire sleep studies, we sought to identify cyclical features of this signal. We collected time indices of local minima in these bands and generated histograms of trough-to-trough intervals. We also used the same method of trough identification in locomotor activity of adult male mice.

Among all analyzed frequency bands of rat EEG and in mouse activity, we found an average ultradian time, or short ultradian rhythm (SUR), of approximately 10 minutes. In 12:12 light:dark lighting conditions, rat EEG data showed no significant difference between SUR timing during the light period versus SUR timing during the dark period. A

separate, semi-automated analysis of rat EEG using discrete wavelet analysis also demonstrated similar timing for SURs.

2.3 Materials and Methods

Experimental animals

Adult male wild type Sprague-Dawley rats were used for EEG experiments. Adult male BALB-C mice were used for locomotor activity studies.

Experimental chamber

For all experiments, rats and mice were housed individually within an electrically-shielded and sound-dampened Faraday chamber in which the temperature was maintained at ~23.3 °C, and relative humidity was kept at ~55%. Lights were kept on a 12:12 light:dark cycle.

E-Mitter transponder implantation surgery

For each surgery, a rat or mouse was placed in an induction chamber primed with 5% gaseous isoflurane at a flow rate of 2 LPM for 5 min, then placed on a platform maintained at 37 °C to prevent hypothermia. The gaseous mixture was reduced to 2.5% isoflurane at the same flow rate after attaching a nose cone to the surgical subject. Each E-Mitter Transponder (Mini Mitter, Bend, OR) was implanted through a 1 cm anterior-posterior midventral incision in the abdominal wall. Muscle and skin layers were closed with vicryl sutures, and bacitracin was applied topically. After surgery, all subjects were

injected intramuscularly with 0.125% bupivacaine. All procedures were approved by the Institutional Animal Care and Use Committee (IACUC) at Rutgers University.

EEG electrode implantation surgery

In rats, after implantation of E-Mitter transponders, surgery was continued to implant EEG electrodes. Rats were turned over and attached to a stereotaxic device. A midline scalp incision was made to expose the skull approximately 0.6 cm anterior of and 1 cm posterior of bregma. After incision, tissue/musculature was cleared away from the skull surface and the resulting bleeding was stanched.

With a 0.0125" drill bit, holes were made in the bone according to the medial-lateral (ML) and anterior-posterior (AP) coordinates of the desired locus with respect to bregma. Four holes were partially drilled, one in each quadrant of the skull surface, to place a 0–80 stainless steel screw into each hole (coordinates: ±3 mm ML, ±3 mm AP, relative to bregma). Each screw was attached to a 1.5-cm length of 0.010-inch, Teflon-coated stainless-steel wire with an Amphenol socket at the end. Stripped ends of two more wires were implanted in the dorsal neck muscle for electromyographam (EMG) data. The other ends of EMG wires were stripped ~2 mm and soldered to an Amphenol socket. EEG and EMG electrode sockets were inserted into a plastic screw-socket, and the entire assembly was encased in dental acrylic, leaving the top exposed for connection to data-collection hardware. Bacitracin was applied topically to the periphery of the wound.

Data collection and analysis

The implanted electrodes were connected via a shielded cable to a multichannel Model 15 amplifier (Grass Technologies, West Warwick, RI). Fronto-occipital EEG, Bifrontal EEG, and an EMG trace were recorded for each rat. EEG, EMG, and activity were monitored for 24 hours. Collection and manipulation of EEG data was performed in Spike2 software (Cambridge, UK).

All locomotor activity data were collected via the E-Mitter transponder; activity counts were collected by comparing relative signal strength over time to a receiver box underneath the experimental apparatus. Activity counts (arbitrary unit) were summed over 15-second intervals.

After data collection, the EEG/EMG signal for each rat was separated into sequential 30-second epochs. A magnitude coefficient was generated from a Fourier transform of each epoch, and plots for whole EEG studies were made based on these values in sequence (see Figure 1). Power plots were generated from the 1-8 Hz frequency band (see Figure 2), with additional plots generated from the 1-4 and 4-8 Hz frequency sub-ranges. The bifrontal EEG channel served as the basis of spectral magnitude plots.

A trained investigator visually inspected both rat spectral magnitude plots and mouse locomotor activity plots, marking the time indices of local minima, or troughs. Trough-to-trough time differences were collected, and histograms were generated using SigmaPlot (London, UK). Histogram trough-to-trough time was separated into half-minute bins.

Discrete wavelet analysis

EEG data recorded at a 100 samples/second were exported in 2-hour segments into the Matlab Wavelet Toolbox as one-dimensional arrays. The Toolbox preset Coiflet 1 wavelet was found to be most effective for denoising EEG data. Spikes corresponding to biological signals were identified in decomposition level 4 in the Wavelet Toolbox, corresponding to the 5-10 Hz (theta) frequency range. The signal was denoised using an unscaled white noise filter, with the resulting plot focused on this scale. After denoising, peaks were identified, and a histogram was generated using the peak-to-peak intervals. Histogram time was separated into half-minute bins.

2.4 Results

Mouse body temperature, rat body temperature, and rat locomotor activity showed no observable peaks under these experimental conditions (data not shown).

Histograms generated from identifying local minima in several different frequency bands yielded a consensus SUR interval. The most recurrent SUR time for the 1-4 Hz frequency band was 8.5 minutes (n = 40), with a mean ultradian period of 11.1 ± 0.34 minutes (n = 623) (Figure 3A). Equally recurrent ultradian periods of 9 and 5.5 minutes (n = 21) were seen in the 4-8 Hz frequency band, with a mean ultradian period of 9.3 ± 0.32 minutes (n = 408) (Figure 3B). For the 1-8 Hz frequency band (Figure 3C), the most recurrent ultradian period was 10 minutes (n = 22), with a mean ultradian period of 12.8 ± 0.41 minutes (n = 467). However, no significant difference in ultradian period was observed between the light and dark phase for the 1-8 Hz frequency band, as

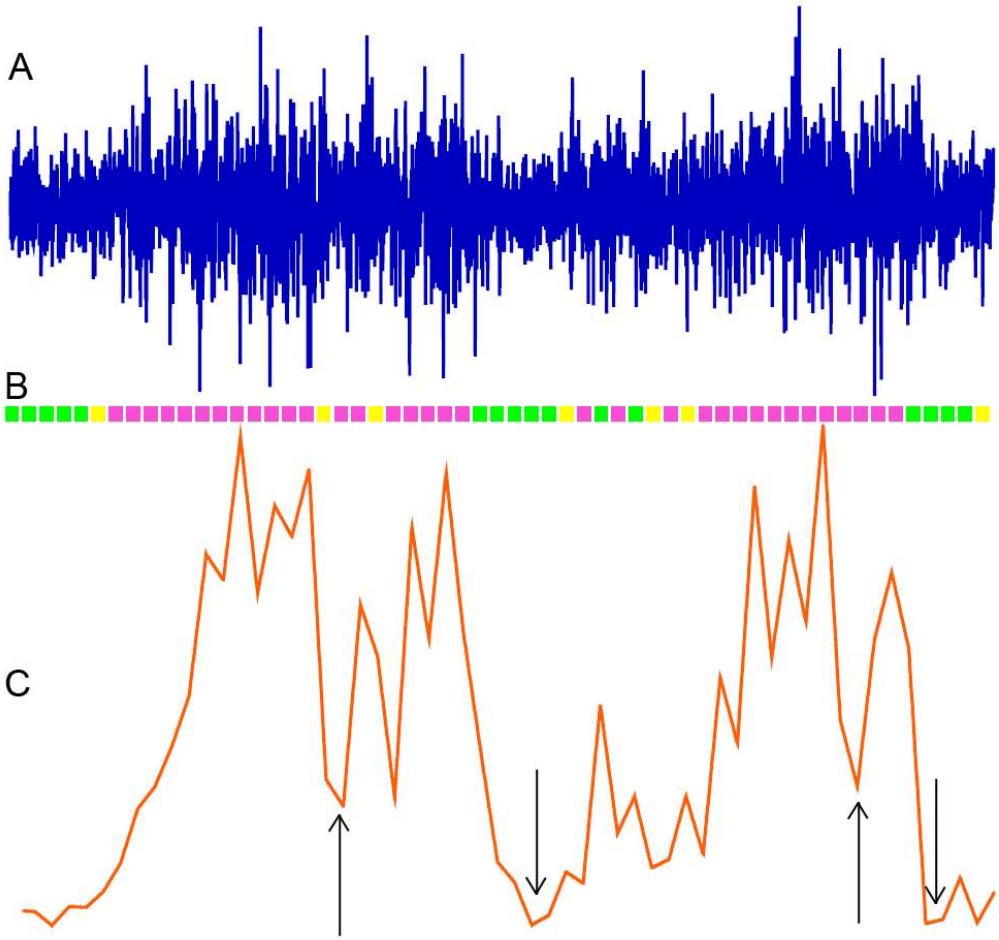

Figure 1. Example of raw EEG, sleep staging, and Fast-Fourier spectral power plotting. (A) Raw EEG taken from an adult male rat. During determination of consciousness state, researchers looked at the EEG waveform expanded to show only the width of raw signal within the span of one of the squares in (B). Identified sleep states are color-coded (nREM sleep = pink, wakefulness = yellow, REM sleep = green). Additionally, for each 30-second interval, the Fast-Fourier-derived spectral power of the entire 1-8 Hz frequency band was displayed, and could be seen as a new waveform when viewing larger intervals of data (C). Troughs in the 1-8 Hz spectral power (indicated by arrows) denote a significant change in waveform composition, and often indicate a change in consciousness state. “By eye” trough identification used these spectral power plots to identify the timestamp of possible consciousness state changes.

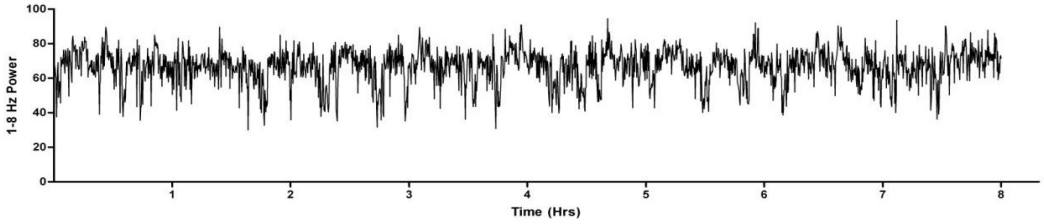

Figure 2—Spectral magnitude of 1-8 Hz frequency range of rat EEG data over time. Illustrative trace of the summed 1-8 Hz frequency of rat EEG. The repeating, downward trends in the trace represent a decrease in prominence of this frequency band.

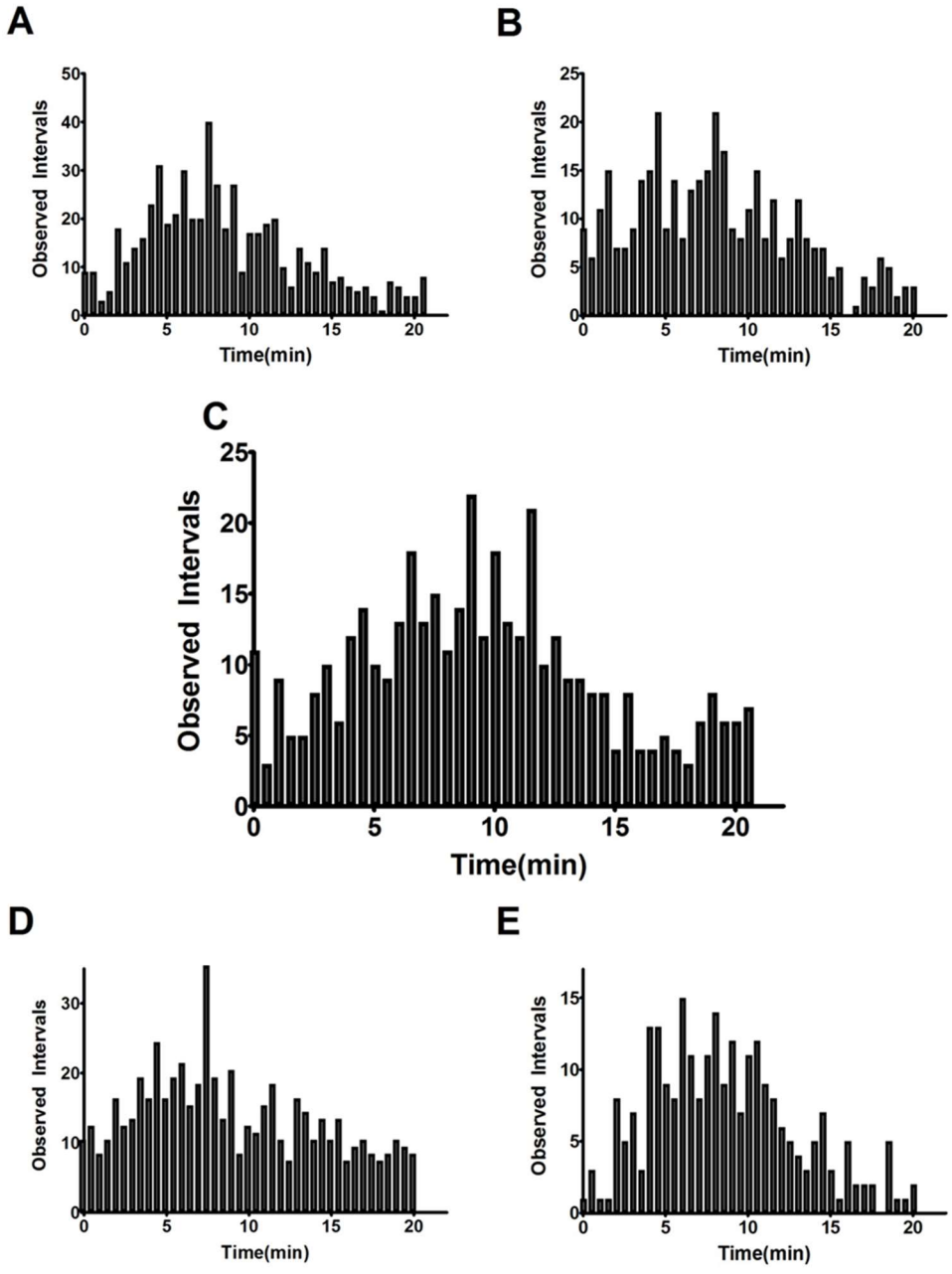

Figure 3. Histogram of SURs according to variable frequency ranges and periods during the day. Analysis of summed spectral magnitude of EEG frequency bands. (A) Shows the 1-4 Hz frequency. (B) Shows the 4-8 Hz frequency band. (C) Shows the 1 -8 Hz frequency band. Ultradian period is shown during the light (D) and dark (E) phase for the 1-8 Hz frequency band.

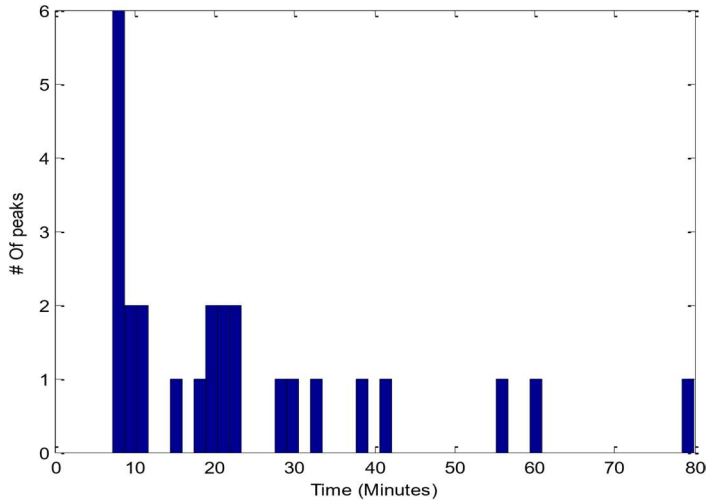

Figure 4—Histogram of cyclical EEG signal activity from adult male rat. Raw EEG data, recorded at a 100Hz sampling rate, was exported into one-dimensional arrays corresponding to 2 hours of data, and was then imported into the Matlab Wavelet Toolbox for processing. The data was denoised using the Coiflet 1 mother wavelet at decomposition level 4. The result is an analysis of the general wave pattern presented as histogram of spike-to-spike time intervals. Figure was generated with Dennis Egen.

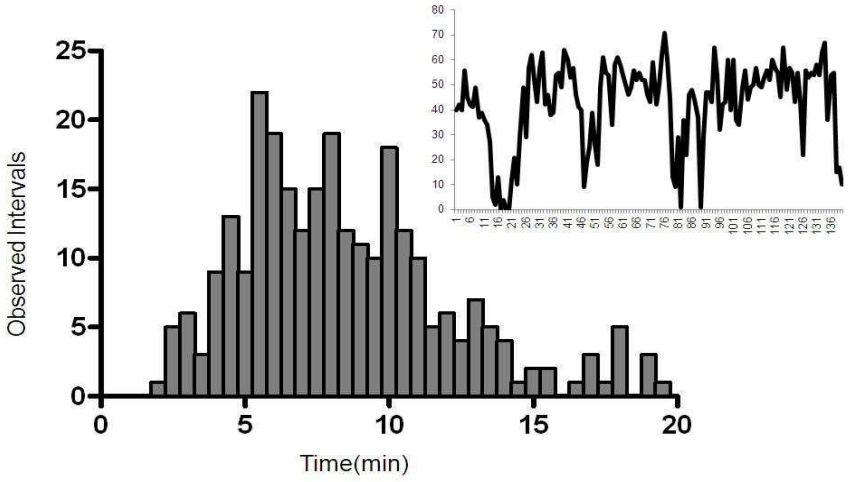

Figure 5—Interval distribution of mouse locomotor activity by time. Raw locomotor activity (inset) was recorded from mice in 15-second intervals via a surgically implanted transponder. Time between local minima was calculated to determine the ultradian period during the dark (active) phase.

depicted in (Figure 3D) and (Figure 3E), respectively ($p = 0.08$, paired t-test). All ± values of calculated means denote SEM.

Analysis of raw EEG using discrete wavelet transform showed an average SUR of 11.5 minutes (SD = 5), with 80% of the spikes within the 9-13-minute range (Figure 4). Spike detection using this method also showed quantization effect of this ~10-minute rhythm, with smaller, diminishing histogram peaks at multiples of ten minutes.

For mouse locomotor activity (Figure 5), mean SUR was calculated to be 8.6 ± 0.26 minutes.

2.5 Discussion

We show a robust indication of a new short ultradian rhythm, or SUR, after analysis of EEG, using two separate methods, one manual and one semi-automated. This also indicates the first analysis of raw EEG from adult male rats to determine such a rhythm. We also show that locomotor activity of mice exhibits a similar rhythm as determined by manual methods.

Circadian rhythms were thought to be subject exclusively to transcription/translation oscillations (TTOs), in which the transcription of promoters induces the transcription of repressors, forming a negative feedback loop which repeats daily [69]. However, metabolic oscillations (MO) can maintain a rhythm in the absence of a TTO. Enzymes in human red blood cells, known as class-2 peroxiredoxins, dimerize and oligomerize as they are inactivated, accumulating reactive oxygen species within a cell [70]. The oligomerization pattern was found to be cyclic and self-sustaining over a 24-hour

period, and the peroxiredoxin oxidation cycles were synchronized to temperature cues. Since red blood cells do not contain nuclei, these processes occur in the absence of genomic feedback [70].

Investigations of longer ultradian rhythms (on the order of 1-2 hours) in both humans and rodents show hormone release correlative with changes in EEG spectral magnitude [71, 72]. Perturbation of the dopamine transporter gene lengthens the period of longer ultradian locomotor rhythms in mice [73]. Recently, several gene-expression ultradian rhythms have been identified in the 3-13-hour range [74]. Ultradian rhythm periodicity ranges from hours to seconds; although TTOs may influence longer ultradian rhythms, the time course of the SURs in this study may preclude genetic control.

The suprachiasmatic nucleus (SCN), which controls circadian rhythms in mammals, is neither necessary nor sufficient to generate ultradian rhythms in the small rodents [75, 76]. However, oscillatory short-term changes in brain metabolic species occur in other nuclei and tissue types. Extracellular glutamate and lactate levels drop while the concentration of cerebral glucose increases during non-REM sleep [77-82]. Noradrenergic and acetylcholine neurons are dramatically suppressed during non-REM sleep, although cholinergic activity rebounds during REM sleep (for review see [83]). During non-REM sleep, cerebral metabolism shifts from aerobic glycolysis to oxidative phosphorylation [84]. ATP concentration surges in wake-active areas during spontaneous sleep in rats, but not in sleep active nuclei [85]. This surge is posited to be due to lack of ATP degradation rather than increased ATP synthesis [86], and increased ATP in these nuclei, inhibitory to cytochrome c oxidase [87], #0}, may prevent

accumulation of reactive oxygen species [86]. MOs and TTOs may be partially influenced or controlled by the redox condition in cells.

While the non-REM/REM sleep cycle in humans cycles several times throughout a single long sleep bout per 24-hour day [47, 50], rodent polyphasic sleep introduces some ambiguity in what can be identified as a sleep cycle. Rodents are typically active in the dark phase and inactive in the light phase; the inactive phase encompasses about 57-59% of sleep in a given 24-hour day, with more sporadic sleep during the active phase [88]. Since nearly all non-REM/REM bouts are interrupted by wakefulness in rodents, the amount of incidental wakefulness tolerated before identifying the following bout of sleep as part of the former or latter sleep bout is not well-characterized. The more reliable measure of sleep ultradian rhythms is demonstrated to be the interval between successive bouts of REM sleep [68].

Perturbation of mechanisms involved with metabolic oscillatory species affects non-REM/REM sleep behavior. Mice deficient in norepinephrine-synthesizing dopamine β-hydroxylase (Dbh -/-) show decreased sleep latency after stressful events [89]. Mice missing the β-2 subunit of nicotinic acetylcholine receptors show longer bouts of REM sleep and more consolidated non-REM sleep [90]. Alpha-9 acetylcholine receptor knockout mice exhibit longer non-REM and REM sleep episodes and higher delta activity during non-REM sleep [91]. These perturbations, independent of TTO mechanisms, may implicate MOs as necessary for sleep-related ultradian rhythms.

Traits of the spectral magnitude over time correlate with consciousness states: a decrease in delta corresponds to transfer into REM sleep in humans [47, 48], and theta becomes prominent during periods of REM in rodents [92]. Previous studies using EEG for ultradian rhythm detection employed statistical correlation methods, which require extensive preprocessing of EEG data [68]. Wavelet analysis has been used to interpret singular electrooculogram waveform data events in rats to detect REM sleep, and to interpret locomotor activity in mice in 15-minute bins, yielding the detection of ultradian rhythms with period lengths of one hour or more [93, 94].

In the present work, we identified ~10-minute SUR timing through two separate methods: rapid decreases in delta activity were used to manually mark time indices and generate histograms, whereas the semi-automated discrete wavelet method used increases in theta prominence. The two measures of SURs occur at the same point within sleep architecture and yield similar periods. These measurements may correlate with the cyclical activity of MOs in the brain, and may extend into wakefulness and activity behavior, as suggested by the SUR we demonstrate in mice. The exact mechanisms leading to the cyclical rises and falls of metabolic species in brain tissue are still not completely understood. Future experiments may systematically demonstrate the differences in SURs of rodents with perturbations of known MO-active compounds and receptors using semi or fully-automated discrete wavelet analysis.

Chapter 3: AMP phosphatase (CD73) knockout affect affects sleep in mice

3.1 Abstract

In brain, extracellular adenosine triphosphate (ATP) and its metabolic derivative, adenosine, regulate sleep by activation of distinct receptors. ATP extracellular concentration varies with non-rapid-eye-movement (non-REM) sleep, and ATP-gated receptor agonists and inhibitors affect sleep. Extracellular adenosine accumulates with sleep deprivation and declines during recovery sleep. Intracerebroventricular and intraperitoneal adenosine injections increase sleep. Adenosine receptor antagonists reduce sleep, while agonists generally increase sleep. Ecto-5'-nucleosidase (CD73) catalyzes one process of the biochemical reaction chain metabolizing ATP to adenosine by converting adenosine monophosphate (AMP) to adenosine. Here, we show that mice lacking CD73 demonstrate different amounts of wakefulness and REM sleep when compared to wild-type mice, challenging the results of a contemporary study. We also demonstrate different locomotor activity by CD73 knockout mice during recovery after sleep deprivation, with no such difference in locomotor activity seen in wild-type mice during the same recovery phase. As extracellular adenosine is mediated by several mechanisms in brain tissue, these results are consistent with a role of adenosine in sleep, and a sensitive but robust homeostatic mechanism governing adenosine extracellular concentration.

3.2 Introduction

Sleep regulation is linked to accumulation of adenosine triphosphate (ATP) in mammalian brain tissue. ATP concentration surges in wake-active brain nuclei as non-rapid-eye-movement (non-REM) electroencephalographic (EEG) activity increases during sleep in mice, an effect which can be abolished by preventing sleep [85]. Intracerebroventricular injection of the ATP-gated purine type 2 receptor (P2R) agonist 2'(3')-O-(4-benzoylbenzoyl)adenosine 5'-triphosphate promotes non-REM sleep, and injection of P2R antagonists reduces spontaneous non-REM sleep [95]. P2Rs stimulate astrocytic release of cytokines interleukin-1 beta (I1β) [96] and tumor necrosis factor alpha (TNFα) [97] from glial cells, both of which increase non-REM sleep after intracerebroventricular injection [98, 99]. ATP is released to the extracellular compartment by the hemichannel pannexin 1 [100] and during neurotransmission [101, 102], making ATP a transient marker of short-term summed cell signaling. ATP is rapidly catalyzed in the extracellular space to adenosine diphosphate (ADP), adenosine monophosphate (AMP), and adenosine.

Adenosine is another endogenous sleep factor. Intracerebroventricular injection of adenosine increases sleep in cats [103], as do intraperitoneal injections of adenosine agonists in mice and rats [104, 105], although this effect is under some debate [106]. Caffeine, a methylxanthine enjoyed by many [107], antagonizes A_1 and A_2 adenosine receptors, increasing sleep latency and fragmenting non-REM sleep [107, 108]. *In vivo* microdialysis of cat brain demonstrates extracellular adenosine decline during sleep, whereas in cortex and in the cholinergic region of the basal forebrain, adenosine increases with sleep deprivation and returns to baseline slowly during recovery [109].

This slow return to baseline may be due to basal forebrain cholinergic neurons' quiescence during sleep. The commensurately diminishing time course in EEG delta activity through the night may reflect the extracellular decline in accumulated adenosine [110].

Extracellular concentration of adenosine decreases while ATP concentration surges during non-REM sleep [85, 109]. Since ATP is an adenosine precursor in the extracellular compartment, perturbations of ATP metabolism should change sleep behavior and/or locomotor activity. Ecto-5'-nucleotidase (AMP phosphatase or CD73), a marker of astrocytes [111], regulates extracellular adenosine concentration by hydrolyzing AMP to adenosine (reviewed in [112]).

We compared EEG-defined sleep, core body temperature, and locomotor activity of CD73 knockout (KO) mice with those of wild-type mice in 12:12 light:dark conditions for 72 hours. We also compared locomotor activity during sleep deprivation recovery in CD73 KO mice with that of wild-type mice. Here we demonstrate statistically distinct sleep behavior by CD73 KO mice compared to wild-type mice. We also demonstrate statistically distinct locomotor activity of CD73 KO mice during the recovery period following sleep deprivation when compared to its sleep-deprivation-free control day, a distinction not observed in wild-type mice. These data illustrate perturbation of the ATP/adenosine biochemical pathway's effect on EEG-defined sleep and locomotor activity.

3.3 Materials and Methods

Experimental animals

Adult male BALB-C wild-type and CD73 KO mice were used for all studies.

Experimental chamber

For all experiments, mice were housed individually within an electrically-shielded and sound-dampened Faraday chamber where the temperature stayed at ~23.3 °C, and relative humidity at ~55%. Lights were kept on a 12:12 light:dark cycle.

E-Mitter transponder/EEG electrode implantation surgery

For each surgery, a mouse was placed in an induction chamber primed with 5% gaseous isoflurane at a flow rate of 2 LPM for 5 min. After loss of consciousness, mice were placed on a platform maintained at 37 °C. Gaseous mixture was reduced to 2.5% isoflurane after attaching a nose cone to the mouse. Each E-Mitter Transponder (Mini Mitter, Bend, OR) was implanted through a 1 cm anterior-posterior midventral incision in the abdominal wall. Muscle and skin layers were closed with vicryl sutures, and bacitracin was applied topically.

After implantation of E-Mitter transponders, mice were turned over and attached to a stereotaxic device. A midline scalp incision was made to expose the skull approximately 0.5 cm anterior of and 0.5 cm posterior of bregma. After incision, musculature and connective tissue were cleared away from the skull surface.

Locations on the skull are designated according to the medial-lateral (ML) and anterior-posterior (AP) coordinates of the desired locus with respect to bregma. Four holes, one

in each quadrant of the skull surface, were drilled with a 0.0125" drill bit to place a 0–80 stainless steel screw into each hole (coordinates: ± 1.5 mm ML, ± 1.5 mm AP, relative to bregma). Each screw was attached to a 1.5-cm length of 0.010-inch, Teflon-coated stainless-steel wire with an Amphenol socket at the end. EEG electrode sockets were inserted into a plastic screw-socket, and the entire assembly was encased in dental acrylic, leaving the top exposed for connection to data-collection hardware. After surgery, all mice were injected intramuscularly with 0.125% bupivacaine and bacitracin ointment was applied topically to the periphery of the wound. All procedures were approved by the Institutional Animal Care and Use Committee (IACUC) at Rutgers University.

Data collection and analysis

The implanted electrodes were connected via a shielded cable to a multichannel Model 15 amplifier (Grass Technologies, West Warwick, RI). Fronto-occipital EEG and bifrontal EEG were recorded for each mouse. Collection and manipulation of EEG data was performed in Spike2 software (Cambridge, UK).

All locomotor activity data was collected via the E-Mitter transponder; activity counts were collected by comparing relative signal strength over time to a receiver box underneath the experimental apparatus. Activity counts (arbitrary units) were collected in 15-second intervals.

After data collection, Thomas D. James analyzed EEG data offline, unaware of experimental conditions. Each 72-hour record was band-passed (1 – 30 Hz) with a 20 Hz

notch filter in order to minimize effects of ambient electrical signals. Records were evaluated in 30-second epochs and a state of consciousness (non-REM, REM, or waking) was assigned according to standard criteria [106]. Data were analyzed in 1-hour bins using a 2-way analysis of variance (ANOVA) on GraphPad Prism version 5.00 for Windows (GraphPad Software, San Diego, California, USA, www.graphpad.com).

Experiment 1: EEG-defined sleep, locomotor activity, and core body temperature

EEG, body temperature, and locomotor activity in wild-type (n=3) and CD73 KO (n=3) mice were monitored for 72 hours (start time: 19:00). Each consciousness state was quantified by the percentage of time spent in that state per hour. Locomotor activity was determined as each mouse's total activity over each hour during recording. Core body temperature was given as the normalized, average core body temperature during each hour throughout recording.

Experiment 2: Sleep deprivation/recovery activity

At 09:00 on day 1 (control day), temperature and activity data were recorded in wild-type (n = 4) and CD73 KO (n = 3) mice for 24 hours with no intervention. On day 2 (sleep deprivation/recovery day), all mice were sleep-deprived using periodic paint-brush sensory stimulation and gentle handling for 6 hours during the light phase (09:00-15:00) (data from 09:00-11:00 not shown). All mice were then allowed to recover as locomotor activity recording continued until 09:00 the next morning. Activity samples were normalized relative to the maximum 15-second activity sample of each individual mouse, and activity per 15 minutes was summed.

3.4 Results

In Experiment 1, each consciousness state was quantified as the percentage of time spent in that state per hour. A two-way ANOVA revealed that CD73 KO mice exhibited statistically different amounts of wakefulness (Figure 2A) and REM sleep (Figure 2C) when compared to wild-type mice ($p < 0.0001$, $p < 0.0001$, respectively; n = 3 wild-type, n = 3 KO). Upon inspection of the graphs, CD73 KO mice seem to exhibit higher amounts of wakefulness on the second dark/light phase, and lower amounts of REM sleep throughout the 72-hour study. Non-REM sleep (Figure 2B) was not significantly different between genetic conditions.

Locomotor activity in Experiment 1 was portrayed as each mouse's total activity over each hour during recording. A two-way ANOVA revealed no statistical difference between wild-type and CD73 KO mice. Similarly, a two-way ANOVA revealed no statistical difference between core body temperature in wild-type and CD73 KO mice.

In Experiment 2, each mouse's activity was normalized relative to its own maximum activity, and activity per 15 minutes was summed. The two-way ANOVA showed no statistical difference between post-sleep-deprivation recovery activity and the corresponding interval during control day for wild-type mice. However, a statistical difference between post-sleep-deprivation recovery locomotor activity and the corresponding interval during control day for wild-type mice was observed ($p = 0.027$). Inspection of the graph reveals a possible decrease in activity of CD73 mice on the sleep deprivation/recovery day after the initial increase in activity at the beginning of the dark

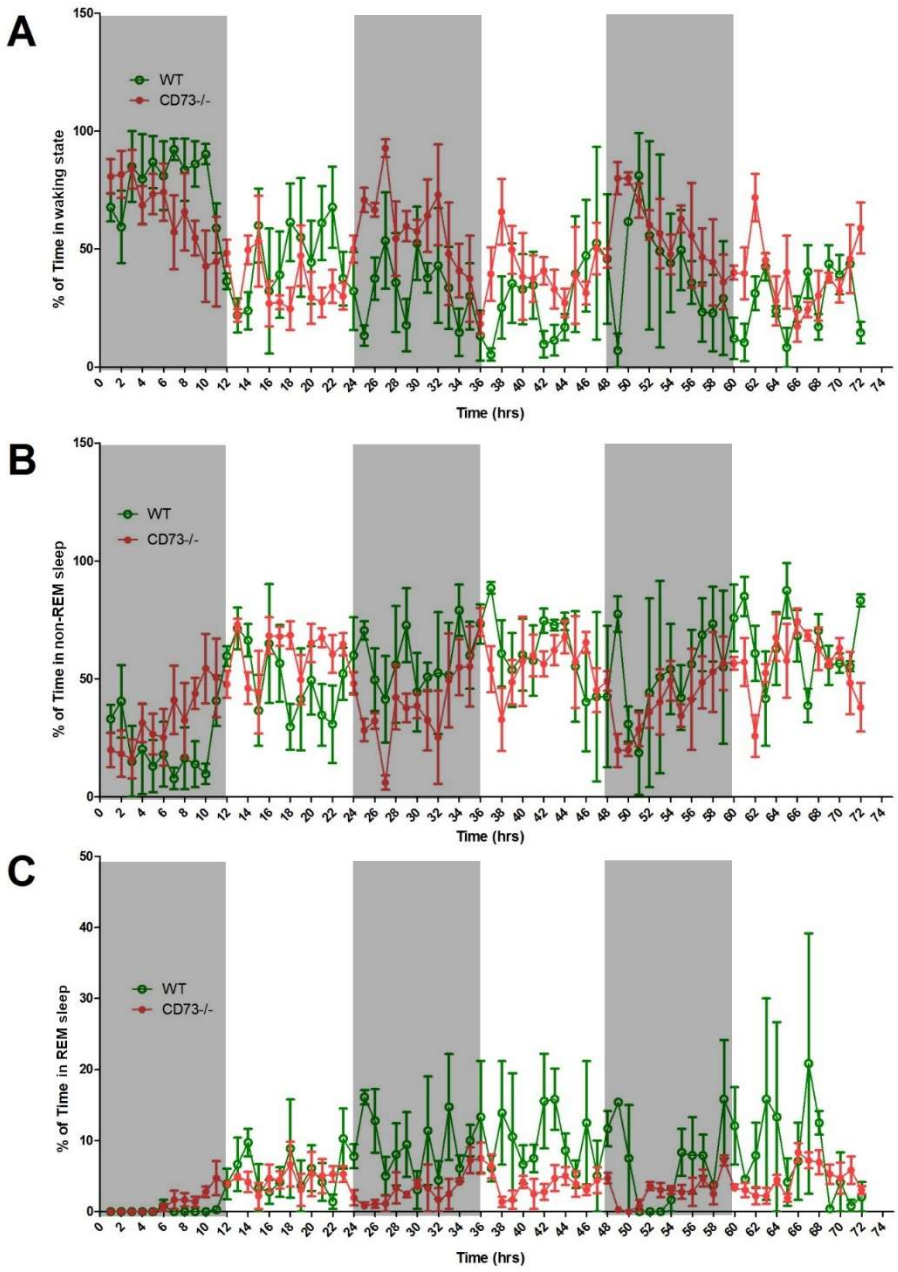

Figure 1. Differences in EEG-defined states of consciousness between adult male wild-type and CD73 -/- mice. Wild-type (green hollow circles) and CD73 -/- mice (red filled circles) EEG data were recorded for 72 hours. Amount of time spent in (A) non-REM sleep, (B) wakefulness, or (C) REM sleep are portrayed as the percentage of time in that state per hour of recording. Gray areas on graphs denote the dark phase. For both groups of mice, n = 3. Error bars denote standard error of the mean (SEM).

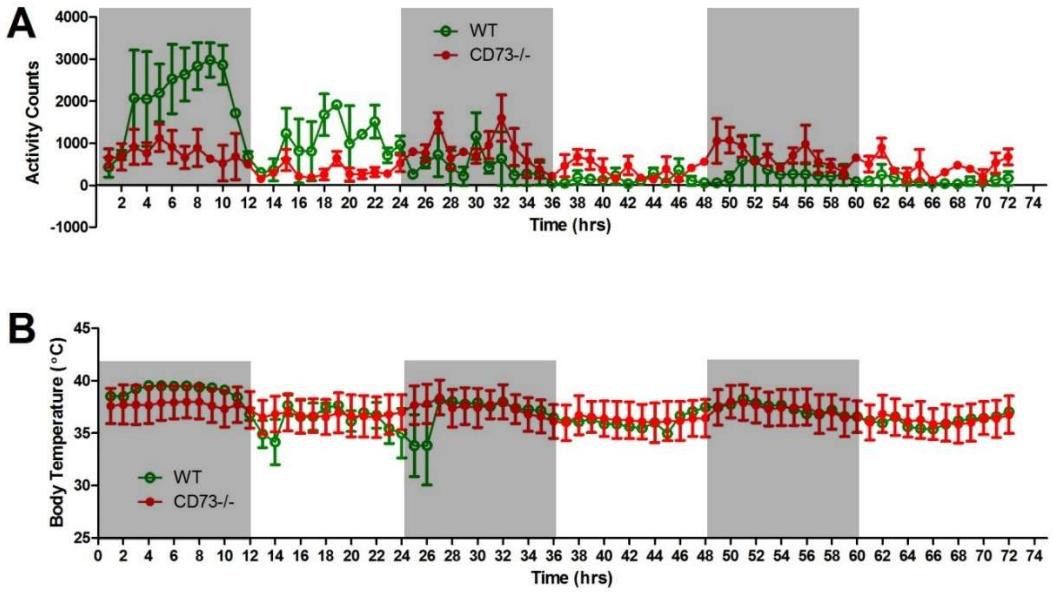

Figure 2. Locomotor activity and core body temperature between adult male wild-type and CD73 -/- mice. Wild-type (green hollow circles) and CD73 -/- mice (red filled circles) were subject to 72 hours of temperature and locomotor activity data recording. (A) Locomotor activity was expressed as the sum of mouse activity over each hour. (B) Core body temperature was expressed as the average body temperature over each hour. Gray areas on graphs denote the dark phase. For both groups of mice, n = 3. Error bars denote standard error of the mean (SEM).

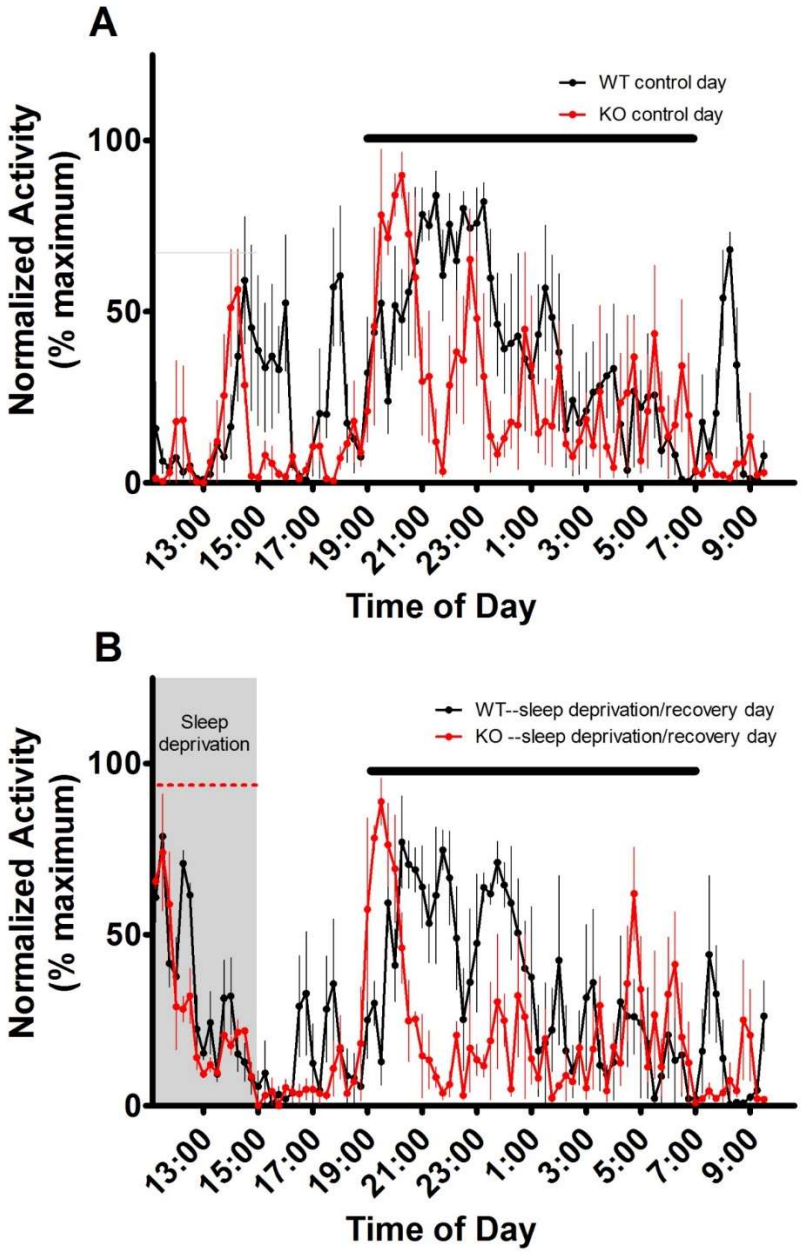

Figure 3. Effect of sleep deprivation on wild-type and CD73 knockout mice. Locomotor activity on (A) control day 1 and (B) sleep deprivation/recovery day 2 was recorded for 22 hours for wild-type (black trace) and CD73 KO (red trace) mice. Activity was normalized relative to the maximum activity in each individual mouse, and activity per 15 minutes was summed. Dotted line/gray area in (B) denotes sleep deprivation time. Black horizontal lines denote the dark phase. For wild-type mice, n = 4. For CD73 KO mice, n = 3. Error bars denote standard error of the mean (SEM).

phase. The activity seems to become indistinguishable from the control day's activity at the end of the dark phase.

3.5 Discussion

We show differing sleep behavior in CD73 KO mice when compared to control. ATP and adenosine have been identified as occurring in relation to non-REM sleep [85, 109]; however, our data shows a change in wakefulness and REM sleep.

In a larger and more comprehensive investigation published near the time of data collection for the present study, CD73 KO mice were demonstrated to increase EEG-defined non-REM sleep. C57BL/6J control mice showed enhancement of non-REM sleep after sleep deprivation, whereas CD73 KO mice showed no such enhancement [113]. These contradictory results may have been due to the control mice used in their study: differential sleep behaviors, notably in REM sleep after stress, are demonstrated by C7BL/6J and BALB/C mice, and within-strain C57BL/J mice exhibit differential non-REM and REM sleep behaviors [114]. Use of BALB/C control mice may have influenced manifestations of comparable sleep behavior in CD73 KO mice.

The enzyme adenosine kinase (AK) mediates adenosine content by converting it to AMP. AK overexpression leading to net decreased adenosine [115], increased wakefulness, decreased REM sleep, and decreased compensating delta activity in mice after sleep deprivation [116] when compared to mixed-background 129/JEms × C57Bl/6 controls. Here we show that CD73 KO mice demonstrate statistically different wakefulness and REM sleep when compared to wild-type mice. We also show that CD73 mice have

different activity profiles during recovery after sleep deprivation than do wild-type mice. Knockout of the catalyst responsible for conversion of AMP to adenosine may have similar effects as AK overexpression on extracellular adenosinergic tone, and if so, may account for the results seen here. Decreased extracellular adenosine may result in a decreased gating of A_1 and A_2 receptors, leading to increased wakefulness, as seen in previous studies involving A_1 and A_2 receptors [117, 118].

The absence of ecto-5'-nucleosidase interrupts conversion of AMP to adenosine, but extracellular adenosine can be derived from several sources. Prostatic acid phosphatase also converts AMP to adenosine; it is implicated in pain control [119, 120] and occurs in brain [121]. CD73 KO mice show spike-evoked accumulation of adenosine in the extracellular compartment of cerebellar slices; this accumulation is blocked by bafilomycin, a synaptic vesicle-refilling inhibitor, implying that adenosine can be released to the extracellular compartment directly and without breakdown from extracellular ATP [122]. Equilibrative nucleoside transporters can regulate concentration of extracellular adenosine [123]. AMP itself can activate adenosine receptor A1 [124]. Homeostatic mechanisms may exist to compensate for the perturbation of CD73 KO mice's lack of extracellular AMP phosphatase. Such mechanisms may cause ambiguities in results of single knockouts of mutations. Future studies may focus on combinatorial effects to clearly isolate the extracellular adenosine pool's role in sleep regulation.

Chapter 4: Effects of acute microinjections of thyroid hormone derivative 3-iodothyronamine (T1AM) to the preoptic region of adult male rats on EEG-defined sleep, body temperature, and locomotor activity [125]

4.1 Abstract

Along with the proposal of thyroid hormone's role in non-genomic signaling in the 1970s came the prediction of a decarboxylated thyroid hormone derivative. Nearly thirty years later, the decarboxylated thyroid hormone derivative 3-iodothyronamine (T1AM) was discovered to be endogenous in rodent brain, and intraperitoneal injection of T1AM in mice was found to cause hypothermia and bradycardia. Meanwhile, more recent studies have showed microinjection of thyroid hormone 3,3',5-triiodothyronine (T3) to the sleep-active preoptic region decreased EET-defined sleep in adult male rats. T3 inhibits $GABA_A$ receptors in vitro. The effects of thyroid hormone application are generally opposite to those of T1AM. Injection of T1AM to the preoptic region of adult male rats increased sleep fragmentation and, contrary to prediction, caused a decrease in sleep in a biphasic fashion, similar to the effects of thyroid hormone. This result may be due to shared mechanisms or functions of sleep regulation. T1AM also decreased body temperature, an effect seen after systemic application of T1AM in past studies. This work represents the first study showing the effects of T1AM on sleep, and suggests that T3 and T1AM have shared as well as independent effects on the adult mammalian brain.

4.2 Introduction

Dysthyroid states give insight into thyroid hormones' role in the adult brain. In humans, pathological effects on sleep and behavior due to thyroid dysfunction are documented [126-129], but results of systematic studies do not agree [130-133]. Thyroid hormone (3,3',5-triiodothyronine, or T3) administration to the preoptic region of adult male rats reduces non-REM sleep according to EEG data collection methods. Demonstration of behavior after short-term, direct administration of T3 to brain tissue clarifies ambiguities in previous behavioral data.

Thyroid hormone derivates, including 3-iodothyronamine (T1AM), are present in small amounts in rodent brain extracts [134]. While T3 and thyroxine (T4) have been confirmed to localize in short-term-signaling compartments of adult mammalian neural tissue [135-139], T1AM's distribution in brain has not yet been identified. The synthesis mechanism of T1AM is also presently controversial; preliminary work speculated that T1AM resulted from aromatic amino acid decarboxylase (AADC) [134, 140-142], which also converts tyrosine and tyrosine analogues to dopamine. T3 production from T4 occurs in neural tissue [143]. Triiodothyroacetic acid (triac) and tetraiodothyroacetic acid (tetrac) have also been described as derivatives synthesized within neural tissue [144]. Iodothyronines, however, are not substrates for AADC [145], and extrathyroidal conversion of T4 to T1AM does not occur outside the thyroid gland [146].

T1AM does not bind to, or interact with, thyroid hormone nuclear receptors [134, 147], but activates Trace Amine-Associated Receptor 1 (TAAR1), an inhibitory metabotropic receptor, and binds to α2A adrenergic receptor [134, 148]. These receptors are expressed in the preoptic region [149-151], the site of study in previous investigations

establishing T3's sleep influence. As thyroid hormones are accepted as non-genomic signaling molecules [152-156] which affect sleep, T1AM may act similarly. T1AM also inhibits serotonin vesicular transporter (VMAT2) extracted from rat brain synaptosomes as well as recombinant norepinephrine (NET) and dopamine (DAT) plasma membrane transporters [157].

Behavioral changes due to T1AM are related to changes due to norepinephrine and thyroid hormones. Intraperitoneal (IP) injection of T1AM causes a sudden decrease in rat activity [134, 158], an effect opposite to that observed in chronically hyperthyroid rats [159], and decreases body temperature up to 10 °C for several hours after IP injection [134]. While T4 locally administered to hippocampal cells in anesthetized rats causes a decrease in excitability [160], T1AM administered to the locus coeruleus (LC) increases firing in neuronal populations in the area [158, 161]. Further, norepinephrine and its agonists rapidly decrease EEG-defined sleep after injection to the preoptic region [162-164], and norepinephrine injection to the lateral ventricle causes an increase in rat activity. This effect was also observed in chronically hyperthyroid rats after IP injection of T4.

Lesioning, c-Fos, and electrophysiological studies demonstrate sleep-regulatory nuclei including the median preoptic nucleus (MnPN), medial preoptic area, and ventrolateral preoptic nucleus [151, 165-169]. Noradrenergic projections from the LC to, and α2A adrenergic receptors within, the preoptic region suggest that T1AM's noradrenergic receptor-mediated effects may change behavior. While other mechanisms cannot be presently ruled out, we present data that gives credence to this hypothesis. We injected

T1AM to the preoptic region of adult male rats and observed consequent EEG-defined sleep behavior, compared to controls. We demonstrate changes in EEG power, sleep fragmentation, non-REM sleep, and wakefulness due to T1AM administration.

4.3 Materials and Methods

Animals and housing

Individually-housed adult male Sprague-Dawley rats (Hilltop Lab Animals, Scottdale, PA) were fed/watered *ad libitum*. The facility temperature was maintained at ~22.8 °C, with a 12:12 light:dark phase (lights on = 07:00). In order to acclimate to being handled, rats were handled frequently prior to the start of the experiment. All rats received ≥ 5 days post-surgical recovery. Procedures and materials were approved by the Rutgers Institutional Animal Care and Use Committee (IACUC). The housing facility is accredited by the Association for Assessment and Accreditation of Laboratory Animal Care (AAALAC).

Animal Surgery

Rats were placed in an induction chamber and anesthetized with 5% isoflurane using an EZ Anesthesia vaporizer apparatus (EZ Systems) at 2 L/min. After loss of consciousness, rats were placed in a stereotaxic device on a heating pad maintained at 37 °C and connected to a nosecone. Anesthesia was reduced to 2.5% isoflurane for maintenance of unconsciousness. Mini-Mitter transponders were inserted into the peritoneal cavity via a small ventral incision. A 2 cm incision was made to the scalp and the skull exposed. After scraping away muscle tissue and stanching residual bleeding, a stainless-steel EEG

electrode (Plastics One E363-20) was screwed into each quadrant of the skull. EMG electrodes comprised of two stripped-end Teflon-coated wires were inserted into the neck musculature. Electrode sockets were inserted into a screw-top pedestal (Plastics One MS363).

A hole, +0.5 mm medial–lateral and −0.2 mm dorsal–ventral with respect to bregma, was drilled into the skull using a 0.0125" drill bit, after which two stainless steel guide cannulae were inserted −7.1 mm dorsal/ventral with respect to the surface of the skull. Cannulae were 1 mm apart from each other. Electrodes and cannulae were secured with dental acrylic. A topical antibiotic ointment was applied to the periphery of the surgical site.

Experimental Procedure

Rats were housed in individual chambers in an electrically-isolated, sound-attenuated facility for 24 h under the same light/dark schedule prior to the experimental procedure. On the first, control day of each experiment, rats were injected with vehicle solution alone (aCSF: 0.25 mM Na2HPO4, 0.5 mM NaH2PO4, 0.4 mM MgCl2, 0.65 mM CaCl2, 3 mM KCl, 128 mM NaCl, 25 mM NaHCO2; pH =7.4, supplemented with 2% v/v DMSO). The injections took place over 2 min, with 0.25 µL injected in each cannula. On the second, experimental day of each week of the study, rats were bilaterally injected with a total of 0.3, 1, 3, or 10 µg T1AM dissolved in vehicle. All injections were made at approximately 09:00.

After injection on both control and experimental days, animals were connected to a Grass Instruments Model 15 multichannel amplifier via a shielded cable leading through a multichannel commutator (Plastics One SL6C). EEG and EMG were digitized with a CED Micro 1401 data acquisition unit. EEG recording took place for 24 h following each injection using Spike2 Software. Locomotor activity and core body temperature were measured continuously using a Mini-Mitter receiver placed under each chamber and recorded with VitalView software.

Data Analysis

Thomas D. James analyzed EEG and EMG data offline. He was made unaware of experimental conditions to avoid bias while interpreting EEG. Each 24-hour record was put through a 1 – 30 Hz band pass filter and a 20 Hz notch filter in order to minimize effects of ambient electrical signals. Records were evaluated in 30-second epochs and a state of consciousness (non-REM, REM, or Awake) was assigned according to standard criteria [170]. Temperature and activity data were acquired as the average (temperature) or sum (activity) in one-minute intervals. Data were included after cannulae placement was histologically confirmed (Figure 1) according to a rat brain atlas [171]. Although placement of cannula injection tips centered around the MnPN, injection sites are conservatively referred to as being placed in the “preoptic region”, due to the significant radius of diffusion from the cannulae [172].

Data were analyzed in 1-hour bins using a 2-way analysis of variance (ANOVA) on GraphPad Prism version 5.00 for Windows (GraphPad Software, San Diego, California,

USA, www.graphpad.com). Each 2-way ANOVA compared the effect of the vehicle injection to a dose of T3 as one factor and time after injection as a second factor. Temperature and activity data were normalized to account for placement of the Mini-Mitter in each animal. Body temperature was normalized in relation to the average maximal and minimal temperatures. Activity for each rat was normalized, with 100% corresponding to maximal observed activity and 0% corresponding to minimal observed activity for each experimental week. In cases where rats disconnected their cables, or lost their mounted headset, experimental data were compared to pooled control data.

4.4 Results

Microinjection of 3 μg T1AM to the preoptic nucleus changed low-frequency power and theta during wakefulness (Figure 2). In the first 10 hours after T1AM injection, rats exhibited significantly higher fragmentation of sleep than did rats receiving injection of vehicle solution alone (Figure 3). Bout lengths of sleep for control conditions 161.1 ± 2.8 s (mean ± SEM), while after T1AM injections, bout lengths were 143.8 ± 2.8 s. Two-tailed T-testing showed a significant difference of $P < 0.0001$ between groups ($T = 4.3$, $df = 5245$).

Non-REM sleep was reduced in a biphasic fashion after administration of T1AM (see Figure 4 and Table 1). A 2-way ANOVA indicated a statistically significant effect due to T1AM injection at doses 1 and 3 μg ($P < 0.01$, $F(1522) = 6.82$, partial $\eta^2 = 0.013$; $P < 0.01$, $F(1487) = 6.75$, partial $\eta^2 = 0.014$, respectively). However, no significant effect was noted

at 0.3 or 10 μg ($P < 0.68$, $F(1546) = 0.17$, partial $\eta^2 = 0.0003$; $P < 0.89$, $F(1498) = 0.02$, partial $\eta^2 = 3.6E\text{-}5$,

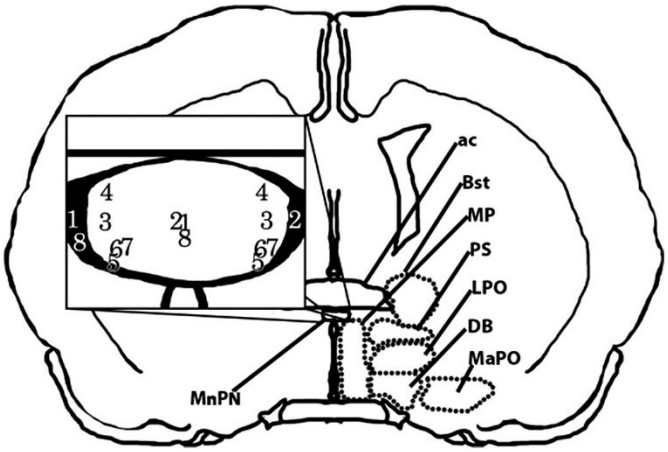

Figure 1. Histological confirmation of cannulae placement. Eight rats were histologically confirmed to have cannula tips within the preoptic region, centered within the median preoptic nucleus (MnPN). Each number denotes cannula terminae per rat. Surrounding structures' abbreviations are: ac (anterior commissure), Bst (bed nucleus of the stria terminalis), MP (medial preoptic area), PS (parastrial nucleus), LPO (lateral preoptic area), DB (diagonal band of Broca), MaPo (magnocellular preoptic nucleus).

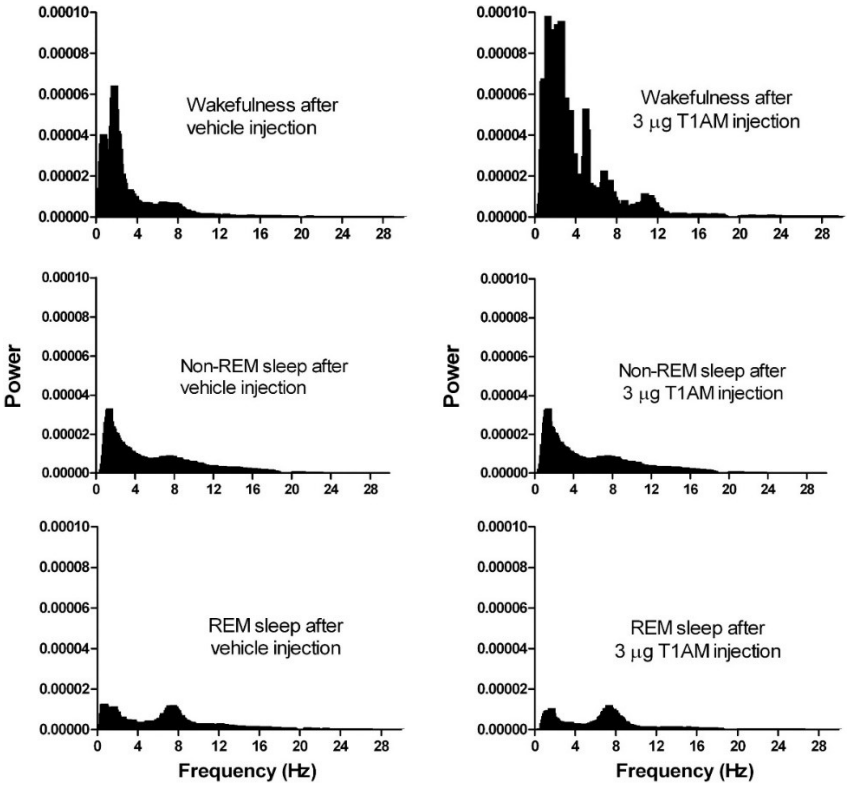

Figure 2. Power spectra of consciousness state over 4 hours after vehicle and 3 μg T1AM injection into the preoptic region. EEG signals were pre-filtered, with a notch filter at 19.5–20.5 Hz, and low-pass filter removing signal above 30 Hz.

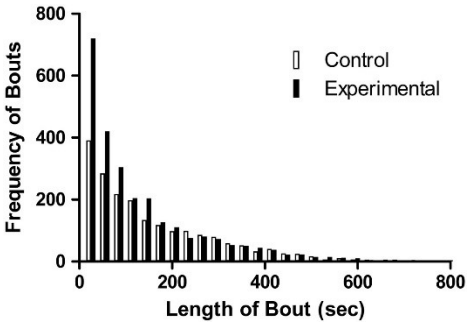

Figure 3. Sleep fragmentation after T1AM injection. Non-REM sleep bout lengths were found to be significantly longer after vehicle versus after combined T1AM treatments.

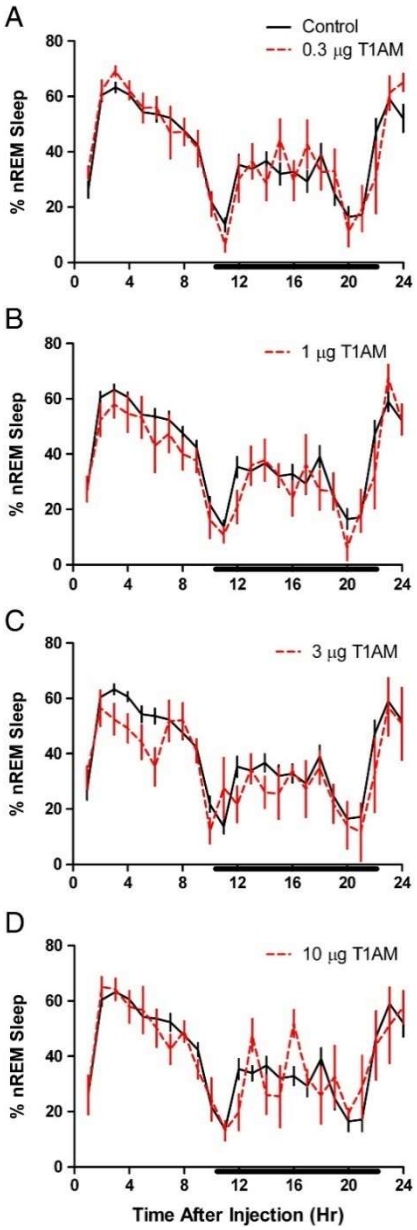

Figure 4. Non-REM sleep after T1AM injection. Percentage of mean nREM sleep after administration of vehicle (black line) or T1AM (red dashed line) to the preoptic region of adult male rats. Doses of 1 and 3 µg T1AM, panels B and C, caused statistically significant changes in nREM sleep (two-way ANOVA, n = 5, n = 4, respectively). Diurnal variation in nREM sleep was noted. However, no interaction between the effects of time and T1AM treatment were noted. Black bar on x-axis indicates dark time of day. Error bars denote standard error of the mean (SEM).

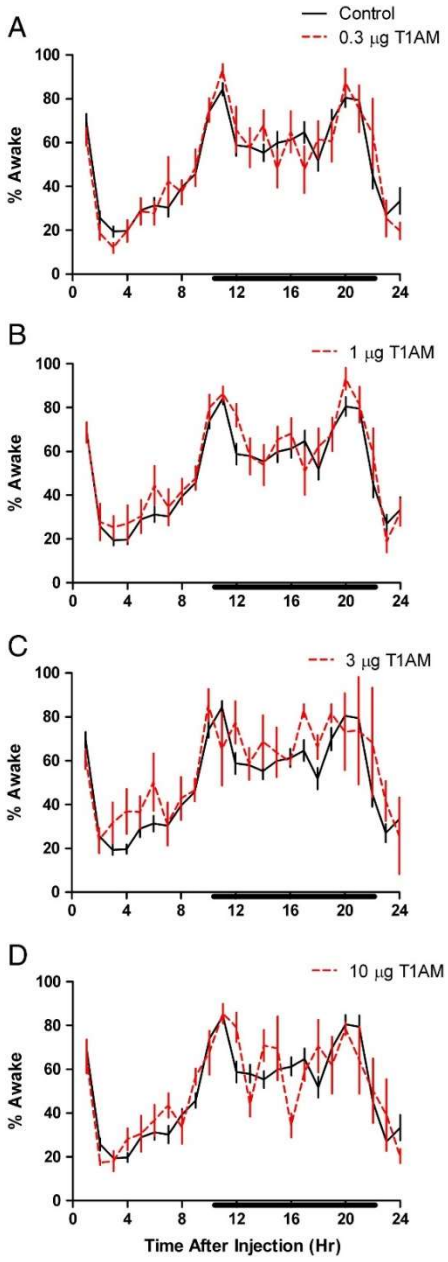

Figure 5. Wakefulness after T1AM injection. Percentage of mean wakefulness after administration of vehicle (black line) or T1AM (red dashed line) to the preoptic region of adult male rats. Doses of 1 and 3 μg T1AM, panels B and C, caused statistically significant changes in wakefulness (two-way ANOVA, n = 5, n = 4, respectively). Diurnal variation in wakefulness was noted. However, no interaction between the effects of time and T1AM treatment were noted. Black bar on x-axis indicates dark time of day. Error bars denote standard error of the mean (SEM).

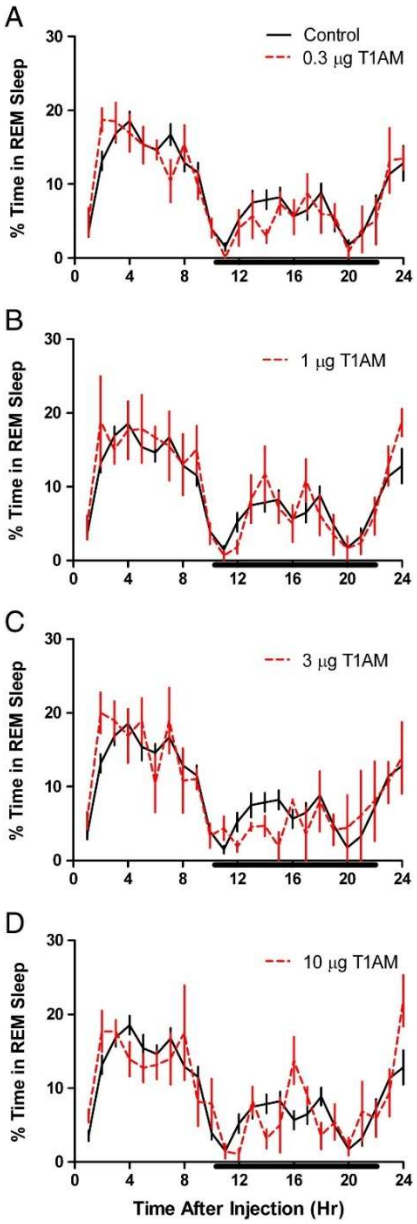

Figure 6. REM sleep after T1AM injection. Percentage of mean REM sleep after administration of vehicle (black line) or T1AM (red dashed line) to the preoptic region of adult male rats. T1AM administration did not significantly affect REM sleep. Diurnal variation in REM sleep was noted. However, no interaction between the effects of time and T1AM treatment were noted. Black bar on x-axis indicates dark time of day. Error bars denote standard error of the mean (SEM).

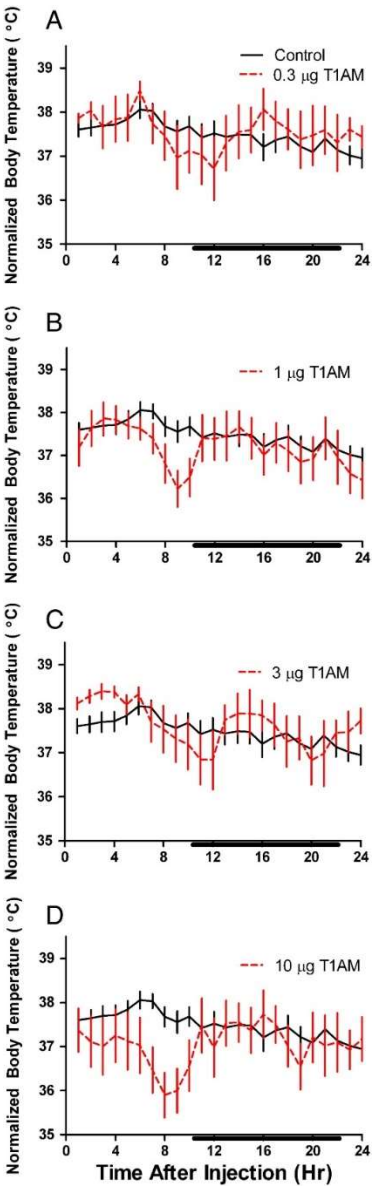

Figure 7. Body temperature after T1AM injection. Mean, normalized core body temperature after administration of vehicle (black line) or T1AM (red dashed line) to the preoptic region of adult male rats. 1 or 10 µg T1AM (B and D) administration significantly affected body temperature (two-way ANOVA, n = 6, n = 7, respectively). Diurnal variation in body temperature was only noted after doses of 1 or 3 µg T1AM (two-way ANOVA, n = 7, n = 6, respectively); no interaction between the effects of time and T1AM treatment was found. Black bar on x-axis indicates dark time of day. Error bars denote standard error of the mean (SEM).

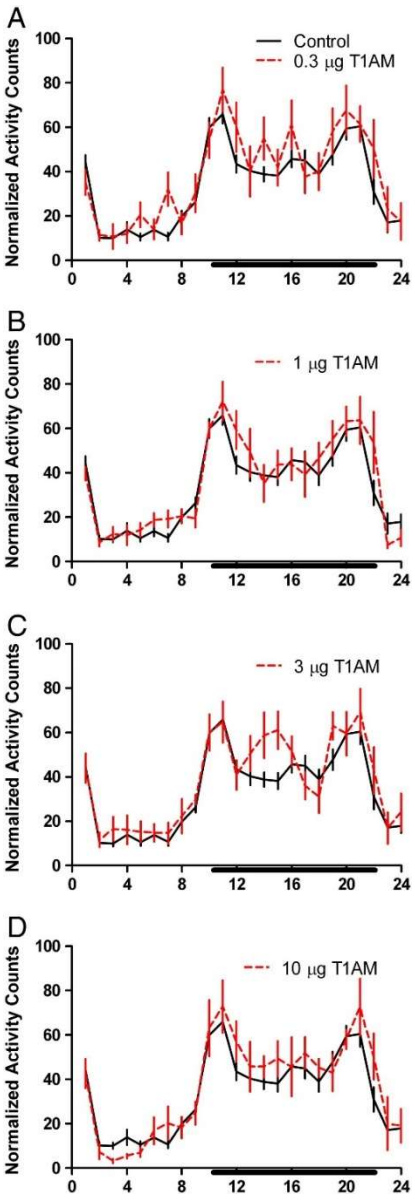

Figure 8. Activity after T1AM injection. Normalized locomotor activity after administration of vehicle (black line) or T1AM (red dashed line) to the preoptic region of adult male rats. Doses of 0.3 and 3 μg T1AM, panels A and C, caused statistically significant changes in locomotor activity (two-way ANOVA, n = 7 for both). Diurnal variation in activity was noted. However, no interaction between the effects of time and T1AM treatment were noted. Black bar on x-axis indicates dark time of day. Error bars denote standard error of the mean (SEM).

	Control	0.3 mg T1AM	1 mg T1AM	3 mg T1AM	10 mg T1AM
Waking					
Time (minutes)	230.58	223.62	256.5*	267.48*	238.8
Standard error	3.6666	3.825	3.5058	3.3966	3.4626
non-REM					
Time (minutes)	289.62	296.76	257.7*	255.66*	282.66
Standard error	2.7042	2.808	2.5152	2.5488	2.7972
REM					
Time (minutes)	76.38	77.28	82.62	80.88	77.4
Standard error	0.981	1.0104	1.0218	1.1562	0.8034

Table 1. Total time in each vigilance state during first 10 hours following T1AM injection. Asterisks denote significance.

respectively). The decrease in sleep was most apparent within the first 8 hours after injection (Figure 4B, Figure 4C). However, there was no significant interaction between time and injection T1AM, and Bonferroni's post-hoc test showed. Significant diurnal variation was observed in nREM sleep for all dosages 0.3, 1, 3, and 10 μg T1AM ($P < 0.01$ and partial $\eta^2 = 0.47$, partial $\eta^2 = 0.43$, partial $\eta^2 = 0.36$, partial $\eta^2 = 0.39$, respectively).

T1AM also affected wakefulness. A significant increase in wakefulness, complementing the decrease in non-REM sleep, was seen after injection of 1 and 3 μg of T1AM (Figure 5; $P < 0.04$, $F(1546) = 4.41$, partial $\eta^2 = 0.008$; $P < 0.02$, $F(1463) = 5.47$, partial $\eta^2 = 0.01$, respectively), but not at 0.3 or 10 μg T1AM ($P < 0.96$, $F(1546) = 0.00$, partial $\eta^2 = 3.6E\text{-}5$; $P < 0.81$, $F(1498) = 0.06$, partial $\eta^2 = 0.0001$, respectively). This change in wakefulness

was strongest for the first 8 hours post-injection (Figs. 5B, C). As with non-REM sleep, there was significant diurnal variation in wakefulness for all groups for all dosages 0.3, 1, 3, and 10 μg T1AM ($P < 0.01$ and partial $\eta^2 = 0.5$, partial $\eta^2 = 0.5$, partial $\eta^2 = 0.34$, partial $\eta^2 = 0.43$, respectively), but there was no significant interaction between T1AM injection and time, with Bonferroni's posthoc test showing no significant differences, either.

REM sleep features did not change after injection of T1AM (Figure 6). REM sleep varied diurnally ($P < 0.01$ and partial $\eta^2 = 0.04$, partial $\eta^2 = 0.39$, partial $\eta^2 = 0.35$, partial $\eta^2 = 0.34$) for all dosages, 0.3, 1, 3, and 10 μg T1AM, respectively. There was, however, no statistically-significant interaction between the effect of injection of T1AM and time of day. Bonferroni post-hoc tests on the data did not show any significant differences at any single time point.

T1AM significantly changed normalized body temperature after 1 or 10 μg injections (Figure 7B, Figure 7D) ($P < 0.01$, $F(1720) = 7.92$, partial $\eta^2 = 0.002$; $P < 0.01$, $F(1696) = 15.49$, partial $\eta^2 = 0.022$, respectively). The most prominent effect on body temperature occurred 8 hours after the 10 μg injection. However, it was not quite statistically significant (Figure 7D). There was a significant body temperature change over time after injection of 1 or 3 μg T1AM ($P < 0.03$, $F(23,720) = 1.67$, partial $\eta^2 = 0.05$; $P < 0.04$, $F(23, 696) = 1.60$, partial $\eta^2 = 0.05$, respectively), but there was not a statistically-significant interaction between the effects of injection of T1AM and time of day.

Doses of 0.3 and 3 μg T1AM increased normalized locomotor activity (Figure 8) ($P < 0.01$, $F(1743) = 8.18$, ; $P < 0.01$, $F(1743) = 6.98$, partial $\eta^2 = 0.003$). There was a non-

significant trend to a locomotor activity reduction in the first 5 hours after injection of 10 μg T1AM ($P < 0.08$, $F(1719) = 3.10$, partial $\eta^2 = 0.004$). There was a statistically significant diurnal variation in activity was noted ($P < 0.01$ and partial $\eta^2 = 0.38$, partial $\eta^2 = 0.41$, partial $\eta^2 = 0.39$, partial $\eta^2 = 0.39$) for all animals and T1AM dosages, 0.3, 1, 3, and 10 μg, respectively. However, there was not a significant interaction between injection of T1AM and time.

4.5 Discussion

Whereas in previous investigations, thyroid hormone injection causes increases in body temperature, heart rate, and locomotor activity, single-dose T1AM administration has a generally opposite effect [134]. Based on previous data demonstrating that T3 thyroid hormone injection to the preoptic region decreases sleep in adult male rats [173, 174], we predicted that T1AM injection to the same brain area would increase sleep relative to controls. It should be noted that according to histological confirmations of cannulae placement, and diffusion radii of microinjection volumes, T1AM spread was not limited to the target of specific injection, the MnPN. While T1AM concentration would be highest in the MnPN, the effects seen may have been partially influenced by diffusion of T1AM to sites peripheral to the MnPN. Therefore, we describe our injection target as the more general preoptic region.

T1AM, against predictions, caused a decrease in EEG-defined sleep after injection to the preoptic region. The effect was biphasic; there was no observable reduction in sleep after the lowest (0.3 μg) nor the highest (10 μg) T1AM dose, yet the middle doses (1 μg

and 3 μg) decreased non-REM sleep and increased wakefulness. This is also the same significant dosage level seen in previous studies on T3 [173, 174], and similar effects are demonstrated in studies of T3's effects on protein phosphorylation in neurons [155, 156]. However, it should be noted that the parallel effects seen between the two compounds does not indicate that T1AM is a derivative of T3. The production of T3 from T4 occurs outside the thyroid, while T1AM synthesis has not been shown to occur anywhere but within the thyroid gland [146]. T3 is not converted to T1AM, so the similarities in effective concentrations of both T3 and T1AM must therefore be due to possessing shared targets and/or functional actions that result in sleep behavior influences.

T1AM increases activity after 0.3 and 3 μg microinjection doses to the preoptic region of rats, the opposite of the effect caused by IP injection of 50 mg/kg T1AM to mice [134, 158]. Further, IP injection of T4 causing chronic hyperthyroidism in mice, as well as T3 or norepinephrine microinjection to the preoptic region, increased activity [159]. This may be due to T1AM's different activity in different regions of the CNS, and further studies may show differential effects of T1AM microinjection to different brain regions. IP injections may result in increases in T1AM concentrations in different neuronal populations than the preoptic region and account for the different results than those seen here. Dosage may also contribute to the difference in effect, and the high concentration of past IP injections may reflect the "inverted U" dose-response curve observable after injection of amphetamine [175].

The high concentration of previous IP injection-based study compared to the current work may also explain the difference in effect on body temperature between the two studies. Scanlan et al.'s IP-injected mice showed a more dramatic decrease in body temperature than did rats after microinjection to the preoptic region here. Norepinephrine also decreases body temperature after injection to the preoptic region, and this effect may be through mediation of α2 adrenergic receptors [176]. As T1AM may have noradrenergic-like mechanistic effects [148], T1AM effects on the noradrenergic systems of the preoptic region may explain the decrease in body temperature after injection there. In mice, knockout of TAAR1 causes hypothermia after IP injection of T1AM in addition to other TAAR1 agonists. TAAR1, therefore, must not be involved in the mechanism of temperature reduction after T1AM injection to the preoptic region [177].

Sleep behavior has a relationship with thermoregulatory functions, and the preoptic region has thermoregulatory functions in addition to its sleep-active neurons [178]. The preoptic region may have a role in physiological behaviors such as shivering, vasodilation after local temperature changes, the administration of glutamate, or electrical stimulation [179, 180]. Locally warming the preoptic the preoptic region induces sleep in cats [181]. The activity of sleep-active c-Fos immunoreactive neurons in the MnPN increases correlative with elevated ambient temperatures as well [165], and neuronal firing rates within MnPN change according to ambient temperature [182]. While no change was seen in non-REM sleep behavior after 10 μg T1AM, this dose showed the highest difference in post-injection body temperature, relative to controls.

This indicates that changes in thermal and sleep regulation may not be completely associated with one another. Other studies demonstrate dissociate changes in firing rates of sleep active neurons in the presence of different temperatures, and triazolam has been shown to increase sleep without changing body temperature [169, 183, 184]. Preoptic region mechanisms for changing body temperature do not necessarily imply a concurrent change in sleep behavior.

A proposed association between thyroid hormones and the noradrenergic systems is not new, and early descriptions of such an associated asserted the possible existence of a decarboxylated thyroid hormone derivative [141]. More recently, T1AM, a decarboxylated derivate was found in rodent brain extracts [134], and it activates α2A adrenergic receptors [148]. The answer to whether T1AM interacts, as thyroid hormones do, with $GABA_A$ receptors, or with any of its other non-genomic modes of action.

The preoptic region has been demonstrated to affect several aspects of thermoregulation and sleep behavior, and the anatomical and functional pathways of the region may act independently or interactively. Our results show that EEG-defined sleep can be modulated by T1AM injection to the preoptic region, and it reiterates the lack of obligatory associations between temperature and sleep regulatory changes.

Chapter 5: Dynamics of High-Frequency Brain Activity [185]

5.1 Abstract

Evidence suggests that electroencephalographic (EEG) activity extends far beyond the traditional frequency range. Much of the prior study of >120 Hz EEG is in epileptic brains. In the current work, we measured EEG activity in the range of 200 to 2000 Hz, in the brains of healthy, spontaneously behaving rats. Both arrhythmic (1/f-type) and rhythmic (band) activities were identified and their properties shown to depend on EEG-defined stage of sleep/wakefulness. The inverse power law exponent of 1/f-type noise is shown to decrease from 3.08 in REM and 2.58 in NonREM to a value of 1.99 in the Waking state. Such a trend represents a transition from long- to short-term memory processes when examined in terms of the corresponding Hurst index. In addition, treating the 1/f-type activity as baseline noise reveals the presence of two, newly identified, high frequency EEG bands. The first band (ψ) is centered between 260–280 Hz; the second, and stronger, band is a broad peak in the 400–500 Hz range (termed ω). Both of these peaks display lognormal distributions. The functional significance of these frequency bands is supported by the variation in the strength of the peaks with EEG-defined sleep/wakefulness.

5.2 Introduction

Global brain activity is conventionally measured in the electroencephalogram, which is comprised of oscillations in several functionally-relevant frequency bands. Historically, the bands were identified as δ (1–4 Hz), θ (4–7 Hz), α/μ (8–13 Hz), β (beta, 15–30 Hz), γ

(gamma, 30–80 Hz) and high γ (80–150 Hz) waves [186, 187]. In addition, “ripples” can be demonstrated as brief bouts of 80–200 Hz oscillations. “Fast ripples” are 250–600 Hz oscillations which occur in epileptogenic brain near the site of a lesion [187, 188]. In sensory evoked potentials, oscillations are known to occur in the 200–400 Hz and higher ranges in rats [189] and humans [188]. EEG in the range ≥200 Hz has been elicited by high-frequency stimulation of the thalamus in healthy rats [190]. However, non-pathological spontaneously-occurring EEG (i.e., not stimulus-evoked) over 200 Hz has not previously been reported [191]. Furthermore, the functions of high frequency EEG are not fully elucidated. The current study is inspired by a recently published theoretical model which proposed a role for high frequency brain activity as a critical factor for signal transmission in the brain [192].

In addition to rhythmic EEG activity in the 200–1000 Hz range, 1/f-type noise is expected across the full range of brain activity examined. Here, the term “1/f-type” is used to indicate an inverse power law dependence ($1/f^{\beta}$) that quite often displays behavior better described by an exponent (β) other than 1. The presence of 1/f-type noise in the conventional EEG spectral range (i.e. 1–100 Hz) has been noted several times over the past forty years [193-198] and its presence in the higher frequency range would come as no surprise given its ubiquitous nature. The manifestation of 1/f-type behavior in the electrical activity of the brain has often been related in some part to ion channel activity fluctuations [199, 200]. A recent study by Pettersen et al. [201], suggests that power spectral densities (PSD) of such noise exhibit two different exponential dependencies and as such two different possible contributors. At lower frequencies, they argue that

synaptic noise is the dominant contributor and at higher frequencies intrinsic channel noise dictates the value of the exponent. Other examples of such inverse power law dependency have been noted by Linkerkaer-Hansen et al. [202], in the decay of μ and β amplitude fluctuations. It is important to remember that EEG is a macroscopic electrophysiological measurement that reflects summation of synchronized potentials within the cerebral cortex and therefore is insensitive to single channel fluctuations.

5.3 Materials and Methods

Measurement of EEG-defined sleep and waking

All animal use was approved by the Rutgers University Institutional Animal Care and Use Committee. The care and use of the animals was according to the stipulations of this committee. Adult male Sprague-Dawley rats (Hilltop Lab Animals, Scottdale, PA) were housed individually, given food and water ad libitum and handled frequently to reduce the effects of stress. The temperature of the facility was maintained at 22.2–23.3 °C on a 12 hour light/12 hour dark cycle (lights on at 07:00). Rats were anesthetized with isoflurane using an EZ Anesthesia vaporizer apparatus. Next, an incision was made in the scalp, the skull exposed, and a screw EEG electrode (Plastics One E363-20) inserted in each quadrant of the skull. Two Teflon-coated wires with stripped ends were inserted into the neck musculature to serve as EMG electrodes. The electrode sockets were inserted into an electrode pedestal (Plastics One MS363), then secured with dental acrylic.

After a recovery period of a week, animals were placed in an individual chamber within a shielded room and connected to a multichannel amplifier (Grass Instruments Model 15) via a shielded cable leading through a multichannel commutator (Plastics One SL6C). At this point, one of the channels was connected to the Hewlett-Packard model 3562 A signal analyzer for recording of brain activity of up to 1 kHz. In parallel, EEG and EMG were digitized using a data acquisition unit (CED Micro 1401) and recorded for 48 hours using Spike2 Software.

EEG and EMG data were analyzed offline by a trained researcher. Each record was evaluated in 30-second epochs, and a state of arousal (NonREM, REM, or Waking) assigned according to standard criteria [170]. High-frequency brain activity was recorded as described below.

Measurement of high-frequency brain activity

The use of cranial implanted electrodes improves signal strength and reduces low-pass filtering effects that would otherwise hinder detection of high frequency neural oscillations. A single channel from the commutator was sent to a coaxial BNC breakout box, built to accept the 6-pin connector terminating the Plastics One electrode cable bundle, thereby facilitating individual electrode pair selection. In this study, measurements were conducted between the left frontal and left occipital electrodes.

Neural activity sensed by the electrodes was sent from the breakout box to a custom-built preamplifier stage. The preamplifier was built around a Linear Technologies LTC1051 zero-drift operational amplifier. The LTC1051 displays excellent DC and AC

characteristics over the frequency range of interest (1 Hz–10 kHz) and utilizes chopper-stabilization in conjunction with internal capacitors to achieve low output noise (1.5μVP−P). To further curtail instrumentation noise, the circuitry was powered by two 9 V batteries which fed a Texas Instruments TLE2426 rail splitter. The function of the rail splitter is to produce precise virtual ground positioned at one-half that of the single-supply battery source. Metal film resistors were used to minimize circuit 1/f noise; while, EMF noise was suppressed by housing the circuitry housed in a grounded aluminum cast case. Input and output connections were made using floating-shield coaxial BNC feedthroughs. The preamplifier was set to a nominal gain of 100x in order to circumvent saturation from lower frequency brain electrical activity (e.g., α rhythms) which can be a couple of orders of magnitude larger than the high-frequency brain activity. After amplification, the signal was ultimately sampled by a fast Fourier transform (FFT) based dynamic signal analyzer (Hewlett-Packard model 3562 A). A frequency range starting at 50 Hz and spanning two decades was chosen along with log resolution to minimize acquisition time and optimize data collection in the region of interest.

1/f noise subtraction and log-normal fits

In order to decouple high frequency EEG activity from the 1/f-type noise, in this case acting as a baseline, the low (<100 Hz) and high (>1000 Hz) regions of the PSD spectra were isolated and fit using regression analysis to a power law, see Figure 1. This defines a baseline that was subtracted from the PSD spectra in order to resolve the presence of RRF activity. As also seen in Figure 1, the subsequent spectra are bimodal in nature and

display a log-normal distribution. Each mode (band) was deconvolved via spectral fitting to a log-normal distribution to determine their relative strengthens, bandwidths, and dependences on waking state, Figure 1. As reviewed by Buzsaki, and Mizuseki [12], the presence of skewed distributions with heavy-tails, such as a lognormal, are quite common in synaptic firing rates and neurological activity in general since such systems are often multiplicative in nature. Due to the lower occurrence of REM events over the collection period than wake and/or NonREM states, the data set for high-frequency brain activity activity during REM displays increased statistical noise.

5.4 Results

As shown in Figure 1, brain EEG activity is apparent in the 200–1000 Hz PSD range. After correcting for 1/f-type noise (Figure 1A–C), two regions of high-frequency EEG were visible (Figure 1D–F) and display lognormal spectral distributions. The first distribution, which we have termed ψ, displayed a peak in the range of 285–315 Hz and the second distribution, termed ω, occurred in the 385–485 Hz range. The peaks varied with the EEG-defined stage of sleep/wakefulnesss, having much greater peak areas in Waking (Figure 1D) than in NonREM (Figure 1E) or REM (Figure 1F) sleep. These will be referred as the ψ-band and ω-band, respectively. As noted in Table 1, the peak spectral location of the bands, during both waking and NonREM states, remain relatively unaltered; while, during REM their frequencies display increases by 4.9% and 21% with respect to waking. Upon waking from NonREM, both bands show a marked (~3-fold) increase in net strength.

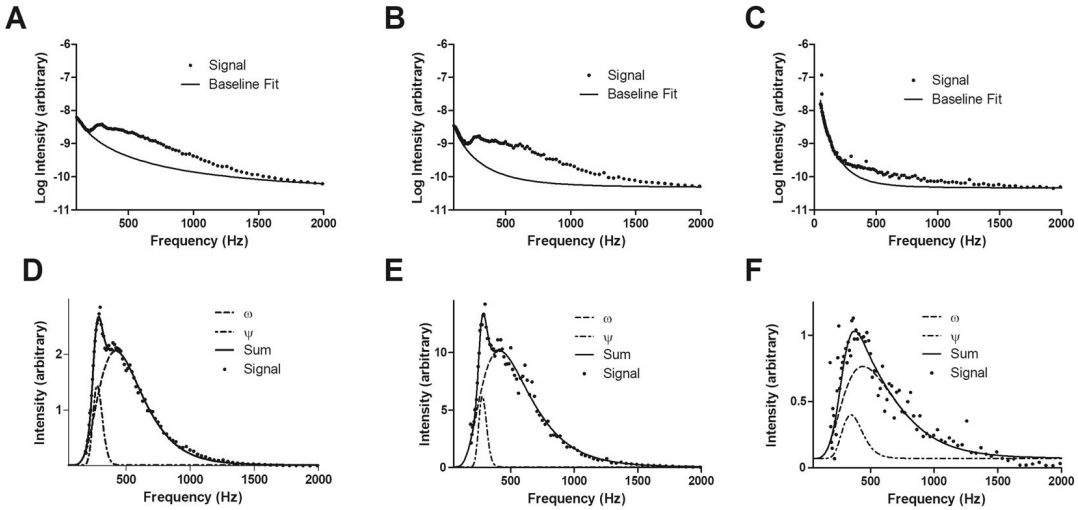

Figure 1. Summation of high-frequency brain activity signal data in different EEG states and characterization of ψ and ω frequency bands. Panels A–C show the overall high-frequency brain activity signal data (dots) from 100–2000 Hz as well as the 1/f-type baseline (solid). Each spectrum is an averaged Fourier analysis of high-frequency signal (1–2000 Hz) during EEG-defined intervals of waking (A), NonREM sleep (B), and REM sleep (C). Panels D–F show the signal (dots), along with curve-fitted sum (solid), as well as the peaks corresponding to the ψ band (lower trace) and the ω band (upper trace) during periods of waking (D), NonREM sleep (E), and REM sleep (F). The data are averages of results from 3 rats.

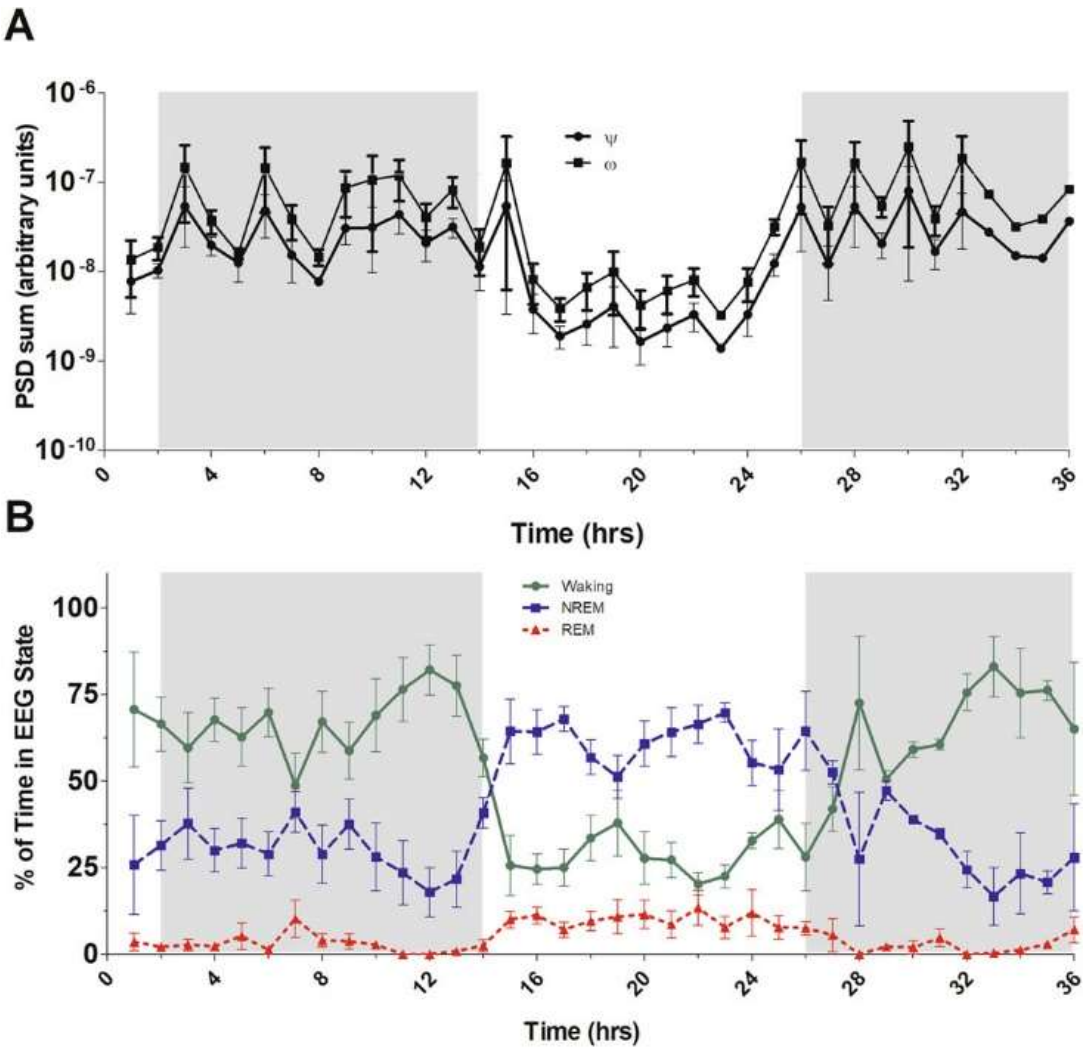

Figure 2. Power spectrum density of ψ and ω and percentage of mean wakefulness, NonREM sleep, and REM sleep for each one-hour period over 36 hours. The power spectrum density sum was calculated for each hour over 36 hours. Panel (A) represents the ψ frequency band (285–315 Hz, squares) and the ω frequency band (385–585 Hz, filled circles). Panel (B) shows the percentage of mean wakefulness (solid with filled circles), NonREM sleep (dashes with squares), and REM sleep (dots with triangles) over 36 hours. The shaded area denotes the 12-hour dark phase of the light-dark cycle. The data are average results from three rats and the error bars indicate standard errors of the mean.

EEG State	Peak Frequency (Hz[A])	Median Frequency (Hz)	S.D.[B] (Hz)	Strength (arbitrary[C]) × 10^{-8}	H
Waking – ψ Band[D]	288	291	11.5	7.6	0.49
Waking – ω Band[E]	389	478	14.2	155	
NonREM – ψ Band	287	290	8.89	3.1	0.79
NonREM – ω Band	416	509	10.5	47	
REM – ψ Band	302	314	51.5	7.46	1.04
REM – ω Band	471	583	29.3	0.957	

[A]Values are determined as the mean data from three rats.

[B]S.D. is the standard deviation of the median frequency. [C]The strength is represented by the area under curve. [D]The ψ band is defined by the frequency range 200–350 Hz. [E]The ω band is represented by the frequency range 375–1000 Hz.

Table 1.

A one-way ANOVA showed that the strength of the ω band was significantly influenced by the EEG state ($F = 16.18$; $P = 0.0121$) and Bonferroni's post hoc tests indicated that the strength of the band was significantly different at the $P < 0.05$ level between Wake and NonREM and between Wake and REM. The ANOVA for the effect of EEG state on the strength of the ψ band showed a trend toward significance ($F = 4.58$; $P = 0.092$). The one-way ANOVA of the median peak frequency of the ω band showed a significant effect of EEG-defined state ($F = 16.04$; $P = 0.0123$) and post-hoc Bonferroni's multiple comparison tests indicated a significant shift in frequency between Wake and REM

states ($P < 0.05$). The median peak frequency of the ψ band was not significantly influenced by EEG-defined state ($F = 0.4768$; $P = 0.652$).

EEG-defined Waking is higher in the dark phase of the light-dark cycle (Figure 2; lower panel) while REM and NonREM sleep are higher in the light phase (Figure 2, lower panel) of this nocturnal animal. The power spectrum density of both ψ and ω were lower in the light phase of the light-dark cycle (Figure 2; upper panel).

5.5 Discussion

As reviewed by Buzsáki and Mizuseki [203], the presence of skewed distributions with heavy-tails, such as a lognormal, are quite common in synaptic firing rates and brain activity in general since such systems are often multiplicative in nature. Through the use of high-frequency data collection in conjunction with conventional EEG collection in adult male rats, we demonstrate the existence of novel, bimodal brain oscillations centered at the ~280 Hz (ψ) and 400–500 Hz (ω) frequency ranges. These oscillations are present after the removal of 1/f-type noise, and show differing characteristics in different EEG-defined states. The general PSD sum also showed a consistently higher average value during the active period of the rats. The values of the PSD sum in ψ and ω bands increased during periods of wakefulness. The PSD sum changes along with the shifts in the most prominent state of EEG (Wakefulness, REM or NonREM) over time, indicating a diurnal cycle, presumably tied to the light-dark cycle.

The 1/f-type baseline exponent decreases from 3.08 − 2.58 − 1.99 for REM, NonREM, and Waking respectively. Large values for exponents approaching 3 are consistent with

the literature for EEG9. In terms of fractal dimensional analysis, it is common to describe the exponent in terms of the Hurst index (H) which is defined as $H = |\beta - 1|/2$. The H parameter is used as a means of gauging the degree of dependence of stochastically-related events. A Hurst index of $H \in (0.5,1)$ represents long-range stochastically dependent increments, a $H = 0.5$ has stochastically independent increments and a $H \in (0,0.5)$ signifies short-range stochastically dependent increments [204, 205]. While the influence of waking state on the Hurst index of high frequency EEG activity is not the premise of the current study it is nevertheless interesting to note that the H seems to decrease with increasing wakefulness implying that the underlying processes become less reliant on past events. A lower Hurst index shown during Waking (0.49) than during NonREM sleep (0.79) or REM sleep (1.04) may indicate a difference in the stochastic interdependence during those discrete EEG-defined states. The Hurst index for Waking indicates a short-range stochastically dependent increment (nearly stochastically independent), while the REM and NonREM Hurst indices indicate long-range stochastically dependent increments.

Our finding of new bands of high-frequency activity in the EEG of healthy, spontaneously behaving rats provides additional details in the picture of the types of possible brain oscillations. The two bands, termed ψ and ω, vary in strength with the state of EEG (Wakefulness, REM Sleep or NonREM Sleep), suggesting new correlates of wakefulness that might have practical utility in clinical studies. The presence of 1/f-type noise in the high-frequency recording echoes the findings of 1/f-type noise in the lower frequency EEG, emphasizing the ubiquity of this phenomenon in brain activity. The

finding of new frequency bands will open new areas of investigation of the functionality of high frequency EEG.

Chapter 6: 3,3',5-Triiodothyronine and pregnenolone sulfate inhibit *Torpedo* nicotinic acetylcholine receptors

6.1 Abstract

The nicotinic acetylcholine receptor (nAChR) is a pentameric ligand-gated ion channel (pLGIC), similar to another pLGIC, the γ-aminobutyric acid ($GABA_A$) receptor. Recent evidence implicating 3,3',5-triiodothyronine (T3) as a competitive inhibitor of the $GABA_A$ receptor-activating neurosteroid allopregnanolone suggested that T3 might also affect nAChRs. Here we show that T3 inhibits nAChRs. We also show that, unlike its effect on $GABA_A$ receptors, allopregnanolone also inhibits nAChRs, and that a closely-related molecule, pregnenolone sulfate (PS), inhibits nAChRs as well. These effects contradict the general trend of ligands having opposite effects on $GABA_A$ receptors and nAChRs, and show that some residues presumed to be active in ligand binding are not necessary. Further, we demonstrate that at pHs wherein the T3 molecule is neutral, T3 retains its inhibitory effects on nAChRs. Finally, we show that both T3 and PS affect nAChR channel desensitization, which may implicate a binding site that was recently theorized to be responsible for PS desensitization of the GABAA receptor.

6.2 Introduction

The nicotinic acetylcholine receptor (nAChR) is an excitatory receptor protein localized in the central nervous system [206] and at the neuromuscular junction (reviewed in [207]). Pathologies of the receptor, including epilepsy [208] and myasthenia gravis (in muscle-type nAChRs) [209, 210], demonstrate its crucial function in fast synaptic

transmission. It is a cation-translocating member of the pentameric ligand-gated ion channel (pLGIC), or “Cys-loop” receptor superfamily [211]. Of the five homologous subunits that comprise the nAChR structure and central pore, two are identical (α, γ, α, β, δ). When acetylcholine molecules bind to the α-γ and α -δ subunit interfaces in the receptor’s extracellular domain (ECD), conformational changes propagate to its transmembrane domain (TMD). Four alpha helices (M1-M4) from each subunit form the TMD, with the M2 helices from each subunit lining the receptor’s central pore. Upon binding acetylcholine, the central pore’s inner diameter increases, permitting ion flux through the channel [212].

The Cys-loop superfamily also includes glycine receptors, 5-HT3 receptors, and γ-aminobutyric acid ($GABA_A$ and $GABA_C$) receptors [211]. Neurosteroids, either those synthesized in endocrine glands and metabolized, or those synthesized *de novo* in brain tissue, can have sedative, anxiolytic, anti-convulsant, and analgesic effects on behavior. Previous investigations of cys-loop receptors elucidate structure-function relationships of neurosteroids’ molecular features. Distinction between molecular features of otherwise similar compounds give insight into binding sites on the receptor of binding orientation of this class of ligands; closely-related molecular species can have differing [213] or opposing [214] effects on their target receptor.

The neurosteroid 3α-hydroxy-5α-pregnan-20-one (allopregnanolone) activates the $GABA_A$ receptor [215], as does the related 5α-pregnane-3α,21-diol-20-one (THDOC) [216-218]. However, pregnenolone sulfate (PS), a sulfated neurosteroid similar to allopregnanolone, inhibits $GABA_A$ receptor function. Meanwhile, the thyroid hormone

3,3',5-L-triiodothyronine (T3) (Figure 1), theorized to have neurosteroid-like effects due to its similarity to neurosteroids' molecular dimensions [219] and functional groups, also inhibits activity of the $GABA_A$ receptor at low concentrations [152, 154, 215]. T3 competitively inhibits activation due to allopregnanolone, which indicates a shared binding site [215]. The differential effects of highly similar neurosteroids, and the similar effects of less closely-related molecules, make generalized geometric and charge-based analogy to ligand function difficult.

Allopregnanolone's activation of $GABA_A$ receptors requires the $GABA_AR$ α_1 and β_2 subunit M1 alpha helices [220-222]. Recently, a crystal structure of a homopentameric receptor chimera with a *Gleobacter* ligand-gated ion channel (GLIC) ECD and a mouse $GABA_AR$ α_1 subunit showed that PS binds alongside a groove between the M3 and M4 domains near the intracellular side of the transmembrane domain of $GABA_A$ receptors [223]. This site is involved with the recently classified "desensitization gate" involving the M1-M2 linker and M3 helix of $GABA_A$ receptors, where residues interact after agonist binding to take a desensitized conformation [224]. The TMD of nAChRs is similar to the mouse $GABA_AR$ α_1 subunit TMD (17% identity; 33% similarity). It is therefore possible that PS and T3 bind to the TMD of nAChRs and could modulate nAChR activity.

While cholesterol in the surrounding lipid environment was found to be necessary for nAChR ion conductance in a dose-dependent fashion [225, 226], most studied neurosteroids inhibit nAChRs. Progesterone, dehydroepiandrosterone sulfate (DHEAS),

hydrocortisone, and 3α,5α,17β-3-hydroxyandrostane-17-carbonitrile (ACN), inhibit rat neuronal nAChRs [213, 227], while progesterone, estradiol, corticosterone, and dexamethasone non-competitively inhibit human muscle-type [228, 229] and ganglionic nAChRs [228].

Changes in extracellular pH also affect nAChR ion conductance, with more acidic environments yielding lower ion flux and basic environments yielding higher ion flux with respect to the receptor's acetylcholine response at a neutral pH [230, 231]. Different pH environments also affect mean open channel time and desensitization of the receptor [231]. Previous publications suggest that charged residues in the nAChR vestibular and channel pore region affect allosteric transitions to active and inactive states, and that changes in the extracellular pH would titrate these residues [230, 231]. Charged positive and negative residues of interest in proximity to one another may mutually repel at extreme pHs, changing the conformation of the receptor and its channel state transition kinetics, compared to those at a neutral pH.

Ligand effects on nAChRs and $GABA_A$ receptors are often opposite: nonhalogenated and halogenated alkane anesthetics inhibit nAChRs but potentiate $GABA_A$ receptors (for review see [232]). We sought to characterize the nature of two putative GABA-negative ligands, T3 and PS. We extracted functional nAChRs from *Torpedo californica* and used two-electrode voltage clamp (TEVC) to demonstrate functional effects of PS and T3 on nAChRs. We found that both PS and T3 inhibit nAChR activity due to acetylcholine, representing a case in which the same effect on channel function is demonstrated in both nAChRs and $GABA_A$ receptors. We also performed TEVC in differing extracellular pH

environments to demonstrate the differential effects pH has on ligand charge and resultant receptor activity. Further, we show that PS and T3 modulate the effects of different pH environments on current amplitude when binding acetylcholine. We also show that T3 and PS change nAChR kinetics, increasing desensitization rate at low pHs but minimally affecting desensitization rate at high pH.

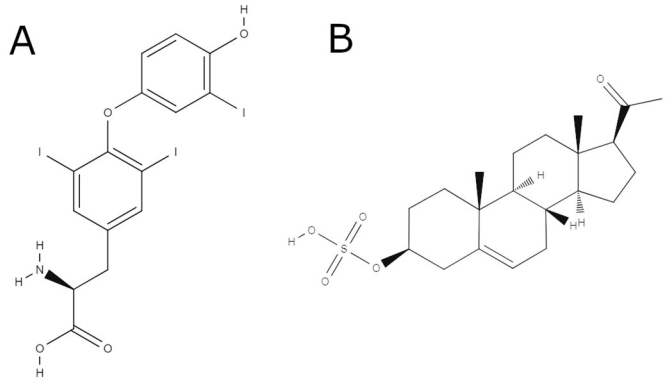

Figure 1. Molecular structure of 3,3',5-triiodothyronine (T3) and pregnenolone sulfate (PS). Comparisons of structures of the thyroid hormone T3 (A) and the neurosteroid pregnenolone sulfate (B). T3 and neurosteroids share common features including molecular volume and size, placement of hydrogen-bond accepting groups, presence of residues projecting from rings, and charged headgroups.

6.3 Materials and Methods

Frozen Torpedo *electric organ tissue and* Xenopus *oocytes*

Flash-frozen *Torpedo* electric organ was purchased from Aquatic Research Consultants (San Pedro, CA). Ready-to-inject, defolliculated *Xenopus* oocytes were purchased from Ecocyte Bioscience (Austin, TX).

Chemicals

Carbachol, acetylcholine, DMSO, asolectin, T3, NaOH, allopregnanolone, and pregnenolone sulfate were purchased from Sigma Aldrich (St. Louis, MO). Isoflurane was purchased from Henry Schein Animal Health (Dublin, OH). T3 was dissolved in 0.1 M NaOH. Allopregnanolone was dissolved in 0.1 % DMSO. All other ligands were dissolved directly in modified Barth's solution (88mM NaCl; 1mM KCl; 0.4mM CaCl2; 0.33mM Ca(NO3)2; 0.8mM MgSO4; 5mM Tris-HCl; 2.4mM NaHCO3; Tris was replaced with either MES or HEPES at other pHs).

Preparation of crude Torpedo nicotinic acetylcholine receptors

All steps before microinjection of resuspended receptor proteins were performed at 0 to 4 °C and were modified from the preparation method described in Ochoa, Dalziel, and McNamee, 1983. Briefly, the frozen electric organ tissue (600 g) was homogenized in homogenization buffer (10 mM sodium phosphate, 5 mM EDTA, 5 mM EGTA, 10 mM iodoacetamide, 0.1 mM PMSF, 0.02% NaN_3, pH 7.5) in 30-second bursts at liquefaction setting (Oster blender) and centrifuged for 10 min at 4,080 x g. The supernatant was then filtered through 4 layers of cheesecloth and reserved. The pellets were the resuspended in 200 mL homogenization buffer and centrifugation was repeated. All of the supernatants were then pooled and centrifuged at 134,000 x g for 45 minutes. This pellet was resuspended in 32 mL 28% sucrose buffer (10 mM sodium phosphate, 0.1 mM EDTA, 0.02% NaN_3, pH 7.0). In order to isolate membrane proteins, the aliquots of resuspended pellet (8 mL each) were layered on top of a discontinuous sucrose gradient (10 mL 30% sucrose, 12 mL 35% sucrose, 7 mL 41% sucrose) and centrifuged at 121,800 x g for 4 hours. The membrane band at the top of the 35% sucrose layer was collected

using a thin glass transfer pipet, diluted 1:1 with deionized water, and centrifuged at 142,400 x g for 35 minutes. The membranes in the resulting pellet were base-extracted by resuspending them to approximately 0.5 mg/mL protein in water, and the pH was carefully titrated to 11.0 with NaOH, followed by stirring for 45 minutes. The base-extracted membranes were then centrifuged at 142,400 x g for 45 minutes, resuspended in buffer A (100 mM NaCl, 10 mM Tris-HCl, 0.1 mM EDTA, 0.02% NaN_3, pH 7.4), and flash-frozen in liquid nitrogen.

Solubilization of crude nicotinic acetylcholine receptor

The protein product from extraction was diluted to 2 mg protein/mL in buffer A. Sodium cholate (10% w/v) dissolved in buffer A was added to give a final cholate concentration of 1%. The mixture was then stirred for 30 minutes and centrifuged at 142,400 x g for 30 minutes. Finally, the supernatant was collected.

Preparation of asolectin liposomes for resuspension

Solid asolectin lipid was suspended in 4.16% cholate solution in buffer A to form a 65 mM solution, and the mixture was vortexed and sonicated at 20 °C under argon gas for ~45 minutes, and then stored at 0-4 °C until reconstitution.

Reconstitution of Torpedo *nicotinic acetylcholine receptors in asolectin liposomes*

Solubilized nAChRs, at confirmed 1-1.65 mg/mL concentration, were mixed with 0.3 mL of liposome/cholate mixture to yield a final volume of 1 mL, and a final concentration of 2% cholate. The mixture was dialyzed for 48 hours against 1,000 volumes buffer A,

changing the buffer every 12 hours. Before use in dialysis, buffer A was bubbled with argon gas for 15 minutes.

Oocyte microinjection

The glass injectors were 1.6 to 2 mm o.d., 1.2 to 1.6 mm i.d., and were pulled using using a Sutter instrument Co. Model P-97 puller. The oocytes were injected with 46 nL asolectin-resuspended nAChRs using a digital microdispenser (Drummond Nanoject II). The injected oocytes were incubated at 19 °C in a sterile solution containing Standard Barth's solution (SBS; 88mM NaCl; 1mM KCl; 0.4mM CaCl2; 0.33mM Ca(NO3)2; 0.8mM MgSO4; 5mM Tris-HCl; 2.4mM NaHCO3), supplemented with 50 mg/L gentamicin.

Two-Electrode Voltage Clamping of Oocytes

Sixteen hours after injection, the oocytes were clamped using a TEVC system. All ligands were dissolved in modified Barth's solution at different pHs and were perfused into the chamber using a gravity flow system. The buffers' different effective pHs meant that three ranges of running solutions were modified as follows: pH 6 and 6.5 were buffered with 2-(*N*-morpholino)ethanesulfonic acid (MES), pH 7 and 7.5 were buffered with tris(hydroxymethyl)aminomethane (Tris-HCl), and pH 8-9 were buffered with *N*-2-hydroxyethypiperazine-*N*'-2-ethanesulfonic acid (HEPES). Thyroid hormones were initially dissolved in 0.1 M NaOH. The oocytes were impaled with two 3 M KCl-filled glass microelectrodes (1-2 MΩ each) and were clamped at -60 mV with an OC-725C Oocyte Clamp (Warner Instruments). The bath solution was perfused at a rate of 10-13 mL/min. Each ligand perfusion lasted 60-70 seconds; after each perfusion, the bath solution was

exchanged with ligand-free buffer until the current response signal had returned to baseline for at least 120 seconds before the next application of ligand(s). Data were recorded using iWorx LabScribe v1.959.

Data analysis

The current flux signal for each administration of ligand was exported from iWorx into Matlab v2012b, and the raw data were normalized for each administration to the maximal current response (peak). The data was then trimmed to begin with the response as it reached 0.96 of the response peak (to avoid false inflection points by signal noise just after the response's maximum point), and end 35 seconds post-peak. The data was then curve-fitted to a two-degree exponential function (i.e., slow and fast response) ($y = a\,e^{-\frac{x}{A1}} + b\,e^{-\frac{x}{A2}}$). For each ligand/environmental condition (n=3, per condition), decay time and amplitude were calculated and averaged.

6.4 Results

PS and T3 inhibit nAChRs

Figure 2A shows the inhibitory effect of T3 on nAChR stimulation by 30 µM acetylcholine, as well as a representative trace of the reduction in response due to acetylcholine when co-applied with T3 (2A, inset). The apparent maximal effect of T3 near a neutral pH (seen at ≥ 100 µM) reduced the nAChR control response (~100-300 nA, depending on individual oocytes' flux capabilities) by 80 ± 6%, with an IC50 of 5.4 ± 1 µM T3. This is very similar to the IC50 of T3 for the $GABA_A$ receptor (8 ± 2 µM [215]).

Figure 2B shows the inhibitory effect of PS on nAChR stimulation by 30 µM acetylcholine, as well as a representative trace of the reduction in response due to acetylcholine when co-applied with PS (Figure 2B, inset). The apparent maximal effect of PS (seen at ≥100 µM) reduced the nAChR control response by 81 ± 4%, with an IC50 of 4.9 ± 3 µM PS. Triiodothyroacetic acid (triac), which lacks the amine group of T3, also inhibits the nAChR, with an IC50 of 109 ± 70 µM µM triac (Supplemental Figure 1). Further, allopregnanolone inhibits activity on nAChRs due to carbachol, an ACh agonist (IC50: 20 ± 13 µM) (Supplemental Figure 2).

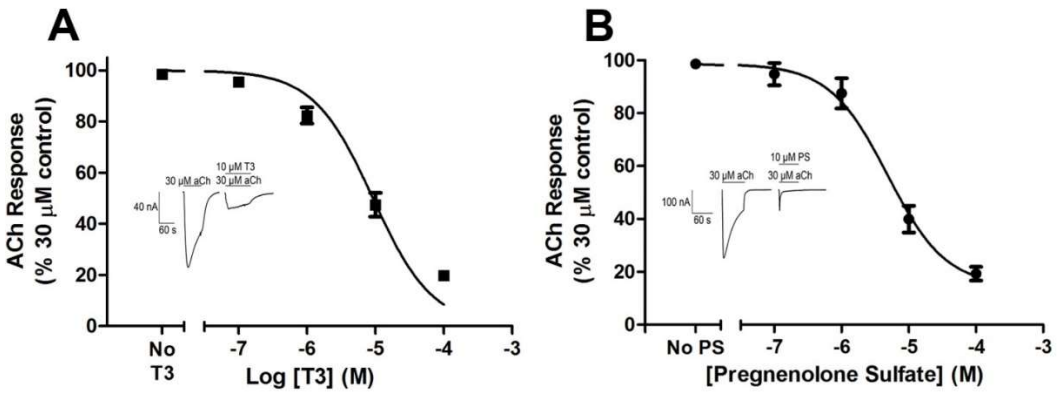

Figure 2. Inhibition of nicotinic acetylcholine receptor response to acetylcholine by T3 and PS. The dose-response curves for the effect of increasing concentrations of 0.1 µM-100 µM T3 (A) or 0.1 µM-100 µM PS (B) on ACh-stimulated current, represented as a percentage of the response to ACh without any additional ligands. Representative tracings show current responses due to application of ACh alone and ACh with T3 (A, inset) or PS (B, inset). Horizontal lines above each trace show the onset and duration of applied ligand(s). The data are represented as mean ± SEM. For each data point, n = 3-7.

Inhibition does not require a negatively charged molecule

The pH environment affects inhibition of nAChRs by T3 and PS. Dose response curves at each pH (6-9, in 0.5 pH increments) show the effect due to pH on the effect of dose of

T3 and PS (Figure 3A-G). A two-way ANOVA indicates that pH has a significant effect on nAChR flux for experiments using T3 ($p < 0.0001$, $F(6, 70) = 74.25$) or PS ($p < 0.0001$, $F(6, 70) = 24.02$) and that the effect due to the pH environment and due to T3 ($p < 0.0001$, $F(6,70) = 11.69$) or PS ($p < 0.0001$, $F(6,70) = 6.214$) dose have interactive effects on nAChR flux.

The effects of pH on inhibition of nAChRs by T3 and PS are different. From pH 6-7, the IC50 values of T3 and PS (Figure 3H) are similar. However, above the pK2 value of T3 (~7.5), the IC50 values of T3 and PS are distinct, with the T3 IC50s shifting downward relative to the IC50 values of PS. This divergence is coincident with the increase in extracellular pH above the pK2 value of T3. The PS IC50 value decreases below T3's at pH 9. This pH is where the net charge of T3, in which the hydroxyl group becomes anionic while the amine group remains neutral, becomes -1, and becomes more prominent than the neutral form dominant at lower pHs.

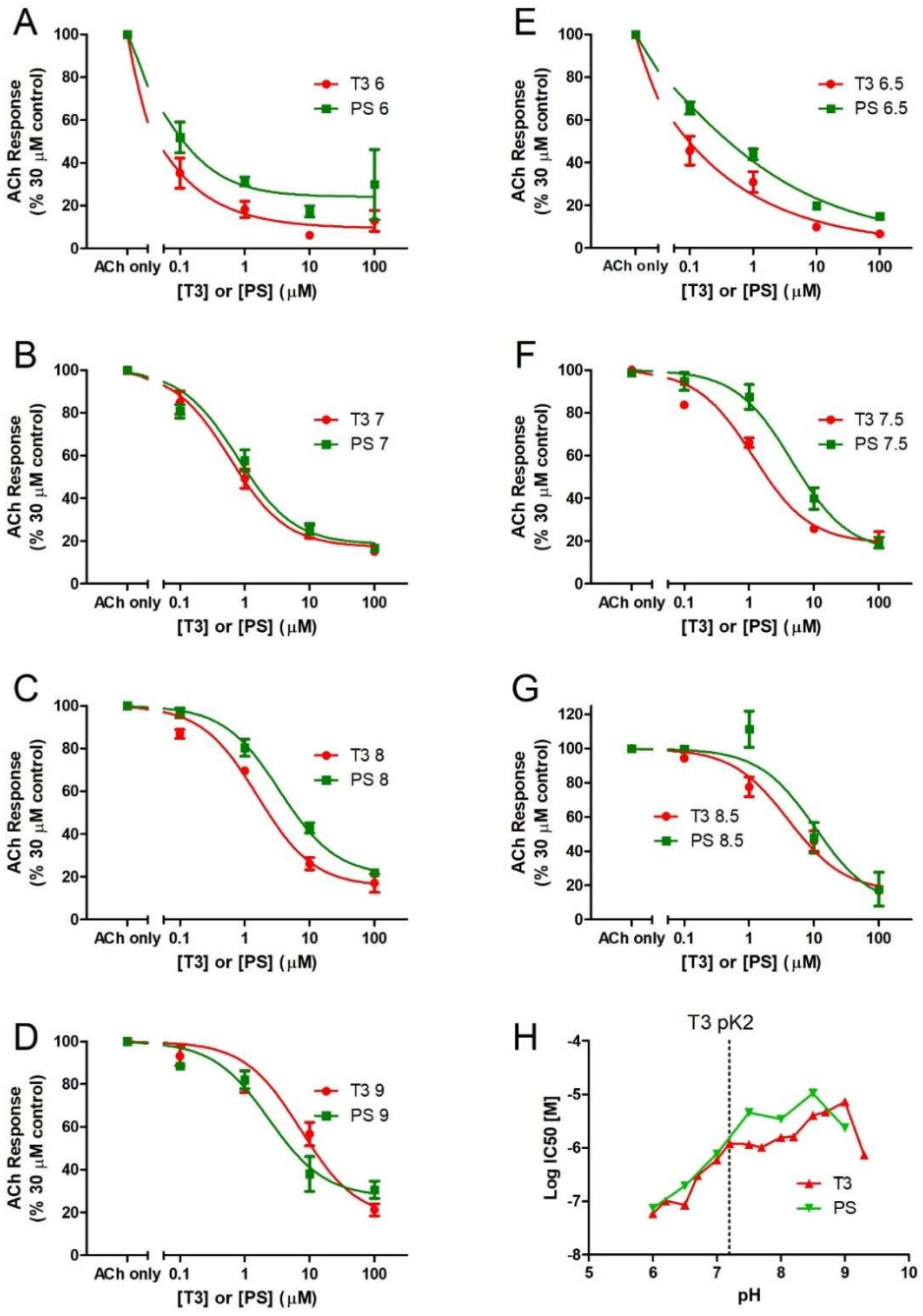

Figure 3. Effects of extracellular pH on inhibition of nAChRs by T3 and PS. The dose-response curves for the effect of increasing concentrations of 0.1 µM-100 µM T3 or 0.1 µM-100 µM PS on ACh-stimulated current at pH (A) 6, (B) 6.5, (C) 7, (D) 7.5, (E) 8, (F) 8.5, or (G) 9. Data in (A-G) are represented as a percentage of the response to ACh without any additional ligand. The data are represented as mean ± SEM. For each data point, n = 3. (H) compares the IC50 values generated from the inhibition curves at each pH

interval. T3 data is supplemented with inhibition experiments run at each pH level + 0.2 (data not shown). Dotted vertical line denotes the pK2 value of T3.

T3 and PS affect desensitization kinetics

Figure 4 and Figure 5 show representative traces of inhibition due to T3 and PS over 60-second administrations. Raw traces of 0-10 µM T3 or PS at pH 6 and 7.5 (Figure 4), or of a 10 µM dose of T3 or PS at each pH (6-9, in 0.5 pH increments) (Figure 5) demonstrate the effect due to ligand dose and pH desensitization of the channel.

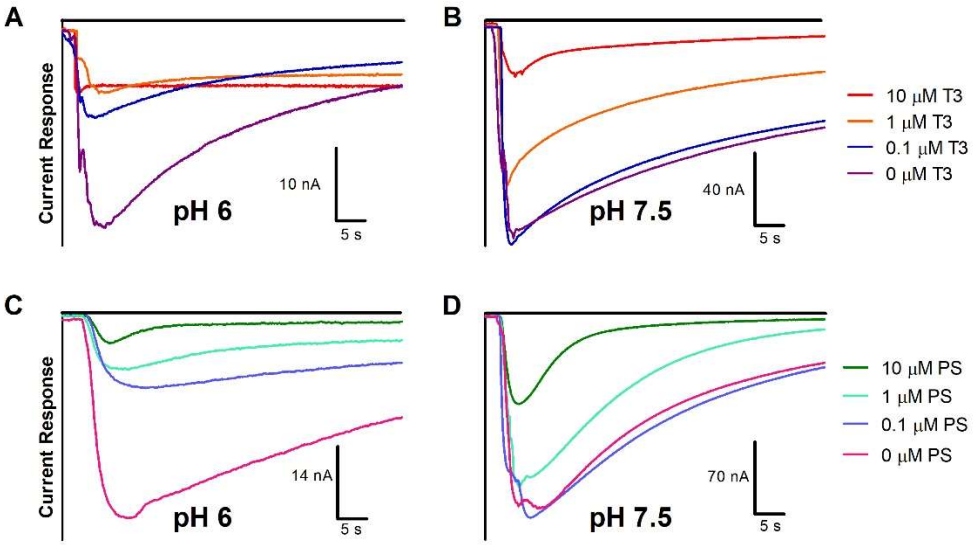

Figure 4. Effect of pH and T3 or PS on nAChR ion conductance. Raw current response traces after administration of 30 µM acetylcholine with (A) 0, 0.1, 1, or 10 µM T3 at pH 6, (B) 0, 0.1, 1, or 10 µM T3 at pH 7.5, (C) 0, 0.1, 1, or 10 µM PS at pH 6, or (D) 0, 0.1, 1, or 10 µM PS at pH 7.5. Traces are representative as close to average values of curve-fit amplitude and decay rate.

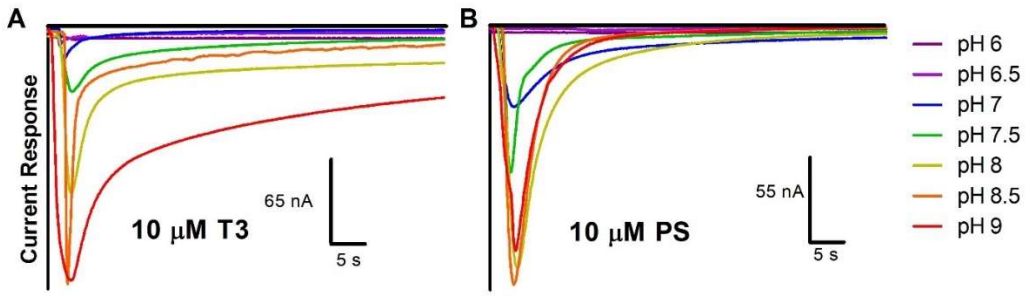

Figure 5. Effect of pH and 10 μM inhibitor on nAChR ion conductance. Raw current response traces after administration of 30 μM acetylcholine with (A) 10 μM T3 at differing pH levels or (B) 10 μM PS at differing pH levels. Traces are representative as close to average values of curve-fit amplitude and decay rate.

6.5 Discussion

Here we present the first direct observation of the inhibitory effect of T3 on nAChRs (Figure 2, Figure 3). The effect due to T3 on nAChRs is the same as the effect due to T3 on GABAA receptors. This is an unexpected result, as in general, ligand effects on GABAA receptors and nAChRs are opposite one another [232].

T3 may act as a neurosteroid-like inhibitor. Thyroid hormone crosses the blood-brain barrier [135-137], and nerve terminal fractions show T3 concentrations of 13.0-65 nM [233, 234]. When injected into the median preoptic nucleus of freely-moving rats, T3 increases REM sleep and wakefulness [173, 174]. T3 directly inhibits $GABA_A$ receptor activity [154, 215].

The current study shows that the possible neurosteroid-like inhibition of nAChRs, however, does not require a charged molecule. Inhibition of nAChRs by T3 from pH 6-9 retains efficacy (Figure 3), including at those pH environments in which T3 is neutral.

Therefore, the mechanism of binding on the nAChR may not depend upon a charged headgroup of the inhibitory molecule.

For the first time, we also demonstrate an inhibitory effect due to PS on nAChR activity (Figure 2B). This effect is comparable to the inhibitory effect due to PS on $GABA_A$ receptors [235], and to T3's effect on nAChRs (Figure 2A) and $GABA_A$ receptors [215]. However, the present study gives more insight into the complexity of neurosteroid/neurosteroid-like binding at each receptor: in $GABA_A$ receptors, allopregnanolone acts as a receptor activator [215], whereas to nAChRs, allopregnanolone acts as an inhibitor (Supplemental Figure 2). If allopregnanolone binds to the same site as PS, this implies that PS's sulfate group, theorized to interact with a residue near the base of the $GABA_A$ TMD [223], is not necessary for binding on the analogous site on nAChRs, and, is not required to confer inhibitory action. Further, the ability of triac to inhibit nAChRs illustrates that the amine group on T3 is not required for inhibition of the channel either.

Although the T3 and PS molecules have nearly identical volume and shape, with T3's 3'-iodine/4'-hydroxyl group in the same relative position as the PS's sulfate group, and T3's inner ring iodines' similarity to PS's methyl and ring carbons [219], it is still unknown what molecular features facilitate binding to $GABA_A$Rs or to nAChRs. The features that distinguish them appear not to be necessary to inhibit each channel, as the actions of allopregnanolone and triac show. Similarities between both ligands may elucidate the molecular features necessary for such binding.

However, available evidence indicates that binding of both T3 and PS occurs at the TMD. Experimental and *in silico* simulation data suggest T3 and allopregnanolone share a binding site on $GABA_A$ receptors [215]. Here we show that T3 and PS both affect channel desensitization (Figure 4, Figure 5). The effect of each ligand on nAChR desensitization may be involved with a region homologous to the desensitization gate structure of $GABA_A$ receptors, where PS has been shown to bind. This binding is theorized to cause constriction at the base of the channel pore, inducing a desensitized state [223]. We show that different pH levels, while not affecting either ligand's ability to bind, appear to affect T3 and PS-induced nAChR desensitization. This may indicate pH influence on channel residues at the TMD, as has been suggested by previous investigations [230, 231].

The inhibitory action of PS and the inhibitory, neurosteroid-like action of T3 on the nAChR indicate a complex structure-function relationship. The actions of both ligands relative to one another, and to the nearly identical molecules allopregnanolone and triac, give insight about what may be necessary to facilitate binding and inhibition of the channel, and, more clearly, what is not.

Chapter 7: Appendix

7.1 nAChRs, Carbachol, and Acetylcholine

Introduction

Studies of the nAChR in its synaptic environment or in radiolabeled cation liposomal reconstitution studies are performed with carbamylcholine (carbachol) [236-238], an ACh agonist which activates both nicotinic and muscarinic acetylcholine receptors and inhibits cholinesterases [239]. Although *Xenopus* oocyte TEVC studies, more rapid experiments unaffected by acetylcholinesterase, use ACh when interrogating channel function, we performed initial experiments using carbachol, whose high stability [240] would afford more time during the initiation and troubleshooting phases of optimizing experimental procedures. After optimizing TEVC procedures and establishing a concentration curve for carbachol, we repeated the procedure with ACh.

Results

Carbachol (EC50 = 326.2 ± 110 μM; n = 10) is nearly ten times less potent than ACh (EC50 = 34.05 ± 7.2 μM; n = 12 (Figure 1B). Raw, un-normalized carbachol's evoked nAChR response (1.098 ± 0.2802, A.U.; n=10) demonstrates less efficacy than ACh's (1.972 ± 0.6407, A.U.; n=12) (Figure 1A).

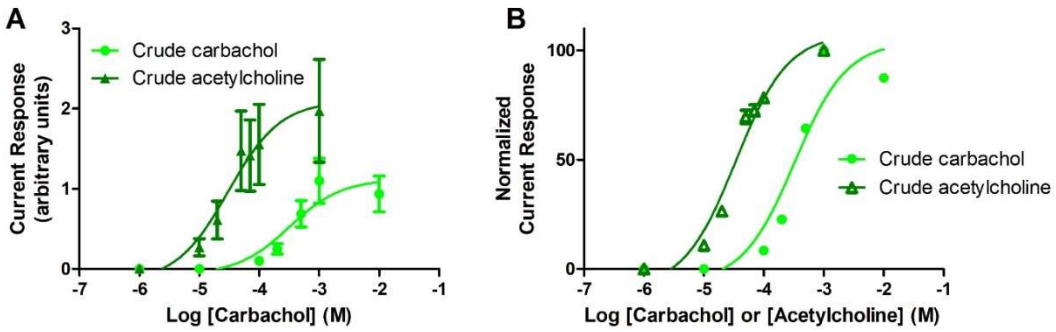

Figure 1. Dose-response curves for raw and normalized current response due to carbamylcholine or acetylcholine in crude-membrane-injected *Xenopus* oocytes. The values are expressed as a mean of 10 (carbachol) or 12 (acetylcholine) separate determinations. Error bars represent the standard error of the mean (SEM).

Discussion

A single-channel conductance study of mouse neuronal nAChRs using carbachol and ACh has identified them as having nearly identical potencies as in the current study, as well as establishing carbachol's much lower association rate relative to ACh's, but carbachol demonstrated an 88% efficacy at maximal doses compared to the effect due to ACh maximal doses [241], instead of carbachol's 55% efficacy compared to ACh seen in the present study. This difference could be due to variations in nAChR ion channel conductance in different oocyte preparations, a noted complication in oocyte TEVC expression systems [242-244].

ACh binding is implicated at the nAChR α-δ and α-γ intersubunit interfaces [245-247], near the C-loop at the β8-β10 hairpin of the α subunit [248, 249]. A crystal structure of acetylcholine-binding protein (AChBP), a putatively-comparable homolog of the extracellular domain of *Torpedo* nAChRs [249], shows carbachol bound at the same C-

loop region [250]. If acetylcholine had proven difficult to work with in our TEVC procedures, experiments interrogating the manner of antagonist inhibition could use carbachol as an acceptable substitute. While all inhibition studies of T3 and PS in variable pH environments (Chapter 6.4) used ACh as the agonist, carbachol was used in several preliminary experiments and inhibition studies. As all preceding data using carbachol in the studies have been normalized to each oocyte's own maximum evoked ion current response, the implications of the data should be applicable to those of experiments using ACh as the agonist.

7.2 nAChRs, Nicotine, and *Xenopus* oocytes

Introduction

Although several ligands activate both nicotinic and muscarinic receptors (carbachol and ACh among them), an acetylcholine receptor classified as nicotinic implies that nicotine acts as a receptor agonist and muscarine does not [251]. Nicotine activates neuronal-type nAChRs, some subtypes having a higher affinity for nicotine than they do for ACh [252, 253] , with the α7 subtype conferring more sensitivity than other CNS subtypes [254]. A crystal structure of AChBP shows nicotine bound in the same position as carbachol [250].

However, in muscle-type nAChRs, the EC50 potency of nicotine is ~1000-fold lower than acetylcholine [241], and its energetic favorability of binding to the *Torpedo* nAChR, while close to that of ACh itself, is not efficacious at eliciting ion flux at appropriate doses due to low affinity for resting receptors (K_d = 1 mM) and self-inhibition [237, 255].

Mutagenesis of a single amino acid (α153) from glycine to lysine in muscle-type nAChRs caused a nearly-10,000-fold increase in nicotine's binding affinity to the nAChR in resting state [255]. Unfortunately, no structural information is available to illustrate the differential binding or receptor conformational change attributable to this mutagenesis.

Nicotine's self-inhibition at the nAChR, speculated to be non-specific perturbation of the cell membrane surrounding the receptor, has an experimental Hill coefficient of 1 in one study, implying a competitive inhibition action with either one site or several sites that share the same affinity [237]. As ethanol increases cholinergic binding affinity [256], increasing environmental ethanol in postsynaptic *Torpedo* membranes increased nicotine efficacy in a dose-dependent manner [257]. However, this experiment generated an inhibitory Hill coefficient of 2 for nicotine in the absence of ethanol, implying its possible noncompetitive inhibition at high doses.

Studies of nicotine on muscle-type and *Torpedo* nAChRs have been performed in synaptic membranes and single-channel studies but not in *Xenopus* oocyte expression TEVC. Nicotine-evoked traces over extended application might give insight into the desensitization mechanisms of the receptor.

We administered different nicotine concentrations to *Torpedo* nAChRs expressed in *Xenopus* ooctyes in order to study desensitization of prolonged nicotine administration. The *Xenopus* TEVC method could yield fast versus slow self-inhibition after curve-fitting the raw traces and could further elucidate the binding mechanism of nicotine in light of previous investigations.

Results

Figure 1 shows that infusion with 1 mM nicotine, which would evoke ~half-maximal current response in other nAChR experiment modes, evoked no observable current relative to baseline. We attribute the lack of response at this dose to be on par with other experiments involving *Torpedo* nAChRs. In those studies, response due to nicotine was not observable at activating concentrations and required either ethanol [257] or specialized vesicular-release methods [237] to elicit observable flux. Lower doses also showed lack of response (data not shown). Higher concentrations of nicotine evoked a slow (~20-second) change in ion flux that disappeared at washing, but this response was also seen in control oocytes which did not express nAChRs.

However, after preincubation for 1 minute with 1.5 M ethanol and when co-applied with the same concentration, 10 μM nicotine evoked a response, as predicted. This response repeated several times; however, the response diminished substantially with each consequent administration. The same ethanol conditions run in a control oocyte not expressing nAChRs showed no response by nicotine (data not shown).

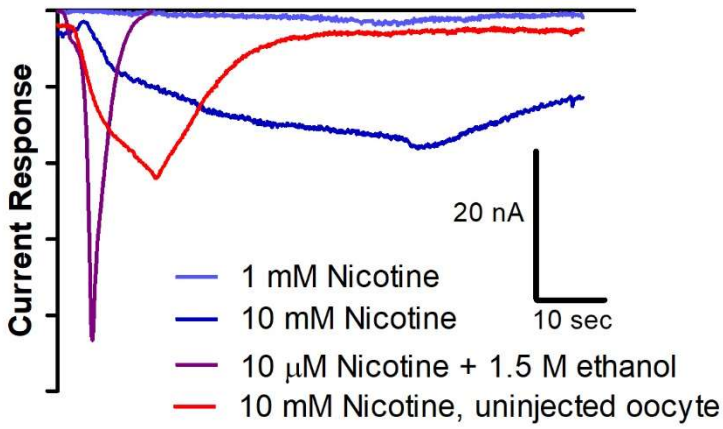

Figure 1. Raw traces of current response evoked by nicotine preparations in *Torpedo* nAChRs. Responses to administration of nicotine at mid and high concentrations alone (blue traces), of nicotine at high concentration in an oocyte not injected with reconstituted nAChRs (orange trace), and of 10 μM nicotine administered with 1.5 M ethanol (violet trace).

Discussion

The evoked current by 10 mM nicotine in oocytes not expressing nAChRs indicates nicotine influence on the oocyte membrane itself. In another control oocyte, administration of 100 mM nicotine cause a sudden drop in baseline which went beyond the scope of the recording hardware, returning to normal after 2 minutes of washing with buffer (data not shown). This effect may be due to the pH of nicotine: at 50 mM, the pH of nicotine solution is at 10.3 [258]. This pH may have adverse effects on any TEVC setup and may account for the slow change in baseline seen in both nAChR-expressing and control oocytes.

1.5 M ethanol has an adverse effect on *Xenopus* oocytes, as the baseline signal was comparably erratic compared to buffer without ethanol. Further, oocytes lost stable baseline entirely within 5 minutes in 1.5 M ethanol buffer, preventing the available

timeline necessary to investigate desensitization conditions. As conditions were too difficult to merit extensive study, we did no further experiments with nicotine.

7.3 nAChRs and Lipid preparations

Introduction

The endogenous membrane surrounding nAChRs is a heterogenous matrix of cholesterol, glycerophospholipids, and sphingolipids [259-261]. Controlled proportions of certain lipids, as well as limiting the amount of cholesterol, affect nAChR channel function. At least 40 mol% cholesterol in the *Torpedo* lipid environment is required for function [225, 262]. Further study revealed that in more controlled lipid environments, more exacting distinctions can be made: phosphatidylcholine (PC)-containing membranes with even relatively small amounts of phosphatidic acid (PA) and cholesterol will support functional receptors [263, 264], as will PC-containing membranes with sufficiently high amounts of PA. The present consensus view is that PA and cholesterol can be absent from the lipidic matrix and still retain functional nAChRs, but the absence of both yields non-functional nAChRs (for review, see [265]).

Another factor of heterogeneity of the membrane surrounding nAChRs is the phase-state of the constitutive lipids. Membrane phospholipids, with two parallel or semi-parallel hydrophobic fatty acid hydrocarbon chains joined by a phosphate group which forms part (or all) of the charged, hydrophilic headgroup, have variabilities leading to different phase behavior. Unsaturation of the fatty acids can cause conformational shifts, leading to less order when arranged in large quantities. This could facilitate the

formation of lipid rafts, in which more ordered phospholipids and cholesterol coalesce and become distinguished from surrounding, disordered unsaturated lipids [266]. Such ordering may have functional consequences, as mutation of the cysteine at α418 on the M4 TM domain helix to tryptophan decreases nAChR function [267], and *in vitro*, function is restored in these mutants upon cholesterol depletion [268]. This may implicate membrane microdomains in nAChR function [269]. Preferential cholesterol distribution in the membrane can add complexity to interpreting nAChR functionality; whether it depends primarily on lipid mixture proportion, or on the subtler relationship of lipid conditions that give rise to appropriate bulk membrane conditions, is controversial (for review, see [265]).

Preparations of nAChRs substituting specific detergents for endogenous phospholipids demonstrate functionality based on their acyl chain length and headgroups, although these results do not yield a clear pattern for either feature [270, 271]. Systematic study of unsaturation on nAChR function has not, as yet, been performed.

We tested nAChR function in *Xenopus* oocytes expressing equivalent concentrations of *Torpedo* nAChRs in crude membrane extracts or nAChRs reconstituted in a sodium cholate (a cholesterol analog)-asolectin (phosphatidic acid (6.6%), phosphatidylinositol (16.5%), phosphatidylethanolamine (12.9), and phosphatidylcholine (20.7%)) mixture. We demonstrate higher amounts of ion flux at the same carbachol or ACh doses by asolectin-injected oocytes than crude-membrane-injected oocytes; however, the respective concentration curves for both each ligand in both preparation conditions have statistically indistinct EC50, maximal ion flux, and sensitivity values.

Results

Figure 1 shows the raw and normalized current responses due to carbachol and ACh in each nAChR preparation. Figure 1A and 1C show the higher ion flux amplitude at all carbachol and ACh doses, yet Figure 1B and 1D show that the concentration curves are essentially identical, possessing the same EC50 value (crude EC50 = 326.2 ± 110 µM, n = 10; asolectin EC50 = 34.05 ± 7.2 µM, n = 9).

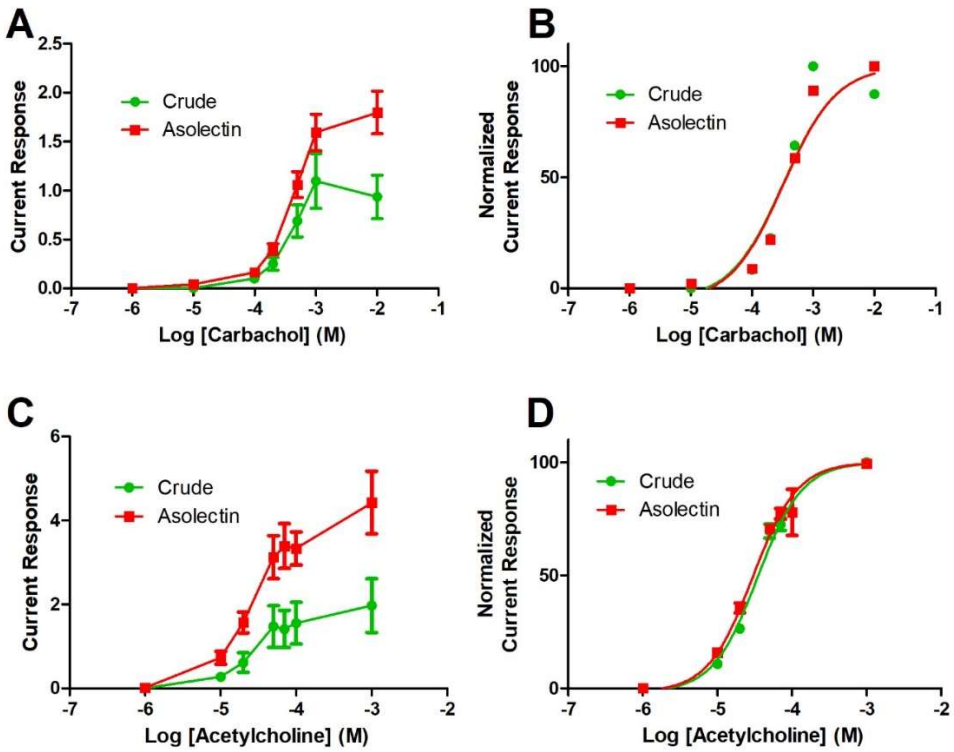

Figure 1. Ion flux in nAChRs evoked by carbachol and ACh in differential nAChR preparations. Oocytes were injected with either crude membrane (green circles) or sodium cholate-asolectin reconstituted nAChRs (red squares) and subjected to increasing doses of carbachol or ACh. Error bars denote standard error of the mean (SEM).

Discussion

Asolectin-reconstituted nAChRs exhibit higher ion flux amplitudes due to carbachol or ACh than do nAChRs in *Torpedo* crude membrane extracts. This difference, however, does not extend to measures of potency, as the EC50 values of each preparation are not distinct. Consistent concentrations of nAChRs in equivalent injection volumes prevented effects due to number of receptors in a given oocyte.

Asolectin lipid reconstitution is known to lead to functional channels [242]. Its lipid content is heterogenous, as are endogenous receptors, yet the reason for increased ion flux amplitude seen here is not accounted for.

When nAChRs reach the oocyte membrane, accounting for the immediate nAChR lipid environment is difficult, given the small amount of injection volume (46 nL) compared to the membrane bilayer (0.5 mm diameter). Since all experiments were performed > 16 hours after injection into the oocyte, with consistent results day to day, it is unlikely that short-term (i.e., milliseconds to minutes), annular lipid diffusion of membrane components [272, 273] in crude or reconstituted nAChR injections accounts for the difference seen in ion flux amplitude. However, non-annular lipids may have slower diffusion rates [274], which may have implications to both the results seen here and to the lipid environment-function relationship in general.

The mechanisms of translocation of the nAChR to the oocyte membrane is not well-understood [242]. Inherent properties of lipids surrounding the nAChRs between preparations, or the relative purity of each preparation, could cause differential

amounts of expression or different orientation of nAChRs in the membrane itself, with a higher proportion of asolectin-reconstituted nAChRs having more favorable orientation or translocation to the membrane.

Interrogation of this issue could be performed by photolabeling a component of the extracellular domain (e.g., with a tagged, irreversibly-binding toxin like α-bungarotoxin) in intact oocytes and comparing it to the same photolabeling of oocytes which have been pierced, allowing access to the inside of the oocyte [244]. The difference in photolabeling between both preparation conditions would give insight to both gross receptor placement and orientation of the receptor.

7.4 nAChRs and Ivermectin

Ivermectin (IVM), a compound with powerful anthelmintic effects [275], selectively kills invertebrates by binding to glutamate-gated chloride channels (GluClRs) [276]. GluClRs, like $GABA_A$, 5-HT3, glycine, and some human nACh receptors, are part of the Cys-loop receptor family, but lower IVM potency in mammalian receptor types make it an effective antiparasitic [277-280]. A resolved crystal structure shows IVM bound to each of the 5 intersubunit interfaces between M1 and M3 helices in the transmembrane (TM) domain of GluClα [281]. Differences between the GluCl and $GABA_A$ receptors make identification of the binding site in $GABA_A$ receptors ambiguous; some theories related to binding residues on GluClRs including a glycine on the M3 helix which $GABA_A$Rs lack [282, 283], and hydrogen bonds with several residues on the M2 helix [281] that differ

in $GABA_A$Rs may explain differences in IVM affinity or binding orientation to $GABA_A$Rs [284].

IVM nevertheless activates α1β1γ2 $GABA_A$Rs in the 0.1 μM– 125 μM concentration range, maximally at 20–50 μM and with an EC50 of 7.1 ± 0.8 μM [215]. 3,3',5-Triiodothyronine (T3) inhibits IVM action on α1β1γ2 $GABA_A$Rs, and a Schild analysis suggests a possible competitive mode of inhibition, although vulnerabilities of Schild analysis and incomplete inhibition of IVM by T3 prevent certainty about a simple relationship [215]. Docking studies with IVM show that it could bind at any of the five intersubunit TM domain interfaces in $GABA_A$Rs, with the most favorable site being at the β-α subunit interface.

Nicotinic acetylcholine receptors, however, show different data. Direct administration of IVM showed no effect on ion channel flux when compared with infusion with its vehicle solution (buffer containing 1% DMSO, which caused a slight and gradual change in baseline current) (data not shown). Co-administration of 30 μM IVM with increasing amounts of carbachol showed no statistically significant difference in evoked current. Inspection of the concentration curve indicates a possible, slight potentiating effect due to 30 μM IVM of carbachol at low carbachol doses, but this effect does not reach significance (data not shown).

To account for the lack of response of nAChRs to IVM, we considered the respective structures of nAChRs and IVM-activatable receptors. Inspection of differences between IVM-activatable GluClRs and nAChRs show that a leucine inhabits the M3 glycine

position, and homologous residue orientations are changed relative to one another [284]. This may account for the differential activity of IVM in GluCl when compared to action at nAChRs.

7.5 nAChRs and Isoflurane

Introduction

General anesthetic action is not fully understood despite nearly 170 years of medical relevance [285]. Isoflurane, a volatile, halogenated inhaled anesthesia, inhibits nAChRs, yet its precise binding site (and precise number of binding sites on the receptor) is not presently known. However, three likely binding sites exist for isoflurane in the nAChR: at an intersubunit site, at an intrasubunit site unique to the nAChR, and at the nAChR channel pore [286]. Functional study of the related prokaryotic Gloeobacter ligand-gated ion channel (GLIC) shows functional evidence of multiple sites of inhaled anesthesia binding, possibly suggesting negative cooperativity, in which the binding of one ligand molecule to the receptor precludes binding of another molecule to another site at low concentrations [287].

We administered increasing concentrations of isoflurane with EC50-evoking acetylcholine concentrations of both crude-membrane and asolectin-reconstituted nAChR preparations in oocytes in order to investigate the possibility of multiple binding sites predicted previously [286]. We found evidence suggesting multiple inhibitory binding sites for isoflurane, although specificity about binding affinity to such sites cannot be drawn conclusively from the data.

Results

The inhibition curve of ACh-evoked ion flux is different than those of other inhibitors in the present study. This inhibitor, at high concentration, leads to 100% abolishment of ACh-evoked ion flux. Also, the inhibitory effect is seemingly biphasic, an effect seen in other investigations of the halogenated inhalants halothane on nAChRs [288] and of isoflurane in GLIC [287]. The inhibition curves of both crude membrane and asolectin-reconstituted nAChRs were similar, showing an initial inhibition at low concentration, followed by a lack of inhibition (or, in crude-membrane-based preparations, potentiation), followed by abrogation of ACh-elicited signal.

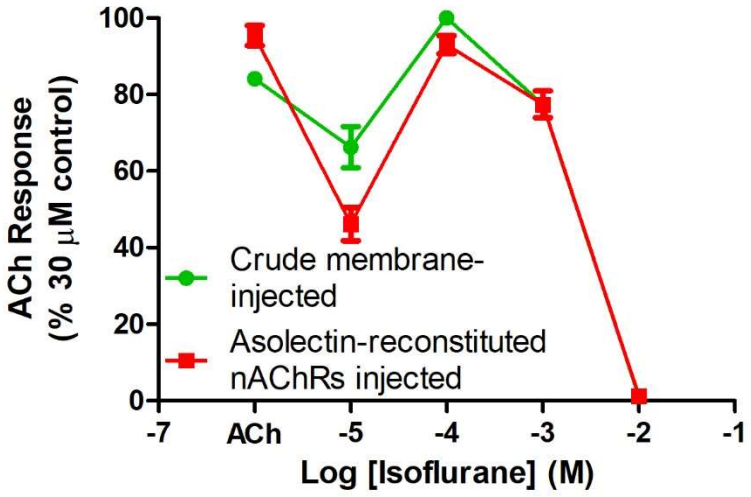

Figure 1. Inhibition of nAChRs by isoflurane. Oocytes were injected with either crude membrane (green circles) or sodium cholate-asolectin reconstituted nAChRs (red squares) and subjected to increasing doses of isoflurane in addition to 30 μM ACh. Error bars denote standard error of the mean (SEM).

Discussion

We describe a biphasic inhibition of ACh-evoked ion flux due to isoflurane, which inhibits, lacks inhibition/potentiates, and blocks all ion flux at increasing concentrations. This is consistent with data seen in other studies of similar anesthetics [289] and may give evidence for more than one isoflurane binding site, as has been predicted [286]. Theoretical prediction also may explain the potentiating effect noted at 100 μM isoflurane, as a unique sequence variation in nAChRs affords a possible potentiating intrasubunit site not seen in some related channels. If a multiple-site binding modality is true, these results may exhibit negative cooperativity, as has been suggested in isoflurane experiments with GLIC [287], which, notably, showed no potentiating effect due to isoflurane.

7.6 nAChRs and Supplemental Figures

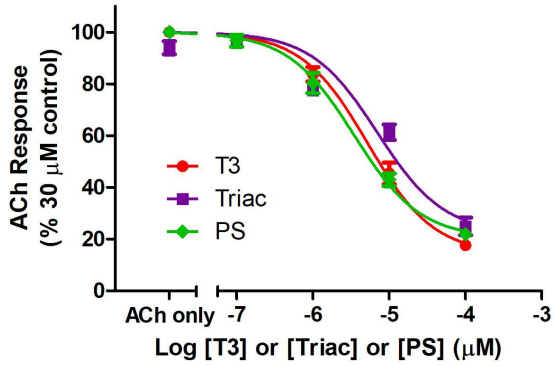

Supplemental Figure 1. Inhibition of nicotinic acetylcholine receptor response to acetylcholine by T3, PS, and triac. The dose-response curves for the effect of increasing concentrations of 0.1 µM-100 µM T3, PS, or triac on ACh-stimulated current, represented as a percentage of the response to ACh without any additional ligands. The data are represented as mean ± SEM. For each data point, n = 3-7.

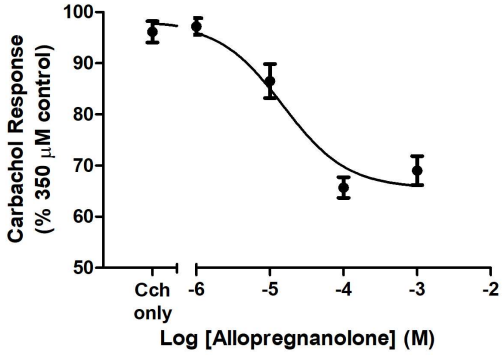

Supplemental Figure 2. Inhibition of carbachol by allopregnanolone. The dose-response curves for the effect of increasing concentrations of 0.1 µM-100 µM allopregnanolone on carbachol (Cch)-stimulated current, represented as a percentage of the response to carbachol without any additional ligands. The data are represented as mean ± SEM. For each data point, n = 5.

Bibliography

1. Johnson CH, Knight MR, Kondo T, Masson P, Sedbrook J, Haley A, et al. Circadian oscillations of cytosolic and chloroplastic free calcium in plants. Science (New York, NY). 1995;269(5232):1863-5. Epub 1995/09/29. PubMed PMID: 7569925.

2. Ditty JL, Williams SB, Golden SS. A cyanobacterial circadian timing mechanism. Annual review of genetics. 2003;37:513-43. Epub 2003/11/18. doi: 10.1146/annurev.genet.37.110801.142716. PubMed PMID: 14616072.

3. Aronson BD, Johnson KA, Loros JJ, Dunlap JC. Negative feedback defining a circadian clock: autoregulation of the clock gene frequency. Science (New York, NY). 1994;263(5153):1578-84. Epub 1994/03/18. PubMed PMID: 8128244.

4. Hardin PE, Panda S. Circadian timekeeping and output mechanisms in animals. Current opinion in neurobiology. 2013;23(5):724-31. Epub 2013/06/05. doi: 10.1016/j.conb.2013.02.018. PubMed PMID: 23731779; PubMed Central PMCID: PMCPMC3973145.

5. Halberg F. Chronobiology. Annual review of physiology. 1969;31:675-725. Epub 1969/01/01. doi: 10.1146/annurev.ph.31.030169.003331. PubMed PMID: 4885778.

6. Ripperger JA, Jud C, Albrecht U. The daily rhythm of mice. FEBS letters. 2011;585(10):1384-92. Epub 2011/03/01. doi: 10.1016/j.febslet.2011.02.027. PubMed PMID: 21354419.

7. Akiyama M, Kouzu Y, Takahashi S, Wakamatsu H, Moriya T, Maetani M, et al. Inhibition of light- or glutamate-induced mPer1 expression represses the phase shifts into the mouse circadian locomotor and suprachiasmatic firing rhythms. The Journal of neuroscience : the official journal of the Society for Neuroscience. 1999;19(3):1115-21. Epub 1999/01/27. PubMed PMID: 9920673.

8. Takahashi JS, DeCoursey PJ, Bauman L, Menaker M. Spectral sensitivity of a novel photoreceptive system mediating entrainment of mammalian circadian rhythms. Nature. 1984;308(5955):186-8. Epub 1984/03/08. PubMed PMID: 6700721.

9. Stephan FK, Zucker I. Circadian rhythms in drinking behavior and locomotor activity of rats are eliminated by hypothalamic lesions. Proceedings of the National Academy of Sciences of the United States of America. 1972;69(6):1583-6. Epub 1972/06/01. PubMed PMID: 4556464; PubMed Central PMCID: PMCPMC426753.

10. Sehgal A, Price JL, Man B, Young MW. Loss of circadian behavioral rhythms and per RNA oscillations in the Drosophila mutant timeless. Science (New York, NY). 1994;263(5153):1603-6. Epub 1994/03/18. PubMed PMID: 8128246.

11. Stokkan KA, Yamazaki S, Tei H, Sakaki Y, Menaker M. Entrainment of the circadian clock in the liver by feeding. Science (New York, NY). 2001;291(5503):490-3. Epub 2001/02/13. doi: 10.1126/science.291.5503.490. PubMed PMID: 11161204.

12. Fuchikawa T, Eban-Rothschild A, Nagari M, Shemesh Y, Bloch G. Potent social synchronization can override photic entrainment of circadian rhythms. Nature communications. 2016;7:11662. Epub 2016/05/24. doi: 10.1038/ncomms11662. PubMed PMID: 27210069; PubMed Central PMCID: PMCPMC4879263.

13. Menaker M, Eskin A. Entrainment of circadian rhythms by sound in Passer domesticus. Science (New York, NY). 1966;154(3756):1579-81. Epub 1966/12/23. PubMed PMID: 5924929.

14. Mills JN, Minors DS, Waterhouse JM. Adaptation to abrupt time shifts of the oscillator(s) controlling human circadian rhythms. The Journal of physiology. 1978;285:455-70. Epub 1978/12/01. PubMed PMID: 745108; PubMed Central PMCID: PMCPMC1281767.

15. Reebs SG, Mrosovsky N. Effects of induced wheel running on the circadian activity rhythms of Syrian hamsters: entrainment and phase response curve. Journal of biological rhythms. 1989;4(1):39-48. Epub 1989/01/01. doi: 10.1177/074873048900400103. PubMed PMID: 2519579.

16. Panda S, Antoch MP, Miller BH, Su AI, Schook AB, Straume M, et al. Coordinated transcription of key pathways in the mouse by the circadian clock. Cell. 2002;109(3):307-20. Epub 2002/05/23. PubMed PMID: 12015981.

17. Provencio I, Cooper HM, Foster RG. Retinal projections in mice with inherited retinal degeneration: implications for circadian photoentrainment. The Journal of comparative neurology. 1998;395(4):417-39. Epub 1998/06/10. PubMed PMID: 9619497.

18. Panda S, Provencio I, Tu DC, Pires SS, Rollag MD, Castrucci AM, et al. Melanopsin is required for non-image-forming photic responses in blind mice. Science (New York, NY). 2003;301(5632):525-7. Epub 2003/06/28. doi: 10.1126/science.1086179. PubMed PMID: 12829787.

19. Foster RG, Provencio I, Hudson D, Fiske S, De Grip W, Menaker M. Circadian photoreception in the retinally degenerate mouse (rd/rd). Journal of comparative physiology A, Sensory, neural, and behavioral physiology. 1991;169(1):39-50. Epub 1991/07/01. PubMed PMID: 1941717.

20. Lowrey PL, Takahashi JS. Genetics of the mammalian circadian system: Photic entrainment, circadian pacemaker mechanisms, and posttranslational regulation. Annual review of genetics. 2000;34:533-62. Epub 2000/11/28. doi: 10.1146/annurev.genet.34.1.533. PubMed PMID: 11092838.

21. Altimus CM, Guler AD, Alam NM, Arman AC, Prusky GT, Sampath AP, et al. Rod photoreceptors drive circadian photoentrainment across a wide range of light intensities. Nature neuroscience. 2010;13(9):1107-12. Epub 2010/08/17. doi: 10.1038/nn.2617. PubMed PMID: 20711184; PubMed Central PMCID: PMCPMC2928860.

22. Hatori M, Le H, Vollmers C, Keding SR, Tanaka N, Buch T, et al. Inducible ablation of melanopsin-expressing retinal ganglion cells reveals their central role in non-image forming

visual responses. PloS one. 2008;3(6):e2451. Epub 2008/06/12. doi: 10.1371/journal.pone.0002451. PubMed PMID: 18545654; PubMed Central PMCID: PMCPMC2396502.

23. Ostergaard J, Hannibal J, Fahrenkrug J. Synaptic contact between melanopsin-containing retinal ganglion cells and rod bipolar cells. Investigative ophthalmology & visual science. 2007;48(8):3812-20. Epub 2007/07/27. doi: 10.1167/iovs.06-1322. PubMed PMID: 17652756.

24. Koch KW, Duda T, Sharma RK. Photoreceptor specific guanylate cyclases in vertebrate phototransduction. Molecular and cellular biochemistry. 2002;230(1-2):97-106. Epub 2002/04/16. PubMed PMID: 11952100.

25. Detwiler P. Open the loop: dissecting feedback regulation of a second messenger transduction cascade. Neuron. 2002;36(1):3-4. Epub 2002/10/09. PubMed PMID: 12367499.

26. Ladant D. Calcium and membrane binding properties of bovine neurocalcin delta expressed in Escherichia coli. The Journal of biological chemistry. 1995;270(7):3179-85. Epub 1995/02/17. PubMed PMID: 7852401.

27. Zozulya S, Stryer L. Calcium-myristoyl protein switch. Proceedings of the National Academy of Sciences of the United States of America. 1992;89(23):11569-73. Epub 1992/12/01. PubMed PMID: 1454850; PubMed Central PMCID: PMCPMC50594.

28. Krishnan A, Venkataraman V, Fik-Rymarkiewicz E, Duda T, Sharma RK. Structural, biochemical, and functional characterization of the calcium sensor neurocalcin delta in the inner retinal neurons and its linkage with the rod outer segment membrane guanylate cyclase transduction system. Biochemistry. 2004;43(10):2708-23. Epub 2004/03/10. doi: 10.1021/bi035631v. PubMed PMID: 15005606.

29. Venkataraman V, Duda T, Ravichandran S, Sharma RK. Neurocalcin delta modulation of ROS-GC1, a new model of Ca(2+) signaling. Biochemistry. 2008;47(25):6590-601. Epub 2008/05/27. doi: 10.1021/bi800394s. PubMed PMID: 18500817; PubMed Central PMCID: PMCPMC2844899.

30. Okazaki K, Obata NH, Inoue S, Hidaka H. S100 beta is a target protein of neurocalcin delta, an abundant isoform in glial cells. The Biochemical journal. 1995;306 (Pt 2):551-5. Epub 1995/03/01. PubMed PMID: 7887910; PubMed Central PMCID: PMCPMC1136553.

31. Wen XH, Duda T, Pertzev A, Venkataraman V, Makino CL, Sharma RK. S100B serves as a Ca(2+) sensor for ROS-GC1 guanylate cyclase in cones but not in rods of the murine retina. Cellular physiology and biochemistry : international journal of experimental cellular physiology, biochemistry, and pharmacology. 2012;29(3-4):417-30. Epub 2012/04/18. doi: 10.1159/000338496. PubMed PMID: 22508049; PubMed Central PMCID: PMCPMC3434333.

32. Emsley JG, Macklis JD. Astroglial heterogeneity closely reflects the neuronal-defined anatomy of the adult murine CNS. Neuron glia biology. 2006;2(3):175-86. Epub 2007/03/16. doi: 10.1017/s1740925x06000202. PubMed PMID: 17356684; PubMed Central PMCID: PMCPMC1820889.

33. Vos PE, Jacobs B, Andriessen TM, Lamers KJ, Borm GF, Beems T, et al. GFAP and S100B are biomarkers of traumatic brain injury: an observational cohort study. Neurology. 2010;75(20):1786-93. Epub 2010/11/17. doi: 10.1212/WNL.0b013e3181fd62d2. PubMed PMID: 21079180.

34. Portela LV, Tort AB, Schaf DV, Ribeiro L, Nora DB, Walz R, et al. The serum S100B concentration is age dependent. Clinical chemistry. 2002;48(6 Pt 1):950-2. Epub 2002/05/25. PubMed PMID: 12029017.

35. Sorci G, Giovannini G, Riuzzi F, Bonifazi P, Zelante T, Zagarella S, et al. The danger signal S100B integrates pathogen- and danger-sensing pathways to restrain inflammation. PLoS pathogens. 2011;7(3):e1001315. Epub 2011/03/23. doi: 10.1371/journal.ppat.1001315. PubMed PMID: 21423669; PubMed Central PMCID: PMCPMC3053348.

36. Peskind ER, Griffin WS, Akama KT, Raskind MA, Van Eldik LJ. Cerebrospinal fluid S100B is elevated in the earlier stages of Alzheimer's disease. Neurochemistry international. 2001;39(5-6):409-13. Epub 2001/10/02. PubMed PMID: 11578776.

37. Harpio R, Einarsson R. S100 proteins as cancer biomarkers with focus on S100B in malignant melanoma. Clinical biochemistry. 2004;37(7):512-8. Epub 2004/07/06. doi: 10.1016/j.clinbiochem.2004.05.012. PubMed PMID: 15234232.

38. Haglid KG, Yang Q, Hamberger A, Bergman S, Widerberg A, Danielsen N. S-100beta stimulates neurite outgrowth in the rat sciatic nerve grafted with acellular muscle transplants. Brain research. 1997;753(2):196-201. Epub 1997/04/11. PubMed PMID: 9125403.

39. Harmar AJ, Marston HM, Shen S, Spratt C, West KM, Sheward WJ, et al. The VPAC(2) receptor is essential for circadian function in the mouse suprachiasmatic nuclei. Cell. 2002;109(4):497-508. Epub 2002/06/28. PubMed PMID: 12086606.

40. Noguchi T, Wang CW, Pan H, Welsh DK. Fibroblast circadian rhythms of PER2 expression depend on membrane potential and intracellular calcium. Chronobiology international. 2012;29(6):653-64. Epub 2012/06/28. doi: 10.3109/07420528.2012.679330. PubMed PMID: 22734566; PubMed Central PMCID: PMCPMC3491983.

41. Dunlap JC. Molecular bases for circadian clocks. Cell. 1999;96(2):271-90. Epub 1999/02/13. PubMed PMID: 9988221.

42. Young MW, Kay SA. Time zones: a comparative genetics of circadian clocks. Nature reviews Genetics. 2001;2(9):702-15. Epub 2001/09/05. doi: 10.1038/35088576. PubMed PMID: 11533719.

43. Crosthwaite SK, Loros JJ, Dunlap JC. Light-induced resetting of a circadian clock is mediated by a rapid increase in frequency transcript. Cell. 1995;81(7):1003-12. Epub 1995/06/30. PubMed PMID: 7600569.

44. Liu Y, Merrow M, Loros JJ, Dunlap JC. How temperature changes reset a circadian oscillator. Science (New York, NY). 1998;281(5378):825-9. Epub 1998/08/07. PubMed PMID: 9694654.

45. Stupfel M, Gourlet V, Perramon A, Merat P, Putet G, Court L. Comparison of ultradian and circadian oscillations of carbon dioxide production by various endotherms. The American journal of physiology. 1995;268(1 Pt 2):R253-65. Epub 1995/01/01. doi: 10.1152/ajpregu.1995.268.1.R253. PubMed PMID: 7840329.

46. Whittington MA, Traub RD, Faulkner HJ, Stanford IM, Jefferys JG. Recurrent excitatory postsynaptic potentials induced by synchronized fast cortical oscillations. Proceedings of the National Academy of Sciences of the United States of America. 1997;94(22):12198-203. Epub 1997/10/29. PubMed PMID: 9342386; PubMed Central PMCID: PMCPMC23749.

47. Rechtschaffen A, Kales A. A manual of standardized terminology, techniques, and scoring system for sleep stages of human subjects. Rechtschaffen A, Kales A, editors. Los Angeles: Brain Research Institute; 1968.

48. McKenna J, Zielinski M, McCarley R. Neurobiology of REM Sleep, NREM Sleep Homeostasis, and Gamma Band Oscillations. In: Chokroverty S, editor. Sleep Disorders Medicine. New York: Springer; 2017.

49. Mendelson WB, Sack DA, James SP, Martin JV, Wagner R, Garnett D, et al. Frequency analysis of the sleep EEG in depression. Psychiatry research. 1987;21(2):89-94. Epub 1987/06/01. PubMed PMID: 3615694.

50. Eiber R, Escande M. [Sleep electroencephalography in depression and mental disorders with depressive comorbidity]. L'Encephale. 1999;25(5):381-90. Epub 1999/12/22. PubMed PMID: 10598300.

51. Hartmann E. Mechanism underlying the sleep-dream cycle. Nature. 1966;212(5062):648-50. Epub 1966/11/05. PubMed PMID: 5971699.

52. Simon C, Brandenberger G. Ultradian oscillations of insulin secretion in humans. Diabetes. 2002;51 Suppl 1:S258-61. Epub 2002/01/30. PubMed PMID: 11815489.

53. Ohdo S. Chronotherapeutic strategy: Rhythm monitoring, manipulation and disruption. Advanced drug delivery reviews. 2010;62(9-10):859-75. Epub 2010/03/02. doi: 10.1016/j.addr.2010.01.006. PubMed PMID: 20188774.

54. Hayashi M, Sato K, Hori T. Ultradian rhythms in task performance, self-evaluation, and EEG activity. Perceptual and motor skills. 1994;79(2):791-800. Epub 1994/10/01. doi: 10.2466/pms.1994.79.2.791. PubMed PMID: 7870505.

55. Klein R, Armitage R. Rhythms in human performance: 1 1/2-hour oscillations in cognitive style. Science (New York, NY). 1979;204(4399):1326-8. Epub 1979/06/22. PubMed PMID: 451541.

56. Lavie P, Lord JW, Frank RA. Basic rest-activity cycle in the perception of the spiral after-effect; a sensitive detector of a basic biological rhythm. Behavioral biology. 1974;11(3):373-9. Epub 1974/07/01. PubMed PMID: 4369803.

57. Lavie P. Ultradian rhythms in alertness - a pupillometric study. Biological psychology. 1979;9(1):49-62. Epub 1979/07/01. PubMed PMID: 534670.

58. Manseau C, Broughton RJ. Bilaterally synchronous ultradian EEG rhythms in awake adult humans. Psychophysiology. 1984;21(3):265-73. Epub 1984/05/01. PubMed PMID: 6539926.

59. Rasmussen DD. Physiological interactions of the basic rest--activity cycle of the brain: pulsatile luteinizing hormone secretion as a model. Psychoneuroendocrinology. 1986;11(4):389-405. Epub 1986/01/01. PubMed PMID: 3550855.

60. Kern W, Offenheuser S, Born J, Fehm HL. Entrainment of ultradian oscillations in the secretion of insulin and glucagon to the nonrapid eye movement/rapid eye movement sleep rhythm in humans. The Journal of clinical endocrinology and metabolism. 1996;81(4):1541-7. Epub 1996/04/01. doi: 10.1210/jcem.81.4.8636364. PubMed PMID: 8636364.

61. Kleitman N. Basic rest-activity cycle--22 years later. Sleep. 1982;5(4):311-7. Epub 1982/01/01. PubMed PMID: 6819628.

62. Lewis BD, Kripke DF. Ultradian rhythms in hand-mouth behavior of the rhesus monkey. Physiology & behavior. 1977;18(2):283-6. Epub 1977/02/01. PubMed PMID: 405694.

63. Araujo JF, Marques N. Circadian and ultradian rhythms of drinking behavior of albino rats maintained in constant darkness. Brazilian journal of medical and biological research = Revista brasileira de pesquisas medicas e biologicas. 1996;29(10):1369-72. Epub 1996/10/01. PubMed PMID: 9181111.

64. Lucas EA, Harper RM. Periodicities in the rate of on-demand electrical stimulation of the mesencephalic reticular formation to maintain wakefulness. Experimental neurology. 1976;51(2):444-56. Epub 1976/05/01. PubMed PMID: 178520.

65. D'Olimpio F, Renzi P. Ultradian rhythms in young and adult mice: further support for the basic rest-activity cycle. Physiology & behavior. 1998;64(5):697-701. Epub 1998/11/17. PubMed PMID: 9817583.

66. Elgar MA, Pagel MD, Harvey PH. Sleep in mammals. Animal Behaviour. 1988;36(5):1407-19. doi: https://doi.org/10.1016/S0003-3472(88)80211-2.

67. Scannapieco E, Pasquali V, Renzi P. Circadian and ultradian motor activity rhythms under 21h and 28h lighting cycles. Biological Rhythm Research. 2009;40(4):307-16. doi: 10.1080/09291010802214716.

68. Le Bon O, Popa D, Streel E, Alexandre C, Lena C, Linkowski P, et al. Ultradian cycles in mice: definitions and links with REMS and NREMS. Journal of comparative physiology A,

Neuroethology, sensory, neural, and behavioral physiology. 2007;193(10):1021-32. Epub 2007/08/29. doi: 10.1007/s00359-007-0253-7. PubMed PMID: 17724599.

69. Bass J, Takahashi JS. Circadian rhythms: Redox redux. Nature. 2011;469(7331):476-8. Epub 2011/01/29. doi: 10.1038/469476a. PubMed PMID: 21270881; PubMed Central PMCID: PMCPMC3760156.

70. O'Neill JS, Reddy AB. Circadian clocks in human red blood cells. Nature. 2011;469(7331):498-503. Epub 2011/01/29. doi: 10.1038/nature09702. PubMed PMID: 21270888; PubMed Central PMCID: PMCPMC3040566.

71. Gronfier C, Chapotot F, Weibel L, Jouny C, Piquard F, Brandenberger G. Pulsatile cortisol secretion and EEG delta waves are controlled by two independent but synchronized generators. The American journal of physiology. 1998;275(1 Pt 1):E94-100. Epub 1998/08/05. PubMed PMID: 9688879.

72. Prast H, Grass K, Philippu A. The ultradian EEG rhythm coincides temporally with the ultradian rhythm of histamine release in the posterior hypothalamus. Naunyn-Schmiedeberg's archives of pharmacology. 1997;356(4):526-8. Epub 1998/01/24. PubMed PMID: 9349641.

73. Blum ID, Zhu L, Moquin L, Kokoeva MV, Gratton A, Giros B, et al. A highly tunable dopaminergic oscillator generates ultradian rhythms of behavioral arousal. eLife. 2014;3. Epub 2014/12/30. doi: 10.7554/eLife.05105. PubMed PMID: 25546305; PubMed Central PMCID: PMCPMC4337656.

74. van der Veen DR, Gerkema MP. Unmasking ultradian rhythms in gene expression. FASEB journal : official publication of the Federation of American Societies for Experimental Biology. 2017;31(2):743-50. Epub 2016/11/22. doi: 10.1096/fj.201600872R. PubMed PMID: 27871062; PubMed Central PMCID: PMCPMC5240665.

75. Gerkema MP, Groos GA, Daan S. Differential elimination of circadian and ultradian rhythmicity by hypothalamic lesions in the common vole, Microtus arvalis. Journal of biological rhythms. 1990;5(2):81-95. Epub 1990/01/01. doi: 10.1177/074873049000500201. PubMed PMID: 2133128.

76. Ibuka N, Inouye SI, Kawamura H. Analysis of sleep-wakefulness rhythms in male rats after suprachiasmatic nucleus lesions and ocular enucleation. Brain research. 1977;122(1):33-47. Epub 1977/02/11. PubMed PMID: 837222.

77. Naylor E, Aillon DV, Barrett BS, Wilson GS, Johnson DA, Johnson DA, et al. Lactate as a biomarker for sleep. Sleep. 2012;35(9):1209-22. Epub 2012/09/04. doi: 10.5665/sleep.2072. PubMed PMID: 22942499; PubMed Central PMCID: PMCPMC3413798.

78. Naylor E, Aillon DV, Gabbert S, Harmon H, Johnson DA, Wilson GS, et al. Simultaneous real-time measurement of EEG/EMG and L-glutamate in mice: A biosensor study of neuronal activity during sleep. Journal of electroanalytical chemistry (Lausanne, Switzerland). 2011;656(1-2):106-13. Epub 2011/06/15. doi: 10.1016/j.jelechem.2010.12.031. PubMed PMID: 27076812; PubMed Central PMCID: PMCPMC4827928.

79. Dash MB, Douglas CL, Vyazovskiy VV, Cirelli C, Tononi G. Long-term homeostasis of extracellular glutamate in the rat cerebral cortex across sleep and waking states. The Journal of neuroscience : the official journal of the Society for Neuroscience. 2009;29(3):620-9. Epub 2009/01/23. doi: 10.1523/jneurosci.5486-08.2009. PubMed PMID: 19158289; PubMed Central PMCID: PMCPMC2770705.

80. Van den Noort S, Brine K. Effect of sleep on brain labile phosphates and metabolic rate. The American journal of physiology. 1970;218(5):1434-9. Epub 1970/05/01. doi: 10.1152/ajplegacy.1970.218.5.1434. PubMed PMID: 4245209.

81. Netchiporouk L, Shram N, Salvert D, Cespuglio R. Brain extracellular glucose assessed by voltammetry throughout the rat sleep-wake cycle. The European journal of neuroscience. 2001;13(7):1429-34. Epub 2001/04/12. PubMed PMID: 11298804.

82. Dash MB, Bellesi M, Tononi G, Cirelli C. Sleep/wake dependent changes in cortical glucose concentrations. Journal of neurochemistry. 2013;124(1):79-89. Epub 2012/10/31. doi: 10.1111/jnc.12063. PubMed PMID: 23106535; PubMed Central PMCID: PMCPMC3518620.

83. Datta S, Maclean RR. Neurobiological mechanisms for the regulation of mammalian sleep-wake behavior: reinterpretation of historical evidence and inclusion of contemporary cellular and molecular evidence. Neuroscience and biobehavioral reviews. 2007;31(5):775-824. Epub 2007/04/21. doi: 10.1016/j.neubiorev.2007.02.004. PubMed PMID: 17445891; PubMed Central PMCID: PMCPMC1955686.

84. Wisor JP, Rempe MJ, Schmidt MA, Moore ME, Clegern WC. Sleep slow-wave activity regulates cerebral glycolytic metabolism. Cerebral cortex (New York, NY : 1991). 2013;23(8):1978-87. Epub 2012/07/07. doi: 10.1093/cercor/bhs189. PubMed PMID: 22767634; PubMed Central PMCID: PMCPMC3707408.

85. Dworak M, McCarley RW, Kim T, Kalinchuk AV, Basheer R. Sleep and brain energy levels: ATP changes during sleep. The Journal of neuroscience : the official journal of the Society for Neuroscience. 2010;30(26):9007-16. Epub 2010/07/02. doi: 10.1523/jneurosci.1423-10.2010. PubMed PMID: 20592221; PubMed Central PMCID: PMCPMC2917728.

86. Wong-Riley M. What is the meaning of the ATP surge during sleep? Sleep. 2011;34(7):833-4. Epub 2011/07/07. doi: 10.5665/sleep.1102. PubMed PMID: 21731129; PubMed Central PMCID: PMCPMC3119554.

87. Kadenbach B, Huttemann M, Arnold S, Lee I, Bender E. Mitochondrial energy metabolism is regulated via nuclear-coded subunits of cytochrome c oxidase. Free radical biology & medicine. 2000;29(3-4):211-21. Epub 2000/10/18. PubMed PMID: 11035249.

88. Van Twyver H. Sleep patterns of five rodent species. Physiology & behavior. 1969;4(6):901-5. doi: https://doi.org/10.1016/0031-9384(69)90038-9.

89. Hunsley MS, Palmiter RD. Norepinephrine-deficient mice exhibit normal sleep-wake states but have shorter sleep latency after mild stress and low doses of amphetamine. Sleep. 2003;26(5):521-6. Epub 2003/08/27. PubMed PMID: 12938804.

90. Lena C, Popa D, Grailhe R, Escourrou P, Changeux JP, Adrien J. Beta2-containing nicotinic receptors contribute to the organization of sleep and regulate putative micro-arousals in mice. The Journal of neuroscience : the official journal of the Society for Neuroscience. 2004;24(25):5711-8. Epub 2004/06/25. doi: 10.1523/jneurosci.3882-03.2004. PubMed PMID: 15215293.

91. Madrid-Lopez N, Estrada J, Diaz J, Bassi A, Delano PH, Ocampo-Garces A. The Sleep-Wake Cycle in the Nicotinic Alpha-9 Acetylcholine Receptor Subunit Knock-Out Mice. Frontiers in cellular neuroscience. 2017;11:302. Epub 2017/10/27. doi: 10.3389/fncel.2017.00302. PubMed PMID: 29066952; PubMed Central PMCID: PMCPMC5641320.

92. Cirelli C, Tononi G. Cortical development, electroencephalogram rhythms, and the sleep/wake cycle. Biological psychiatry. 2015;77(12):1071-8. Epub 2015/02/15. doi: 10.1016/j.biopsych.2014.12.017. PubMed PMID: 25680672; PubMed Central PMCID: PMCPMC4444390.

93. Leise TL, Harrington ME. Wavelet-based time series analysis of circadian rhythms. Journal of biological rhythms. 2011;26(5):454-63. Epub 2011/09/17. doi: 10.1177/0748730411416330. PubMed PMID: 21921299.

94. Fulda S, Romanowski CP, Becker A, Wetter TC, Kimura M, Fenzel T. Rapid eye movements during sleep in mice: high trait-like stability qualifies rapid eye movement density for characterization of phenotypic variation in sleep patterns of rodents. BMC neuroscience. 2011;12:110. Epub 2011/11/04. doi: 10.1186/1471-2202-12-110. PubMed PMID: 22047102; PubMed Central PMCID: PMCPMC3228710.

95. Krueger JM, Taishi P, De A, Davis CJ, Winters BD, Clinton J, et al. ATP and the purine type 2 X7 receptor affect sleep. Journal of applied physiology (Bethesda, Md : 1985). 2010;109(5):1318-27. Epub 2010/09/11. doi: 10.1152/japplphysiol.00586.2010. PubMed PMID: 20829501; PubMed Central PMCID: PMCPMC2980381.

96. Ferrari D, Chiozzi P, Falzoni S, Dal Susino M, Melchiorri L, Baricordi OR, et al. Extracellular ATP triggers IL-1 beta release by activating the purinergic P2Z receptor of human macrophages. Journal of immunology (Baltimore, Md : 1950). 1997;159(3):1451-8. Epub 1997/08/01. PubMed PMID: 9233643.

97. Hide I, Tanaka M, Inoue A, Nakajima K, Kohsaka S, Inoue K, et al. Extracellular ATP triggers tumor necrosis factor-alpha release from rat microglia. Journal of neurochemistry. 2000;75(3):965-72. Epub 2000/08/11. PubMed PMID: 10936177.

98. Krueger JM, Walter J, Dinarello CA, Wolff SM, Chedid L. Sleep-promoting effects of endogenous pyrogen (interleukin-1). The American journal of physiology. 1984;246(6 Pt 2):R994-9. Epub 1984/06/01. doi: 10.1152/ajpregu.1984.246.6.R994. PubMed PMID: 6611091.

99. Shoham S, Davenne D, Cady AB, Dinarello CA, Krueger JM. Recombinant tumor necrosis factor and interleukin 1 enhance slow-wave sleep. The American journal of physiology. 1987;253(1 Pt 2):R142-9. Epub 1987/07/01. doi: 10.1152/ajpregu.1987.253.1.R142. PubMed PMID: 3496800.

100. Kovalzon VM, Moiseenko LS, Ambaryan AV, Kurtenbach S, Shestopalov VI, Panchin YV. Sleep-wakefulness cycle and behavior in pannexin1 knockout mice. Behavioural brain research. 2017;318:24-7. Epub 2016/10/30. doi: 10.1016/j.bbr.2016.10.015. PubMed PMID: 27769744.

101. Lundberg JM. Pharmacology of cotransmission in the autonomic nervous system: integrative aspects on amines, neuropeptides, adenosine triphosphate, amino acids and nitric oxide. Pharmacological reviews. 1996;48(1):113-78. Epub 1996/03/01. PubMed PMID: 8685245.

102. Kupfermann I. Functional studies of cotransmission. Physiological reviews. 1991;71(3):683-732. Epub 1991/07/01. doi: 10.1152/physrev.1991.71.3.683. PubMed PMID: 1647537.

103. Feldberg W, Sherwood SL. Intraventricular injections of acetylcholine and of 5-hydroxytryptamine (serotonin) into the conscious cat. The Journal of physiology. 1953;120(1-2):12p. Epub 1953/04/28. PubMed PMID: 13062248.

104. Dunwiddie TV, Worth T. Sedative and anticonvulsant effects of adenosine analogs in mouse and rat. The Journal of pharmacology and experimental therapeutics. 1982;220(1):70-6. Epub 1982/01/01. PubMed PMID: 7053424.

105. Radulovacki M, Virus RM, Djuricic-Nedelson M, Green RD. Adenosine analogs and sleep in rats. The Journal of pharmacology and experimental therapeutics. 1984;228(2):268-74. Epub 1984/02/01. PubMed PMID: 6694111.

106. Martin JV, Berman KF, Skolnick P, Mendelson WB. Behavioral and electroencephalographic effects of the adenosine1 agonist, L-PIA. Pharmacology, biochemistry, and behavior. 1989;34(3):507-10. Epub 1989/11/01. PubMed PMID: 2623008.

107. Fredholm BB, Battig K, Holmen J, Nehlig A, Zvartau EE. Actions of caffeine in the brain with special reference to factors that contribute to its widespread use. Pharmacological reviews. 1999;51(1):83-133. Epub 1999/03/02. PubMed PMID: 10049999.

108. Landolt HP, Dijk DJ, Gaus SE, Borbely AA. Caffeine reduces low-frequency delta activity in the human sleep EEG. Neuropsychopharmacology : official publication of the American College of Neuropsychopharmacology. 1995;12(3):229-38. Epub 1995/05/01. doi: 10.1016/0893-133x(94)00079-f. PubMed PMID: 7612156.

109. Porkka-Heiskanen T, Strecker RE, McCarley RW. Brain site-specificity of extracellular adenosine concentration changes during sleep deprivation and spontaneous sleep: an in vivo microdialysis study. Neuroscience. 2000;99(3):507-17. Epub 2000/10/13. PubMed PMID: 11029542.

110. Porkka-Heiskanen T, Strecker RE, Thakkar M, Bjorkum AA, Greene RW, McCarley RW. Adenosine: a mediator of the sleep-inducing effects of prolonged wakefulness. Science (New York, NY). 1997;276(5316):1265-8. Epub 1997/05/23. PubMed PMID: 9157887; PubMed Central PMCID: PMCPMC3599777.

111. Jacobson KA, Costanzi S, Kim SK, Roh E, Joshi BV, Tchilibon S, et al. Action of nucleosides and nucleotides at 7 transmembrane-spanning receptors. Nucleosides, nucleotides & nucleic acids. 2006;25(12):1425-36. Epub 2006/10/28. doi: 10.1080/15257770600919027. PubMed PMID: 17067963.

112. Zimmermann H, Zebisch M, Strater N. Cellular function and molecular structure of ecto-nucleotidases. Purinergic signalling. 2012;8(3):437-502. Epub 2012/05/05. doi: 10.1007/s11302-012-9309-4. PubMed PMID: 22555564; PubMed Central PMCID: PMCPMC3360096.

113. Zielinski MR, Taishi P, Clinton JM, Krueger JM. 5'-Ectonucleotidase-knockout mice lack non-REM sleep responses to sleep deprivation. The European journal of neuroscience. 2012;35(11):1789-98. Epub 2012/05/01. doi: 10.1111/j.1460-9568.2012.08112.x. PubMed PMID: 22540145; PubMed Central PMCID: PMCPMC3370120.

114. Meerlo P, Easton A, Bergmann BM, Turek FW. Restraint increases prolactin and REM sleep in C57BL/6J mice but not in BALB/cJ mice. American journal of physiology Regulatory, integrative and comparative physiology. 2001;281(3):R846-54. Epub 2001/08/17. doi: 10.1152/ajpregu.2001.281.3.R846. PubMed PMID: 11507000.

115. Fedele DE, Gouder N, Guttinger M, Gabernet L, Scheurer L, Rulicke T, et al. Astrogliosis in epilepsy leads to overexpression of adenosine kinase, resulting in seizure aggravation. Brain : a journal of neurology. 2005;128(Pt 10):2383-95. Epub 2005/06/03. doi: 10.1093/brain/awh555. PubMed PMID: 15930047.

116. Palchykova S, Winsky-Sommerer R, Shen HY, Boison D, Gerling A, Tobler I. Manipulation of adenosine kinase affects sleep regulation in mice. The Journal of neuroscience : the official journal of the Society for Neuroscience. 2010;30(39):13157-65. Epub 2010/10/01. doi: 10.1523/jneurosci.1359-10.2010. PubMed PMID: 20881134; PubMed Central PMCID: PMCPMC2950004.

117. Satoh S, Matsumura H, Suzuki F, Hayaishi O. Promotion of sleep mediated by the A2a-adenosine receptor and possible involvement of this receptor in the sleep induced by prostaglandin D2 in rats. Proceedings of the National Academy of Sciences of the United States of America. 1996;93(12):5980-4. Epub 1996/06/11. PubMed PMID: 8650205; PubMed Central PMCID: PMCPMC39174.

118. Benington JH, Kodali SK, Heller HC. Stimulation of A1 adenosine receptors mimics the electroencephalographic effects of sleep deprivation. Brain research. 1995;692(1-2):79-85. Epub 1995/09/18. PubMed PMID: 8548323.

119. Zylka MJ, Sowa NA, Taylor-Blake B, Twomey MA, Herrala A, Voikar V, et al. Prostatic acid phosphatase is an ectonucleotidase and suppresses pain by generating adenosine. Neuron.

2008;60(1):111-22. Epub 2008/10/23. doi: 10.1016/j.neuron.2008.08.024. PubMed PMID: 18940592; PubMed Central PMCID: PMCPMC2629077.

120. Street SE, Walsh PL, Sowa NA, Taylor-Blake B, Guillot TS, Vihko P, et al. PAP and NT5E inhibit nociceptive neurotransmission by rapidly hydrolyzing nucleotides to adenosine. Molecular pain. 2011;7:80. Epub 2011/10/21. doi: 10.1186/1744-8069-7-80. PubMed PMID: 22011440; PubMed Central PMCID: PMCPMC3210096.

121. Quintero IB, Araujo CL, Pulkka AE, Wirkkala RS, Herrala AM, Eskelinen EL, et al. Prostatic acid phosphatase is not a prostate specific target. Cancer research. 2007;67(14):6549-54. Epub 2007/07/20. doi: 10.1158/0008-5472.can-07-1651. PubMed PMID: 17638863.

122. Klyuch BP, Dale N, Wall MJ. Deletion of ecto-5'-nucleotidase (CD73) reveals direct action potential-dependent adenosine release. The Journal of neuroscience : the official journal of the Society for Neuroscience. 2012;32(11):3842-7. Epub 2012/03/17. doi: 10.1523/jneurosci.6052-11.2012. PubMed PMID: 22423104.

123. Baldwin SA, Beal PR, Yao SY, King AE, Cass CE, Young JD. The equilibrative nucleoside transporter family, SLC29. Pflugers Archiv : European journal of physiology. 2004;447(5):735-43. Epub 2003/07/03. doi: 10.1007/s00424-003-1103-2. PubMed PMID: 12838422.

124. Rittiner JE, Korboukh I, Hull-Ryde EA, Jin J, Janzen WP, Frye SV, et al. AMP is an adenosine A1 receptor agonist. The Journal of biological chemistry. 2012;287(8):5301-9. Epub 2012/01/05. doi: 10.1074/jbc.M111.291666. PubMed PMID: 22215671; PubMed Central PMCID: PMCPMC3285310.

125. James TD, Moffett SX, Scanlan TS, Martin JV. Effects of acute microinjections of the thyroid hormone derivative 3-iodothyronamine to the preoptic region of adult male rats on sleep, thermoregulation and motor activity. Hormones and behavior. 2013;64(1):81-8. doi: 10.1016/j.yhbeh.2013.05.004. PubMed PMID: PMC4091812.

126. Demet MM, Ozmen B, Deveci A, Boyvada S, Adiguzel H, Aydemir O. Depression and anxiety in hyperthyroidism. Archives of medical research. 2002;33(6):552-6. Epub 2002/12/31. PubMed PMID: 12505101.

127. Watt T, Groenvold M, Rasmussen AK, Bonnema SJ, Hegedus L, Bjorner JB, et al. Quality of life in patients with benign thyroid disorders. A review. European journal of endocrinology. 2006;154(4):501-10. Epub 2006/03/25. doi: 10.1530/eje.1.02124. PubMed PMID: 16556711.

128. Whybrow, Bauer. Behavioral and psychiatric aspects of hypothyroidism. Braverman LE UR, editor. Philadelphia: Lippincott Williams and Wilkins; 2005.

129. Whybrow, Bauer. Behavioral and psychiatric aspects of thyrotoxicosis. Braverman LE UR, editor. Philadelphia: Lippincott Williams and Wilkins; 2005.

130. Browning TB, Atkins RW, Weiner H. Cerebral metabolic disturbances in hypothyroidism; clinical and electroencephalographic studies of the psychosis of myxedema and hypothyroidism.

AMA archives of internal medicine. 1954;93(6):938-50. Epub 1954/06/01. PubMed PMID: 13157681.

131. Carpenter AC, Timiras PS. Sleep organization in hypo- and hyperthyroid rats. Neuroendocrinology. 1982;34(6):438-43. Epub 1982/06/01. doi: 10.1159/000123342. PubMed PMID: 7201573.

132. Eastman CI, Rechtschaffen A. Effect of thyroxine on sleep in the rat. Sleep. 1979;2(2):215-32. Epub 1979/01/01. PubMed PMID: 232566.

133. Kales A, Heuser G, Jacobson A, Kales JD, Hanley J, Zweizig JR, et al. All night sleep studies in hypothyroid patients, before and after treatment. The Journal of clinical endocrinology and metabolism. 1967;27(11):1593-9. Epub 1967/11/01. doi: 10.1210/jcem-27-11-1593. PubMed PMID: 6075589.

134. Scanlan TS, Suchland KL, Hart ME, Chiellini G, Huang Y, Kruzich PJ, et al. 3-Iodothyronamine is an endogenous and rapid-acting derivative of thyroid hormone. Nature medicine. 2004;10(6):638-42. Epub 2004/05/18. doi: 10.1038/nm1051. PubMed PMID: 15146179.

135. Dratman MB, Crutchfield FL. Synaptosomal [125I]triiodothyronine after intravenous [125I]thyroxine. The American journal of physiology. 1978;235(6):E638-47. Epub 1978/12/01. doi: 10.1152/ajpendo.1978.235.6.E638. PubMed PMID: 736123.

136. Dratman MB, Crutchfield FL, Axelrod J, Colburn RW, Thoa N. Localization of triiodothyronine in nerve ending fractions of rat brain. Proceedings of the National Academy of Sciences of the United States of America. 1976;73(3):941-4. Epub 1976/03/01. PubMed PMID: 1062808; PubMed Central PMCID: PMCPMC336036.

137. Dratman MB, Futaesaku Y, Crutchfield FL, Berman N, Payne B, Sar M, et al. Iodine-125-labeled triiodothyronine in rat brain: evidence for localization in discrete neural systems. Science (New York, NY). 1982;215(4530):309-12. Epub 1982/01/15. PubMed PMID: 7053582.

138. Gordon JT, Kaminski DM, Rozanov CB, Dratman MB. Evidence that 3,3',5-triiodothyronine is concentrated in and delivered from the locus coeruleus to its noradrenergic targets via anterograde axonal transport. Neuroscience. 1999;93(3):943-54. Epub 1999/09/03. PubMed PMID: 10473259.

139. Rozanov CB, Dratman MB. Immunohistochemical mapping of brain triiodothyronine reveals prominent localization in central noradrenergic systems. Neuroscience. 1996;74(3):897-915. Epub 1996/10/01. PubMed PMID: 8884785.

140. Berry MD. Mammalian central nervous system trace amines. Pharmacologic amphetamines, physiologic neuromodulators. Journal of neurochemistry. 2004;90(2):257-71. Epub 2004/07/02. doi: 10.1111/j.1471-4159.2004.02501.x. PubMed PMID: 15228583.

141. Dratman MB. On the mechanism of action of thyroxin, an amino acid analog of tyrosine. Journal of theoretical biology. 1974;46(1):255-70. Epub 1974/07/01. PubMed PMID: 4152982.

142. Piehl S, Heberer T, Balizs G, Scanlan TS, Smits R, Koksch B, et al. Thyronamines are isozyme-specific substrates of deiodinases. Endocrinology. 2008;149(6):3037-45. Epub 2008/03/15. doi: 10.1210/en.2007-1678. PubMed PMID: 18339710; PubMed Central PMCID: PMCPMC2734495.

143. Campos-Barros A, Musa A, Flechner A, Hessenius C, Gaio U, Meinhold H, et al. Evidence for circadian variations of thyroid hormone concentrations and type II 5'-iodothyronine deiodinase activity in the rat central nervous system. Journal of neurochemistry. 1997;68(2):795-803. Epub 1997/02/01. PubMed PMID: 9003071.

144. Rall JE, Rawson RW, Tata JR. Metabolism of L-thyroxine and L-3:5:3'-triiodothyronine by brain tissue preparations. Endocrinology. 1957;60(1):83-98. Epub 1957/01/01. doi: 10.1210/endo-60-1-83. PubMed PMID: 13384387.

145. Hoefig CS, Renko K, Piehl S, Scanlan TS, Bertoldi M, Opladen T, et al. Does the aromatic L-amino acid decarboxylase contribute to thyronamine biosynthesis? Molecular and cellular endocrinology. 2012;349(2):195-201. Epub 2011/11/09. doi: 10.1016/j.mce.2011.10.024. PubMed PMID: 22061622.

146. Hackenmueller SA, Marchini M, Saba A, Zucchi R, Scanlan TS. Biosynthesis of 3-iodothyronamine (T1AM) is dependent on the sodium-iodide symporter and thyroperoxidase but does not involve extrathyroidal metabolism of T4. Endocrinology. 2012;153(11):5659-67. Epub 2012/09/06. doi: 10.1210/en.2012-1254. PubMed PMID: 22948220; PubMed Central PMCID: PMCPMC3473208.

147. Koury EJ, Pawlyk AC, Berrodin TJ, Smolenski CL, Nagpal S, Deecher DC. Characterization of ligands for thyroid receptor subtypes and their interactions with co-regulators. Steroids. 2009;74(2):270-6. Epub 2008/12/17. doi: 10.1016/j.steroids.2008.11.014. PubMed PMID: 19073200.

148. Regard JB, Kataoka H, Cano DA, Camerer E, Yin L, Zheng YW, et al. Probing cell type-specific functions of Gi in vivo identifies GPCR regulators of insulin secretion. The Journal of clinical investigation. 2007;117(12):4034-43. Epub 2007/11/10. doi: 10.1172/jci32994. PubMed PMID: 17992256; PubMed Central PMCID: PMCPMC2066199.

149. Bucheler MM, Hadamek K, Hein L. Two alpha(2)-adrenergic receptor subtypes, alpha(2A) and alpha(2C), inhibit transmitter release in the brain of gene-targeted mice. Neuroscience. 2002;109(4):819-26. Epub 2002/04/03. PubMed PMID: 11927164.

150. Lindemann L, Meyer CA, Jeanneau K, Bradaia A, Ozmen L, Bluethmann H, et al. Trace amine-associated receptor 1 modulates dopaminergic activity. The Journal of pharmacology and experimental therapeutics. 2008;324(3):948-56. Epub 2007/12/18. doi: 10.1124/jpet.107.132647. PubMed PMID: 18083911.

151. Modirrousta M, Mainville L, Jones BE. Gabaergic neurons with alpha2-adrenergic receptors in basal forebrain and preoptic area express c-Fos during sleep. Neuroscience.

2004;129(3):803-10. Epub 2004/11/16. doi: 10.1016/j.neuroscience.2004.07.028. PubMed PMID: 15541901.

152. Chapell R, Martin J, Machu TK, Leidenheimer NJ. Direct channel-gating and modulatory effects of triiodothyronine on recombinant GABA(A) receptors. European journal of pharmacology. 1998;349(1):115-21. Epub 1998/07/21. PubMed PMID: 9669504.

153. Dratman MB, Gordon JT. Thyroid hormones as neurotransmitters. Thyroid : official journal of the American Thyroid Association. 1996;6(6):639-47. Epub 1996/12/01. doi: 10.1089/thy.1996.6.639. PubMed PMID: 9001201.

154. Martin JV, Williams DB, Fitzgerald RM, Im HK, Vonvoigtlander PF. Thyroid hormonal modulation of the binding and activity of the GABAA receptor complex of brain. Neuroscience. 1996;73(3):705-13. Epub 1996/08/01. PubMed PMID: 8809792.

155. Sarkar PK, Durga ND, Morris JJ, Martin JV. In vitro thyroid hormone rapidly modulates protein phosphorylation in cerebrocortical synaptosomes from adult rat brain. Neuroscience. 2006;137(1):125-32. Epub 2005/11/18. doi: 10.1016/j.neuroscience.2005.10.002. PubMed PMID: 16289831.

156. Sarkar PK, Morris JJ, Martin JV. Non-genomic effect of L-triiodothyronine on calmodulin-dependent synaptosomal protein phosphorylation in adult rat cerebral cortex. Indian journal of experimental biology. 2011;49(3):169-76. Epub 2011/04/02. PubMed PMID: 21452595.

157. Snead AN, Santos MS, Seal RP, Miyakawa M, Edwards RH, Scanlan TS. Thyronamines inhibit plasma membrane and vesicular monoamine transport. ACS chemical biology. 2007;2(6):390-8. Epub 2007/05/29. doi: 10.1021/cb700057b. PubMed PMID: 17530732.

158. Dhillo WS, Bewick GA, White NE, Gardiner JV, Thompson EL, Bataveljic A, et al. The thyroid hormone derivative 3-iodothyronamine increases food intake in rodents. Diabetes, obesity & metabolism. 2009;11(3):251-60. Epub 2008/08/02. doi: 10.1111/j.1463-1326.2008.00935.x. PubMed PMID: 18671794.

159. Emlen W, Segal DS, Mandell AJ. Thyroid state: effects on pre- and postsynaptic central noradrenergic mechanisms. Science (New York, NY). 1972;175(4017):79-82. Epub 1972/01/07. PubMed PMID: 4400216.

160. Caria MA, Dratman MB, Kow LM, Mameli O, Pavlides C. Thyroid hormone action: nongenomic modulation of neuronal excitability in the hippocampus. Journal of neuroendocrinology. 2009;21(2):98-107. Epub 2008/12/17. doi: 10.1111/j.1365-2826.2008.01813.x. PubMed PMID: 19076268.

161. Gompf HS, Greenberg JH, Aston-Jones G, Ianculescu AG, Scanlan TS, Dratman MB. 3-Monoiodothyronamine: the rationale for its action as an endogenous adrenergic-blocking neuromodulator. Brain research. 2010;1351:130-40. Epub 2010/07/10. doi: 10.1016/j.brainres.2010.06.067. PubMed PMID: 20615397; PubMed Central PMCID: PMCPMC2926234.

162. Mohan Kumar V, Datta S, Chhina GS, Singh B. Alpha adrenergic system in medial preoptic area involved in sleep-wakefulness in rats. Brain research bulletin. 1986;16(4):463-8. Epub 1986/04/01. PubMed PMID: 3013378.

163. Ramesh V, Kumar VM. The role of alpha-2 receptors in the medial preoptic area in the regulation of sleep-wakefulness and body temperature. Neuroscience. 1998;85(3):807-17. Epub 1998/06/25. PubMed PMID: 9639274.

164. Ramesh V, Kumar VM, John J, Mallick H. Medial preoptic alpha-2 adrenoceptors in the regulation of sleep-wakefulness. Physiology & behavior. 1995;57(1):171-5. Epub 1995/01/01. PubMed PMID: 7878113.

165. Gong H, Szymusiak R, King J, Steininger T, McGinty D. Sleep-related c-Fos protein expression in the preoptic hypothalamus: effects of ambient warming. American journal of physiology Regulatory, integrative and comparative physiology. 2000;279(6):R2079-88. Epub 2000/11/18. doi: 10.1152/ajpregu.2000.279.6.R2079. PubMed PMID: 11080072.

166. Gvilia I, Xu F, McGinty D, Szymusiak R. Homeostatic regulation of sleep: a role for preoptic area neurons. The Journal of neuroscience : the official journal of the Society for Neuroscience. 2006;26(37):9426-33. Epub 2006/09/15. doi: 10.1523/jneurosci.2012-06.2006. PubMed PMID: 16971526.

167. McGinty DJ, Sterman MB. Sleep suppression after basal forebrain lesions in the cat. Science (New York, NY). 1968;160(3833):1253-5. Epub 1968/06/14. PubMed PMID: 5689683.

168. Sterman MB, Clemente CD. Basal forebrain structures and sleep. Acta neurologica latinoamericana. 1968;14(1):228-44. Epub 1968/01/01. PubMed PMID: 4918111.

169. Suntsova N, Szymusiak R, Alam MN, Guzman-Marin R, McGinty D. Sleep-waking discharge patterns of median preoptic nucleus neurons in rats. The Journal of physiology. 2002;543(Pt 2):665-77. Epub 2002/09/03. PubMed PMID: 12205198; PubMed Central PMCID: PMCPMC2290500.

170. Martin JV, Cook JM, Hagen TJ, Mendelson WB. Inhibition of sleep and benzodiazepine receptor binding by a beta-carboline derivative. Pharmacology, biochemistry, and behavior. 1989;34(1):37-42. Epub 1989/09/01. PubMed PMID: 2560549.

171. kruger, saporta, swanson. Photographic atlas of the rat brain: the cell and fiber architecture illustrated in three planes with stereotaxic coordinates. Cambridge; New York: Cambridge University Press; 1995.

172. Lohman RJ, Liu L, Morris M, O'Brien TJ. Validation of a method for localised microinjection of drugs into thalamic subregions in rats for epilepsy pharmacological studies. Journal of neuroscience methods. 2005;146(2):191-7. Epub 2005/08/02. doi: 10.1016/j.jneumeth.2005.02.008. PubMed PMID: 16054509.

173. Martin JV, Giannopoulos PF, Moffett SX, James TD. Effects of acute microinjections of thyroid hormone to the preoptic region of euthyroid adult male rats on sleep and motor activity.

Brain research. 2013;1516:45-54. Epub 2013/01/26. doi: 10.1016/j.brainres.2013.01.032. PubMed PMID: 23348377.

174. Moffett SX, Giannopoulos PF, James TD, Martin JV. Effects of acute microinjections of thyroid hormone to the preoptic region of hypothyroid adult male rats on sleep, motor activity and body temperature. Brain research. 2013;1516:55-65. Epub 2013/04/23. doi: 10.1016/j.brainres.2013.04.017. PubMed PMID: 23603414.

175. Glick SD, Muller RU. Paradoxical effects of low doses of d-amphetamine in rats. Psychopharmacologia. 1971;22(4):396-402. Epub 1971/01/01. PubMed PMID: 5133440.

176. Day TA, Willoughby JO, Geffen LB. Thermoregulatory effects of preoptic area injections of noradrenaline in restrained and unrestrained rats. Brain research. 1979;174(1):175-9. Epub 1979/09/28. PubMed PMID: 573655.

177. Panas HN, Lynch LJ, Vallender EJ, Xie Z, Chen GL, Lynn SK, et al. Normal thermoregulatory responses to 3-iodothyronamine, trace amines and amphetamine-like psychostimulants in trace amine associated receptor 1 knockout mice. Journal of neuroscience research. 2010;88(9):1962-9. Epub 2010/02/16. doi: 10.1002/jnr.22367. PubMed PMID: 20155805; PubMed Central PMCID: PMCPMC3587846.

178. McGinty D, Szymusiak R. Keeping cool: a hypothesis about the mechanisms and functions of slow-wave sleep. Trends in neurosciences. 1990;13(12):480-7. Epub 1990/12/01. PubMed PMID: 1703678.

179. Satinoff E. BEHAVIORAL THERMOREGULATION IN RESPONSE TO LOCAL COOLING OF THE RAT BRAIN. The American journal of physiology. 1964;206:1389-94. Epub 1964/06/01. doi: 10.1152/ajplegacy.1964.206.6.1389. PubMed PMID: 14193560.

180. Zhang YH, Yanase-Fujiwara M, Hosono T, Kanosue K. Warm and cold signals from the preoptic area: which contribute more to the control of shivering in rats? The Journal of physiology. 1995;485 (Pt 1):195-202. Epub 1995/05/15. PubMed PMID: 7658373; PubMed Central PMCID: PMCPMC1157983.

181. Roberts WW, Robinson TC. Relaxation and sleep induced by warming of preoptic region and anterior hypothalamus in cats. Experimental neurology. 1969;25(2):282-94. Epub 1969/10/01. PubMed PMID: 5345014.

182. Travis KA, Johnson AK. In vitro sensitivity of median preoptic neurons to angiotensin II, osmotic pressure, and temperature. The American journal of physiology. 1993;264(6 Pt 2):R1200-5. Epub 1993/06/01. doi: 10.1152/ajpregu.1993.264.6.R1200. PubMed PMID: 8322974.

183. Mendelson WB, Martin JV. Characterization of the hypnotic effects of triazolam microinjections into the medial preoptic area. Life sciences. 1992;50(15):1117-28. Epub 1992/01/01. PubMed PMID: 1556906.

184. Mendelson WB, Martin JV, Perlis M, Wagner R. Enhancement of sleep by microinjection of triazolam into the medial preoptic area. Neuropsychopharmacology : official publication of the American College of Neuropsychopharmacology. 1989;2(1):61-6. Epub 1989/03/01. PubMed PMID: 2803481.

185. Moffett SX, O'Malley SM, Man S, Hong D, Martin JV. Dynamics of high frequency brain activity. Scientific reports. 2017;7:15758. doi: 10.1038/s41598-017-15966-6. PubMed PMID: PMC5693956.

186. Groppe DM, Bickel S, Keller CJ, Jain SK, Hwang ST, Harden C, et al. Dominant frequencies of resting human brain activity as measured by the electrocorticogram. NeuroImage. 2013;79:223-33. Epub 2013/05/04. doi: 10.1016/j.neuroimage.2013.04.044. PubMed PMID: 23639261; PubMed Central PMCID: PMCPMC4269223.

187. Buzsaki G. Rhythms of the Brain: Oxford University Press; 2006.

188. Klostermann F, Gobbele R, Buchner H, Curio G. Intrathalamic non-propagating generators of high-frequency (1000 Hz) somatosensory evoked potential (SEP) bursts recorded subcortically in man. Clinical neurophysiology : official journal of the International Federation of Clinical Neurophysiology. 2002;113(7):1001-5. Epub 2002/06/29. PubMed PMID: 12088692.

189. Jones MS, MacDonald KD, Choi B, Dudek FE, Barth DS. Intracellular correlates of fast (>200 Hz) electrical oscillations in rat somatosensory cortex. Journal of neurophysiology. 2000;84(3):1505-18. Epub 2000/09/09. doi: 10.1152/jn.2000.84.3.1505. PubMed PMID: 10980023.

190. Kandel A, Buzsaki G. Cellular-synaptic generation of sleep spindles, spike-and-wave discharges, and evoked thalamocortical responses in the neocortex of the rat. The Journal of neuroscience : the official journal of the Society for Neuroscience. 1997;17(17):6783-97. Epub 1997/09/01. PubMed PMID: 9254689.

191. Engel J, Jr., Bragin A, Staba R, Mody I. High-frequency oscillations: what is normal and what is not? Epilepsia. 2009;50(4):598-604. Epub 2008/12/06. doi: 10.1111/j.1528-1167.2008.01917.x. PubMed PMID: 19055491.

192. Hong D, Man S, Martin JV. A stochastic mechanism for signal propagation in the brain: Force of rapid random fluctuations in membrane potentials of individual neurons. Journal of theoretical biology. 2016;389:225-36. Epub 2015/11/12. doi: 10.1016/j.jtbi.2015.10.035. PubMed PMID: 26555846.

193. Grigolini P, Aquino G, Bologna M, Luković M, West BJ. A theory of 1/f noise in human cognition. Physica A: Statistical Mechanics and its Applications. 2009;388(19):4192-204. doi: https://doi.org/10.1016/j.physa.2009.06.024.

194. He BJ. Scale-free brain activity: past, present, and future. Trends in cognitive sciences. 2014;18(9):480-7. Epub 2014/05/03. doi: 10.1016/j.tics.2014.04.003. PubMed PMID: 24788139; PubMed Central PMCID: PMCPMC4149861.

195. Kamitani Y, Matsuba I, editors. Neural networks in three dimensions producing 1/f spectra. 8th International Conference on Neural Information Processing; 2001.

196. Pereda E, Gamundi A, Rial R, Gonzalez J. Non-linear behaviour of human EEG: fractal exponent versus correlation dimension in awake and sleep stages. Neuroscience letters. 1998;250(2):91-4. Epub 1998/08/11. PubMed PMID: 9697926.

197. Pritchard WS. The brain in fractal time: 1/f-like power spectrum scaling of the human electroencephalogram. The International journal of neuroscience. 1992;66(1-2):119-29. Epub 1992/09/01. PubMed PMID: 1304564.

198. Voytek B, Kramer MA, Case J, Lepage KQ, Tempesta ZR, Knight RT, et al. Age-Related Changes in 1/f Neural Electrophysiological Noise. The Journal of neuroscience : the official journal of the Society for Neuroscience. 2015;35(38):13257-65. Epub 2015/09/25. doi: 10.1523/jneurosci.2332-14.2015. PubMed PMID: 26400953; PubMed Central PMCID: PMCPMC4579381.

199. Clay JR, Shlesinger MF. Theoretical model of the ionic mechanism of 1/f noise in nerve membrane. Biophysical journal. 1976;16(2 Pt 1):121-36. Epub 1976/02/01. PubMed PMID: 1247642; PubMed Central PMCID: PMCPMC1334823.

200. Siwy Z, Fulinski A. Origin of 1/f(alpha) noise in membrane channel currents. Physical review letters. 2002;89(15):158101. Epub 2002/10/09. doi: 10.1103/PhysRevLett.89.158101. PubMed PMID: 12366027.

201. Pettersen KH, Linden H, Tetzlaff T, Einevoll GT. Power laws from linear neuronal cable theory: power spectral densities of the soma potential, soma membrane current and single-neuron contribution to the EEG. PLoS computational biology. 2014;10(11):e1003928. Epub 2014/11/14. doi: 10.1371/journal.pcbi.1003928. PubMed PMID: 25393030; PubMed Central PMCID: PMCPMC4230751.

202. Linkenkaer-Hansen K, Nikouline VV, Palva JM, Ilmoniemi RJ. Long-range temporal correlations and scaling behavior in human brain oscillations. The Journal of neuroscience : the official journal of the Society for Neuroscience. 2001;21(4):1370-7. Epub 2001/02/13. PubMed PMID: 11160408.

203. Buzsaki G, Mizuseki K. The log-dynamic brain: how skewed distributions affect network operations. Nature reviews Neuroscience. 2014;15(4):264-78. Epub 2014/02/27. doi: 10.1038/nrn3687. PubMed PMID: 24569488; PubMed Central PMCID: PMCPMC4051294.

204. Mandelbrot BB, Ness JWV. Fractional Brownian Motions, Fractional Noises and Applications. 1968;10(4):422-37. doi: 10.1137/1010093.

205. Mishura Y. Stochastic Calculus for Fractional Brownian Motion and Related Processes: Springer; 2007.

206. Clarke PB, Schwartz RD, Paul SM, Pert CB, Pert A. Nicotinic binding in rat brain: autoradiographic comparison of [3H]acetylcholine, [3H]nicotine, and [125I]-alpha-bungarotoxin.

The Journal of neuroscience : the official journal of the Society for Neuroscience. 1985;5(5):1307-15. Epub 1985/05/01. PubMed PMID: 3998824.

207. Hucho F. The nicotinic acetylcholine receptor and its ion channel. European journal of biochemistry. 1986;158(2):211-26. Epub 1986/07/15. PubMed PMID: 2426106.

208. Steinlein OK, Bertrand D. Nicotinic receptor channelopathies and epilepsy. Pflugers Archiv : European journal of physiology. 2010;460(2):495-503. Epub 2009/12/18. doi: 10.1007/s00424-009-0766-8. PubMed PMID: 20016990.

209. Fambrough DM, Drachman DB, Satyamurti S. Neuromuscular junction in myasthenia gravis: decreased acetylcholine receptors. Science (New York, NY). 1973;182(4109):293-5. Epub 1973/10/19. PubMed PMID: 4742736.

210. Drachman DB, Angus CW, Adams RN, Michelson JD, Hoffman GJ. Myasthenic antibodies cross-link acetylcholine receptors to accelerate degradation. The New England journal of medicine. 1978;298(20):1116-22. Epub 1978/05/18. doi: 10.1056/nejm197805182982004. PubMed PMID: 643030.

211. Sine SM, Engel AG. Recent advances in Cys-loop receptor structure and function. Nature. 2006;440(7083):448-55. Epub 2006/03/24. doi: 10.1038/nature04708. PubMed PMID: 16554804.

212. Miyazawa A, Fujiyoshi Y, Unwin N. Structure and gating mechanism of the acetylcholine receptor pore. Nature. 2003;423(6943):949-55. Epub 2003/06/27. doi: 10.1038/nature01748. PubMed PMID: 12827192.

213. Uki M, Nabekura J, Akaike N. Suppression of the nicotinic acetylcholine response in rat superior cervical ganglionic neurons by steroids. Journal of neurochemistry. 1999;72(2):808-14. Epub 1999/02/04. PubMed PMID: 9930757.

214. Wang M. Neurosteroids and GABA-A Receptor Function. Frontiers in endocrinology. 2011;2:44. Epub 2011/01/01. doi: 10.3389/fendo.2011.00044. PubMed PMID: 22654809; PubMed Central PMCID: PMCPMC3356040.

215. Westergard T, Salari R, Martin JV, Brannigan G. Interactions of L-3,5,3'-Triiodothyronine [corrected], Allopregnanolone, and Ivermectin with the GABAA Receptor: Evidence for Overlapping Intersubunit Binding Modes. PloS one. 2015;10(9):e0139072. Epub 2015/10/01. doi: 10.1371/journal.pone.0139072. PubMed PMID: 26421724; PubMed Central PMCID: PMCPMC4589331.

216. Majewska MD. Neurosteroids: endogenous bimodal modulators of the GABAA receptor. Mechanism of action and physiological significance. Progress in neurobiology. 1992;38(4):379-95. Epub 1992/01/01. PubMed PMID: 1349441.

217. Majewska MD, Harrison NL, Schwartz RD, Barker JL, Paul SM. Steroid hormone metabolites are barbiturate-like modulators of the GABA receptor. Science (New York, NY). 1986;232(4753):1004-7. Epub 1986/05/23. PubMed PMID: 2422758.

218. Callachan H, Cottrell GA, Hather NY, Lambert JJ, Nooney JM, Peters JA. Modulation of the GABAA receptor by progesterone metabolites. Proceedings of the Royal Society of London Series B, Biological sciences. 1987;231(1264):359-69. Epub 1987/08/21. PubMed PMID: 2888123.

219. Martin JV, Padron JM, Newman MA, Chapell R, Leidenheimer NJ, Burke LA. Inhibition of the activity of the native gamma-aminobutyric acid A receptor by metabolites of thyroid hormones: correlations with molecular modeling studies. Brain research. 2004;1004(1-2):98-107. Epub 2004/03/23. doi: 10.1016/j.brainres.2003.12.043. PubMed PMID: 15033424.

220. Hosie AM, Buckingham SD, Hamon A, Sattelle DB. Replacement of asparagine with arginine at the extracellular end of the second transmembrane (M2) region of insect GABA receptors increases sensitivity to penicillin G. Invertebrate neuroscience : IN. 2006;6(2):75-9. Epub 2006/06/08. doi: 10.1007/s10158-006-0020-4. PubMed PMID: 16758255.

221. Hosie AM, Wilkins ME, da Silva HM, Smart TG. Endogenous neurosteroids regulate GABAA receptors through two discrete transmembrane sites. Nature. 2006;444(7118):486-9. Epub 2006/11/17. doi: 10.1038/nature05324. PubMed PMID: 17108970.

222. Hosie AM, Wilkins ME, Smart TG. Neurosteroid binding sites on GABA(A) receptors. Pharmacology & therapeutics. 2007;116(1):7-19. Epub 2007/06/15. doi: 10.1016/j.pharmthera.2007.03.011. PubMed PMID: 17560657.

223. Laverty D, Thomas P, Field M, Andersen OJ, Gold MG, Biggin PC, et al. Crystal structures of a GABAA-receptor chimera reveal new endogenous neurosteroid-binding sites. Nature structural & molecular biology. 2017;24(11):977-85. Epub 2017/10/03. doi: 10.1038/nsmb.3477. PubMed PMID: 28967882.

224. Gielen M, Thomas P, Smart TG. The desensitization gate of inhibitory Cys-loop receptors. Nature communications. 2015;6:6829. Epub 2015/04/22. doi: 10.1038/ncomms7829. PubMed PMID: 25891813; PubMed Central PMCID: PMCPMC4410641.

225. Rankin SE, Addona GH, Kloczewiak MA, Bugge B, Miller KW. The cholesterol dependence of activation and fast desensitization of the nicotinic acetylcholine receptor. Biophysical journal. 1997;73(5):2446-55. Epub 1997/11/25. doi: 10.1016/s0006-3495(97)78273-0. PubMed PMID: 9370438; PubMed Central PMCID: PMCPMC1181146.

226. Criado M, Eibl H, Barrantes FJ. Effects of lipids on acetylcholine receptor. Essential need of cholesterol for maintenance of agonist-induced state transitions in lipid vesicles. Biochemistry. 1982;21(15):3622-9. Epub 1982/07/20. PubMed PMID: 7115688.

227. Paradiso K, Sabey K, Evers AS, Zorumski CF, Covey DF, Steinbach JH. Steroid inhibition of rat neuronal nicotinic alpha4beta2 receptors expressed in HEK 293 cells. Molecular pharmacology. 2000;58(2):341-51. Epub 2000/07/25. PubMed PMID: 10908302.

228. Ke L, Lukas RJ. Effects of steroid exposure on ligand binding and functional activities of diverse nicotinic acetylcholine receptor subtypes. Journal of neurochemistry. 1996;67(3):1100-12. Epub 1996/09/01. PubMed PMID: 8752117.

229. Barrantes FJ, Antollini SS, Bouzat CB, Garbus I, Massol RH. Nongenomic effects of steroids on the nicotinic acetylcholine receptor. Kidney international. 2000;57(4):1382-9. Epub 2000/04/12. doi: 10.1046/j.1523-1755.2000.00979.x. PubMed PMID: 10760071.

230. Palma A, Li L, Chen XJ, Pappone P, McNamee M. Effects of pH on acetylcholine receptor function. The Journal of membrane biology. 1991;120(1):67-73. Epub 1991/02/01. PubMed PMID: 2020020.

231. li L, McNamee M. Modulation of Nicotinic Acetylcholine Receptor Channel by pH: A Difference in pH Sensitivity of Torpedo and Mouse Receptors Expressed in Xenopus Oocytes. Cellular and Molecular Biology. 1991;12(2):83-93.

232. Campagna JA, Miller KW, Forman SA. Mechanisms of actions of inhaled anesthetics. The New England journal of medicine. 2003;348(21):2110-24. Epub 2003/05/23. doi: 10.1056/NEJMra021261. PubMed PMID: 12761368.

233. Mason GA, Walker CH, Prange AJ, Jr. L-triiodothyronine: is this peripheral hormone a central neurotransmitter? Neuropsychopharmacology : official publication of the American College of Neuropsychopharmacology. 1993;8(3):253-8. Epub 1993/05/01. doi: 10.1038/npp.1993.28. PubMed PMID: 8099484.

234. Sarkar PK, Ray AK. Specific binding of L-triiodothyronine modulates Na(+)-K(+)-ATPase activity in adult rat cerebrocortical synaptosomes. Neuroreport. 1998;9(6):1149-52. Epub 1998/05/28. PubMed PMID: 9601684.

235. Mienville JM, Vicini S. Pregnenolone sulfate antagonizes GABAA receptor-mediated currents via a reduction of channel opening frequency. Brain research. 1989;489(1):190-4. Epub 1989/06/05. PubMed PMID: 2472854.

236. Sattelle DB, McClay AS, Dowson RJ, Callec JJ. The pharmacology of an insect ganglion: actions of carbamylcholine and acetylcholine. The Journal of experimental biology. 1976;64(1):13-23. Epub 1976/02/01. PubMed PMID: 178820.

237. Forman SA, Firestone LL, Miller KW. Is agonist self-inhibition at the nicotinic acetylcholine receptor a nonspecific action? Biochemistry. 1987;26(10):2807-14. Epub 1987/05/19. PubMed PMID: 3038165.

238. Epstein M, Racker E. Reconstitution of carbamylcholine-dependent sodium ion flux and desensitization of the acetylcholine receptor from Torpedo californica. The Journal of biological chemistry. 1978;253(19):6660-2. Epub 1978/10/10. PubMed PMID: 690117.

239. O'Shaughnessy KM. Chapter 22 - Cholinergic and antimuscarinic (anticholinergic) mechanisms and drugs. In: Bennett PN, Brown MJ, Sharma P, editors. Clinical Pharmacology (Eleventh Edition). Oxford: Churchill Livingstone; 2012. p. 372-81.

240. Shiroma LO, Costa VP. 56 - Parasympathomimetics. In: Shaarawy TM, Sherwood MB, Hitchings RA, Crowston JG, editors. Glaucoma (Second Edition): W.B. Saunders; 2015. p. 577-82.

241. Akk G, Auerbach A. Activation of muscle nicotinic acetylcholine receptor channels by nicotinic and muscarinic agonists. British journal of pharmacology. 1999;128(7):1467-76. Epub 1999/12/22. doi: 10.1038/sj.bjp.0702941. PubMed PMID: 10602325; PubMed Central PMCID: PMCPMC1571784.

242. Marsal J, Tigyi G, Miledi R. Incorporation of acetylcholine receptors and Cl- channels in Xenopus oocytes injected with Torpedo electroplaque membranes. Proceedings of the National Academy of Sciences of the United States of America. 1995;92(11):5224-8. Epub 1995/05/23. PubMed PMID: 7761478; PubMed Central PMCID: PMCPMC41881.

243. Morales A, Aleu J, Ivorra I, Ferragut JA, Gonzalez-Ros JM, Miledi R. Incorporation of reconstituted acetylcholine receptors from Torpedo into the Xenopus oocyte membrane. Proceedings of the National Academy of Sciences of the United States of America. 1995;92(18):8468-72. Epub 1995/08/29. PubMed PMID: 7667313; PubMed Central PMCID: PMCPMC41178.

244. Ivorra I, Fernandez A, Gal B, Aleu J, Gonzalez-Ros JM, Ferragut JA, et al. Protein orientation affects the efficiency of functional protein transplantation into the xenopus oocyte membrane. The Journal of membrane biology. 2002;185(2):117-27. Epub 2002/03/14. doi: 10.1007/s00232-001-0118-x. PubMed PMID: 11891570.

245. Karlin A. Structure of nicotinic acetylcholine receptors. Current opinion in neurobiology. 1993;3(3):299-309. Epub 1993/06/01. PubMed PMID: 8369624.

246. Sine SM, Kreienkamp HJ, Bren N, Maeda R, Taylor P. Molecular dissection of subunit interfaces in the acetylcholine receptor: identification of determinants of alpha-conotoxin M1 selectivity. Neuron. 1995;15(1):205-11. Epub 1995/07/01. PubMed PMID: 7619523.

247. Xie Y, Cohen JB. Contributions of Torpedo nicotinic acetylcholine receptor gamma Trp-55 and delta Trp-57 to agonist and competitive antagonist function. The Journal of biological chemistry. 2001;276(4):2417-26. Epub 2000/11/01. doi: 10.1074/jbc.M009085200. PubMed PMID: 11056174.

248. Corringer PJ, Le Novere N, Changeux JP. Nicotinic receptors at the amino acid level. Annual review of pharmacology and toxicology. 2000;40:431-58. Epub 2000/06/03. doi: 10.1146/annurev.pharmtox.40.1.431. PubMed PMID: 10836143.

249. Unwin N. Refined structure of the nicotinic acetylcholine receptor at 4A resolution. Journal of molecular biology. 2005;346(4):967-89. Epub 2005/02/11. doi: 10.1016/j.jmb.2004.12.031. PubMed PMID: 15701510.

250. Celie PH, van Rossum-Fikkert SE, van Dijk WJ, Brejc K, Smit AB, Sixma TK. Nicotine and carbamylcholine binding to nicotinic acetylcholine receptors as studied in AChBP crystal structures. Neuron. 2004;41(6):907-14. Epub 2004/03/30. PubMed PMID: 15046723.

251. Mulle C, Changeux JP. A novel type of nicotinic receptor in the rat central nervous system characterized by patch-clamp techniques. The Journal of neuroscience : the official journal of the Society for Neuroscience. 1990;10(1):169-75. Epub 1990/01/01. PubMed PMID: 2299390.

252. Connolly J, Boulter J, Heinemann SF. Alpha 4-2 beta 2 and other nicotinic acetylcholine receptor subtypes as targets of psychoactive and addictive drugs. British journal of pharmacology. 1992;105(3):657-66. Epub 1992/03/01. PubMed PMID: 1378342; PubMed Central PMCID: PMCPMC1908465.

253. Chavez-Noriega LE, Crona JH, Washburn MS, Urrutia A, Elliott KJ, Johnson EC. Pharmacological characterization of recombinant human neuronal nicotinic acetylcholine receptors h alpha 2 beta 2, h alpha 2 beta 4, h alpha 3 beta 2, h alpha 3 beta 4, h alpha 4 beta 2, h alpha 4 beta 4 and h alpha 7 expressed in Xenopus oocytes. The Journal of pharmacology and experimental therapeutics. 1997;280(1):346-56. Epub 1997/01/01. PubMed PMID: 8996215.

254. Papke RL, Dwoskin LP, Crooks PA. The pharmacological activity of nicotine and nornicotine on nAChRs subtypes: relevance to nicotine dependence and drug discovery. Journal of neurochemistry. 2007;101(1):160-7. Epub 2007/01/24. doi: 10.1111/j.1471-4159.2006.04355.x. PubMed PMID: 17241116.

255. Jadey S, Purohit P, Auerbach A. Action of nicotine and analogs on acetylcholine receptors having mutations of transmitter-binding site residue alphaG153. The Journal of general physiology. 2013;141(1):95-104. Epub 2013/01/02. doi: 10.1085/jgp.201210896. PubMed PMID: 23277476; PubMed Central PMCID: PMCPMC3536520.

256. Forman SA, Righi DL, Miller KW. Ethanol increases agonist affinity for nicotinic receptors from Torpedo. Biochimica et biophysica acta. 1989;987(1):95-103. Epub 1989/12/11. PubMed PMID: 2597688.

257. Tonner PH, Wood SC, Miller KW. Can nicotine self-inhibition account for its low efficacy at the nicotinic acetylcholine receptor from Torpedo? Molecular pharmacology. 1992;42(5):890-7. Epub 1992/11/01. PubMed PMID: 1279379.

258. Nicotine. In: O'Neil M, editor. The Merck Index - An Encyclopedia of Chemicals, Drugs, and Biologicals. Whitehouse Station, NJ: Merck and Co., Inc.; 2006. p. 1128.

259. Gonzalez-Ros JM, Llanillo M, Paraschos A, Martinez-Carrion M. Lipid environment of acetylcholine receptor from Torpedo californica. Biochemistry. 1982;21(14):3467-74. Epub 1982/07/06. PubMed PMID: 7115681.

260. Popot JL, Demel RA, Sobel A, Van Deenen LL, Changeux JP. Interaction of the acetylcholine (nicotinic) receptor protein from Torpedo marmorata electric organ with monolayers of pure lipids. European journal of biochemistry. 1978;85(1):27-42. Epub 1978/04/01. PubMed PMID: 639821.

261. Rotstein NP, Arias HR, Barrantes FJ, Aveldano MI. Composition of lipids in elasmobranch electric organ and acetylcholine receptor membranes. Journal of neurochemistry. 1987;49(5):1333-40. Epub 1987/11/01. PubMed PMID: 2822851.

262. Dalziel AW, Rollins ES, McNamee MG. The effect of cholesterol on agonist-induced flux in reconstituted acetylcholine receptor vesicles. FEBS letters. 1980;122(2):193-6. Epub 1980/12/29. PubMed PMID: 7202709.

263. Baenziger JE, Morris ML, Darsaut TE, Ryan SE. Effect of membrane lipid composition on the conformational equilibria of the nicotinic acetylcholine receptor. The Journal of biological chemistry. 2000;275(2):777-84. Epub 2000/01/08. PubMed PMID: 10625607.

264. Ryan SE, Demers CN, Chew JP, Baenziger JE. Structural effects of neutral and anionic lipids on the nicotinic acetylcholine receptor. An infrared difference spectroscopy study. The Journal of biological chemistry. 1996;271(40):24590-7. Epub 1996/10/04. PubMed PMID: 8798723.

265. Baenziger JE, Domville JA, Therien JPD. The Role of Cholesterol in the Activation of Nicotinic Acetylcholine Receptors. Current topics in membranes. 2017;80:95-137. Epub 2017/09/03. doi: 10.1016/bs.ctm.2017.05.002. PubMed PMID: 28863823.

266. Risselada HJ, Marrink SJ. The molecular face of lipid rafts in model membranes. Proceedings of the National Academy of Sciences of the United States of America. 2008;105(45):17367-72. Epub 2008/11/07. doi: 10.1073/pnas.0807527105. PubMed PMID: 18987307; PubMed Central PMCID: PMCPMC2579886.

267. Shen XM, Deymeer F, Sine SM, Engel AG. Slow-channel mutation in acetylcholine receptor alphaM4 domain and its efficient knockdown. Annals of neurology. 2006;60(1):128-36. Epub 2006/05/11. doi: 10.1002/ana.20861. PubMed PMID: 16685696.

268. Baez-Pagan CA, Martinez-Ortiz Y, Otero-Cruz JD, Salgado-Villanueva IK, Velazquez G, Ortiz-Acevedo A, et al. Potential role of caveolin-1-positive domains in the regulation of the acetylcholine receptor's activatable pool: implications in the pathogenesis of a novel congenital myasthenic syndrome. Channels (Austin, Tex). 2008;2(3):180-90. Epub 2008/10/07. PubMed PMID: 18836288; PubMed Central PMCID: PMCPMC4495657.

269. Oyola-Cintron J, Caballero-Rivera D, Ballester L, Baez-Pagan CA, Martinez HL, Velez-Arroyo KP, et al. Lateral diffusion, function, and expression of the slow channel congenital myasthenia syndrome alphaC418W nicotinic receptor mutation with changes in lipid raft components. The Journal of biological chemistry. 2015;290(44):26790-800. Epub 2015/09/12. doi: 10.1074/jbc.M115.678573. PubMed PMID: 26354438; PubMed Central PMCID: PMCPMC4646332.

270. Padilla-Morales LF, Colon-Saez JO, Gonzalez-Nieves JE, Quesada-Gonzalez O, Lasalde-Dominicci JA. Assessment of the functionality and stability of detergent purified nAChR from Torpedo using lipidic matrixes and macroscopic electrophysiology. Biochimica et biophysica acta. 2016;1858(1):47-56. Epub 2015/10/11. doi: 10.1016/j.bbamem.2015.10.002. PubMed PMID: 26454038; PubMed Central PMCID: PMCPMC4663142.

271. Quesada O, Gonzalez-Freire C, Ferrer MC, Colon-Saez JO, Fernandez-Garcia E, Mercado J, et al. Uncovering the lipidic basis for the preparation of functional nicotinic acetylcholine receptor detergent complexes for structural studies. Scientific reports. 2016;6:32766. Epub 2016/09/20. doi: 10.1038/srep32766. PubMed PMID: 27641515; PubMed Central PMCID: PMCPMC5027579.

272. Marsh D, Barrantes FJ. Immobilized lipid in acetylcholine receptor-rich membranes from Torpedo marmorata. Proceedings of the National Academy of Sciences of the United States of America. 1978;75(9):4329-33. Epub 1978/09/01. PubMed PMID: 212745; PubMed Central PMCID: PMCPMC336108.

273. Barrantes FJ. Structural basis for lipid modulation of nicotinic acetylcholine receptor function. Brain research Brain research reviews. 2004;47(1-3):71-95. Epub 2004/12/02. doi: 10.1016/j.brainresrev.2004.06.008. PubMed PMID: 15572164.

274. Lee AG. How lipids affect the activities of integral membrane proteins. Biochimica et biophysica acta. 2004;1666(1-2):62-87. Epub 2004/11/03. doi: 10.1016/j.bbamem.2004.05.012. PubMed PMID: 15519309.

275. Crump A, Omura S. Ivermectin, 'wonder drug' from Japan: the human use perspective. Proceedings of the Japan Academy Series B, Physical and biological sciences. 2011;87(2):13-28. Epub 2011/02/16. PubMed PMID: 21321478; PubMed Central PMCID: PMCPMC3043740.

276. Cully DF, Vassilatis DK, Liu KK, Paress PS, Van der Ploeg LH, Schaeffer JM, et al. Cloning of an avermectin-sensitive glutamate-gated chloride channel from Caenorhabditis elegans. Nature. 1994;371(6499):707-11. Epub 1994/10/20. doi: 10.1038/371707a0. PubMed PMID: 7935817.

277. Ghosh R, Andersen EC, Shapiro JA, Gerke JP, Kruglyak L. Natural variation in a chloride channel subunit confers avermectin resistance in C. elegans. Science (New York, NY). 2012;335(6068):574-8. Epub 2012/02/04. doi: 10.1126/science.1214318. PubMed PMID: 22301316; PubMed Central PMCID: PMCPMC3273849.

278. Kane NS, Hirschberg B, Qian S, Hunt D, Thomas B, Brochu R, et al. Drug-resistant Drosophila indicate glutamate-gated chloride channels are targets for the antiparasitics nodulisporic acid and ivermectin. Proceedings of the National Academy of Sciences of the United States of America. 2000;97(25):13949-54. Epub 2000/11/30. doi: 10.1073/pnas.240464697. PubMed PMID: 11095718; PubMed Central PMCID: PMCPMC17681.

279. McCavera S, Rogers AT, Yates DM, Woods DJ, Wolstenholme AJ. An ivermectin-sensitive glutamate-gated chloride channel from the parasitic nematode Haemonchus contortus. Molecular pharmacology. 2009;75(6):1347-55. Epub 2009/04/02. doi: 10.1124/mol.108.053363. PubMed PMID: 19336526; PubMed Central PMCID: PMCPMC2684884.

280. Martin RJ, Pennington AJ. A patch-clamp study of effects of dihydroavermectin on Ascaris muscle. British journal of pharmacology. 1989;98(3):747-56. Epub 1989/11/01. PubMed PMID: 2480169; PubMed Central PMCID: PMCPMC1854754.

281. Hibbs RE, Gouaux E. Principles of activation and permeation in an anion-selective Cys-loop receptor. Nature. 2011;474(7349):54-60. Epub 2011/05/17. doi: 10.1038/nature10139. PubMed PMID: 21572436; PubMed Central PMCID: PMCPMC3160419.

282. Lynagh T, Lynch JW. A glycine residue essential for high ivermectin sensitivity in Cys-loop ion channel receptors. International journal for parasitology. 2010;40(13):1477-81. Epub 2010/08/18. doi: 10.1016/j.ijpara.2010.07.010. PubMed PMID: 20713056.

283. Kwon DH, Yoon KS, Clark JM, Lee SH. A point mutation in a glutamate-gated chloride channel confers abamectin resistance in the two-spotted spider mite, Tetranychus urticae Koch. Insect molecular biology. 2010;19(4):583-91. Epub 2010/06/05. doi: 10.1111/j.1365-2583.2010.01017.x. PubMed PMID: 20522121.

284. Lynagh T, Lynch JW. Ivermectin binding sites in human and invertebrate Cys-loop receptors. Trends in pharmacological sciences. 2012;33(8):432-41. Epub 2012/06/09. doi: 10.1016/j.tips.2012.05.002. PubMed PMID: 22677714.

285. Krasowski MD, Harrison NL. General anaesthetic actions on ligand-gated ion channels. Cellular and molecular life sciences : CMLS. 1999;55(10):1278-303. Epub 1999/09/16. doi: 10.1007/s000180050371. PubMed PMID: 10487207; PubMed Central PMCID: PMCPMC2854026.

286. Brannigan G, LeBard DN, Henin J, Eckenhoff RG, Klein ML. Multiple binding sites for the general anesthetic isoflurane identified in the nicotinic acetylcholine receptor transmembrane domain. Proceedings of the National Academy of Sciences of the United States of America. 2010;107(32):14122-7. Epub 2010/07/28. doi: 10.1073/pnas.1008534107. PubMed PMID: 20660787; PubMed Central PMCID: PMCPMC2922517.

287. Weng Y, Yang L, Corringer PJ, Sonner JM. Anesthetic sensitivity of the Gloeobacter violaceus proton-gated ion channel. Anesthesia and analgesia. 2010;110(1):59-63. Epub 2009/11/26. doi: 10.1213/ANE.0b013e3181c4bc69. PubMed PMID: 19933531; PubMed Central PMCID: PMCPMC2897236.

288. Firestone LL, Sauter JF, Braswell LM, Miller KW. Actions of general anesthetics on acetylcholine receptor-rich membranes from Torpedo californica. Anesthesiology. 1986;64(6):694-702. Epub 1986/06/01. PubMed PMID: 3717633.

289. Dilger JP, Brett RS, Mody HI. The effects of isoflurane on acetylcholine receptor channels.: 2. Currents elicited by rapid perfusion of acetylcholine. Molecular pharmacology. 1993;44(5):1056-63. Epub 1993/11/01. PubMed PMID: 7504168.